

AD-A138 531

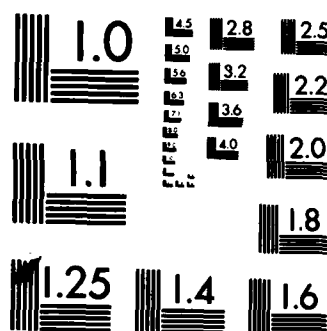
ACTA AERONAUTICA ET ASTRONAUTICA SINICA (SELECTED
ARTICLES)(U) FOREIGN TECHNOLOGY DIV WRIGHT-PATTERSON
AFB OH H Y LI ET AL. 30 JAN 84 FTD-ID(R5)T-1752-83
F/G 1/3

1/2

UNCLASSIFIED

NL

[illegible]



MICROCOPY RESOLUTION TEST CHART
NATIONAL BUREAU OF STANDARDS-1963-A

AD A138531

FTD-ID(RS)T-1752-83

FOREIGN TECHNOLOGY DIVISION



ACTA AERONAUTICA ET ASTRONAUTICA SINICA

(Selected Articles)



DTIC

MAR 2 1984

A

Approved for public release;
distribution unlimited.

DTIC FILE COPY

84 03 01 060

EDITED TRANSLATION

FTD-ID(RS)T-1752-83

30 January 1984

MICROFICHE NR: FTD-84-C-000110

ACTA AERONAUTICA ET ASTRONAUTICA SINICA (Selected Articles)

English pages: 140

Source: Hang Kong Xuebao, Vol. 4, Nr. 2, June 1983,
pp. 1-38; 73-111

Country of origin: China

Translated by: SCITRAN

F33657-81-D-0263

Requester: FTD/TQTA

Approved for public release; distribution unlimited.



THIS TRANSLATION IS A RENDITION OF THE ORIGINAL FOREIGN TEXT WITHOUT ANY ANALYTICAL OR EDITORIAL COMMENT. STATEMENTS OR THEORIES ADVOCATED OR IMPLIED ARE THOSE OF THE SOURCE AND DO NOT NECESSARILY REFLECT THE POSITION OR OPINION OF THE FOREIGN TECHNOLOGY DIVISION.

PREPARED BY:

TRANSLATION DIVISION
FOREIGN TECHNOLOGY DIVISION
WP-AFB, OHIO.

Table of Contents

Graphics Disclaimer	ii
Finite Difference Computation of Wave Drag and Pressure on Slender Bodies of Revolution at Transonic Speeds with Zero-Lift*, by Li Hsiu-ying and Lo Shih-chün	1
Characteristics of Metal Fatigue Propagation in the Initial Stage and Its Influencing Factors, by Yan Minggao	19
Finite Element Models Based on a Generalized Hamilton's Principle for Pfluger's Rod and Its Related Plate*, by Chang Kung-hsing and Li Sung-nien	57
Buse in Axisymmetric Supersonic Inlet and Its Control, by Ho Chung-wei and Chang Shih-ying	72
A Prediction Method for Characteristics of Cooled Transonic Turbines with Low Aspect Ratio and High Load*, by Chuang Yü-nan, Chao Yü-ch'i, Shih Ching, and Han Chien-yüen	88
Effect of Resin Matrix Toughness on Mechanical Properties of Composite Materials, by Ma Ruiran, Zhou Xizhen, Wang Yan, and Zhang Wu	106
Monitoring Cure Process of Composites with Dynamic Dielectric Analysis Technique*, by Tu Shicun, Li Xingzhou, Shen Rongying, and Man Shupeng	125
Brief News of Technical Meetings of the Society	135

GRAPHICS DISCLAIMER

All figures, graphics, tables, equations, etc. merged into this translation were extracted from the best quality copy available.

Finite Difference Computation of Wave Drag and Pressure on
Slender Bodies of Revolution at Transonic Speeds
with Zero-Lift*

Li Hsiu-ying and Lo Shih-chün
(Northwestern Polytechnical University)

ABSTRACT

A transonic axisymmetrical potential equation with large disturbance in the free stream direction and small disturbance in the transverse direction is solved by using the Murman-Cole schemes of finite differences. The boundary condition on the body is transferred to body axis. The boundary condition at far field is approximated by that at infinity.

Finite difference equations for the potential are solved by line-overrelaxation along the radius with Seidel iteration. In order to calculate the pressure on the body surface, the potential is interpolated by the slender-body theory. The pressure coefficient is calculated by the exact Bernoulli's equation. The zero-lift wave-drag coefficients are obtained by integrating the pressure coefficients on the body surface.

The computational results for seven different configurations agree well with the known wind tunnel test data as shown in Figure 2 to Figure 6. The experiences obtained from investigation of mesh spacings, initial-fields, iterative methods, relaxation factors, etc., in relation to the convergence and rate of convergence may be interesting to engineers.

A linearized analysis of the stability and the convergence in line overrelaxation of difference equations for steady axisymmetric small

* Received July, 1982.

This paper was accepted for reading at the 8th meeting of the International Conference of Numerical Methods in Fluid Mechanics (June 28 - July 2, 1982, Aachen, West Germany).

perturbation potential flow is carried out and the conclusions are shown in Table 1. The numerical computations do agree with the theoretical conclusions.

It must be pointed out that as M_∞ is very close to unity or the mesh spacing is shortened, the iterative computation does not converge to the usual degree of accuracy. This fact might be explained by a decrease in the artificial viscosity in the potential difference equation at locally supersonic points.

The mesh is taken to be 62×16 , and the initial field for the iteration, 0. The numbers of iterations necessary before convergence is achieved are approximately 150, 40 and 300, corresponding to $M_\infty < 1$, $M_\infty > 1$ and $M_\infty \sim 1$, respectively. The relaxation factors are taken to be $0.9 \leq \omega_s \leq 1.7$, $0.9 \leq \omega_s \leq 1.0$; for $M_\infty < 1$ and $0.8 \leq \omega_s \leq 0.9$, $0.8 \leq \omega_s \leq 0.9$, for $M_\infty > 1$. Here ω_s , ω_s are the relaxation factors of locally subsonic and locally supersonic points, respectively.

I. INTRODUCTION

According to the area law for transonic speeds, the zero-lift wave drag of an aircraft flying at transonic speeds is equal to that of its equivalent body of revolution under given conditions. Therefore, it is of practical value to aircraft design and analysis to present a convenient method and procedure for calculating the wave drag of bodies of revolution at transonic speeds with zero-lift.

The mixed finite difference scheme [1] is an effective method for solving transonic constant steady potential flow problems with computers. In References [2], [3] and [4], the canonical small perturbation velocity potential equation and boundary conditions have been used to satisfactorily compute the pressure distribution about

a moving parabolic body of revolution. However, there is as yet no published material on the computation of wave drag and pressure distribution about a body of revolution of any given shape. Keeping in mind the requirement of practical applicability, we have used the mixed finite difference scheme to compute and study the transonic axisymmetric potential flow about a body of revolution of any shape.

The canonical small perturbation velocity potential equation has a singularity at the nodal point on the bow of an object with a blunt bow, and is not applicable at other nodal points either. Hence, it cannot be applied to an object that may take on any shape. In Reference [5], a potential equation with large perturbation in the free stream direction and small perturbation in the transverse direction and the corresponding boundary conditions have been adopted. This avoids the singularity of the canonical small perturbation equation at the nodal point on a blunt bow. In theory, this can increase the accuracy of the computation of the flow in the vicinity of the nodal point. Furthermore, it does not require any additional computing time. Based on the above considerations, we also adopt this equation and its boundary conditions in this work.

The finite difference equations are solved by line-overrelaxation along the radius with Seidel iteration. Stability and convergence are important criteria of a successful iterative computation. To provide a guideline for the iterative computation, we have performed an analysis of stability and convergence. Owing to the complexity of the nonlinear problem, this analysis has been carried out under the condition of local linearization.

II. FUNDAMENTAL EQUATIONS AND FORMULAS

Take the Ox -axis to be along the axial direction of the object, and the Or -axis to be along the radial direction of the object. The origin of the coordinate system is taken to be at the apex of the bow (Figure 1). Assume that the large perturbation is along the x -direction, while the small perturbation is along the r -direction. The perturbing velocity potential equation is given by

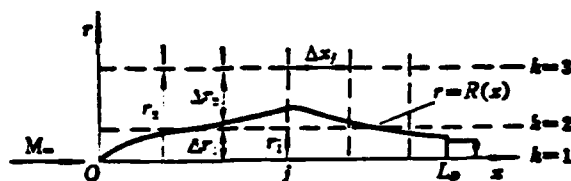


Figure 1. Illustration of model and mesh spacing

$$(1 - M^2) \varphi_{xx} + (r \varphi_r)_r / r = 0 \quad (1)$$

It is necessary to express the above equation in terms of rectangular coordinates on the x-axis in front of the object:

$$(1 - M^2) \varphi_{xx} + \varphi_{rr} + \varphi_{rr} = 0 \quad (1')$$

In the above equation,

$$1 - M^2 = \frac{1 - M_\infty^2 - \frac{\gamma + 1}{q_\infty} M_\infty^2 \varphi_r - \frac{\gamma + 1}{2q_\infty^2} M_\infty^2 \varphi_r^2}{1 - \frac{\gamma - 1}{q_\infty} M_\infty^2 \varphi_r - \frac{\gamma - 1}{2q_\infty^2} M_\infty^2 \varphi_r^2} \quad (2)$$

ϕ ---- is the perturbing velocity potential;

M ---- is the local Mach number

q_∞, M_∞ ---- are respectively the velocity and Mach number of the unperturbed flow ;

γ ---- is the adiabatic index of the gas.

Let the equation for the surface of the body of revolution be given by $r = R(x)$, and assume the object to be a slender body. The boundary condition on the surface of the object (including the tail branch rod) is transferred to the x-axis, i.e.,

$$(r \varphi_r(x, r))_{r=R} \approx (r \varphi_r(x, r))_{r=R} = RR' (q_\infty + \varphi_r(x, R)) \quad (3)$$

The apex of the bow of an object with a sharp bow satisfies the condition specified by Equation (3). For an object with a blunt head, the apex of the bow is treated as a nodal point, i.e.,

$$\varphi_r = -\infty, \varphi_r = 0 \quad (4)$$

The boundary condition at far field is approximated by that at infinity:

$$\varphi = 0 \quad (5)$$

Along the x-axis in front of the object, the flow is symmetrical with respect to the x-axis,

$$\varphi_x = \varphi_r = 0 \quad (6)$$

Let $\Delta r_2 = 2\Delta r_1$. Inserting the boundary condition on the surface of the object into the velocity potential equation, one obtains the expression (Refer to Figure 1):

$$(r\varphi_r)_{r=r_2} = \frac{1}{\Delta r_2} (\varphi_{j+2} - \varphi_{j-2} - RR' [q_\infty + \varphi_s(x, r_2)]) + O(\Delta r^2)$$

Here, j and k are the index numbers of the mesh along the x-direction and r-direction, respectively.

Inserting the boundary condition given by Equation (4) for the apex of the bow into the velocity potential equation, one obtains the expression

$$(\Delta r_2^2 + 8\Delta x_{j+1,1}^2)\varphi_{j+1,1} - 8\Delta x_{j+1,1}^2\varphi_{j+2,1} = \Delta r_2^2(\varphi_{j+1,1} - q_\infty\Delta x_{j+1,1})$$

Here, j1 is the j-index of the apex of the bow.

Inserting the boundary condition on the x-axis in front of the object into the velocity potential equation, one obtains the expression

$$(\varphi_{xx})_{r=0} = (\varphi_{xx})_{r=0} = \frac{8}{\Delta r_2^2} (\varphi_{j+2} - \varphi_{j+1}) + O(\Delta r)$$

Use the mixed finite difference scheme, and substitute all the derivatives in Equation (1) and the equations obtained by inserting the boundary conditions in Equation (1) with the corresponding finite difference expressions. One then obtains a set of finite difference equations. To linearize this set of equations, regard the coefficients of all the terms as known quantities, and use an iterative method of computation. The finite difference equations are solved by line-overrelaxation along the radius with Seidel iteration. The overrelaxation operation is defined by

$$\varphi_{j,k}^{(n)} = \varphi_{j,k}^{(n-1)} + \omega (\bar{\varphi}_{j,k}^{(n)} - \varphi_{j,k}^{(n-1)}) \quad (7)$$

in which $\bar{\varphi}_{j,k}^{(n)}$ is the result of the nth iteration without overrelaxation treatment, and ω is the relaxation factor.

The pressure coefficients on the surface of the object are given by the exact Bernoulli's equation:

$$C_p = \frac{2}{\gamma M_\infty^2} \left\{ \left[1 - (\gamma - 1) M_\infty^2 \left(\frac{\varphi_x}{q_\infty} + \frac{\varphi_x^2}{2q_\infty^2} + \frac{R'^2}{2} \left(1 + \frac{2\varphi_x}{q_\infty} + \frac{\varphi_x^2}{q_\infty^2} \right) \right) \right]^{\frac{\gamma}{\gamma-1}} - 1 \right\} \quad (8)$$

where ϕ_x is derived from the slender body theory^[2];

$$\varphi_x \approx (\varphi_x)_{i,2} + (R'^2 + RR'') q_\infty \ln(R/r_1)$$

The pressure coefficients at $r=\text{constant}$ in the flow field are

$$C_p = \frac{2}{\gamma M_\infty^2} \left\{ \left[1 - (\gamma - 1) M_\infty^2 \left(\frac{(\varphi_x)_{i,2}}{q_\infty} + \frac{(\varphi_x)_{i,2}^2}{2q_\infty^2} + \frac{(\varphi_r)_{i,2}^2}{2q_\infty^2} \right) \right]^{\frac{\gamma}{\gamma-1}} - 1 \right\} \quad (9)$$

The pressure drag coefficient (not including bottom drag) is given by the following expression.

$$C_{Dp} = \frac{2\pi}{s} \int_0^{L_D} C_p R R' dx \quad (10)$$

In the above equation, s is the reference area, and L_D is the object length cut off by the tail branch rod.

The zero-lift wave drag is defined as

$$C_{x0} = C_{x0} - C_{x0}|_{M_\infty = M^*}$$

where M^* is the critical Mach number.

III. COMPUTED EXAMPLE

The examples computed consist of seven slender bodies of revolution with different configurations. The surface pressure distribution and zero-lift pressure drag coefficients of a parabolic-arc body of revolution^[6] having fineness ratio of 12 are given in Figures 2(a) and 2(b), respectively. Figure 3 gives the zero-lift wave drag coefficients for a sing-body combination and those for the body alone. The body consists of a cylinder and a missile type forebody, and the wing is a delta wing. Figure 4(a) gives the zero-lift wave drag coefficients for a swept-wing and curved-body combination^[7] and those for the body alone. Figure 4(b) gives the computed pressure distribution of a body of revolution equivalent to the swept-wing and curved-body combination. The shock wave positions obtained from Figure 4(b) are given in Figure 4(c). Figures 5(a) and 6(a) give the cross-sectional area distribution in the axial direction for a certain aircraft I and aircraft II, respectively. The zero-lift wave drag coefficients corresponding to these area distributions are shown in Figures 5(b) and 6(b), respectively. Except for the results shown in Figure 4(b), all the computed results have been compared with the wind tunnel test data. There is a fairly good agreement between the computed and experimental results. In Figure 5(b), the results obtained from finite difference computations are also compared with those obtained from the linearized theory. It is obvious that the former is superior to the latter.

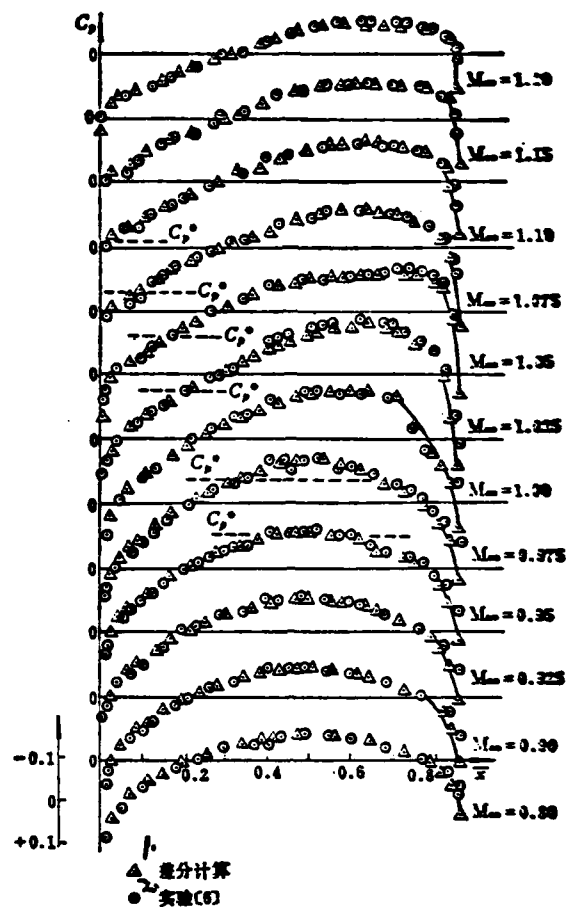


Figure 2(a) Pressure distribution on surface of a parabolic-arc body of revolution having fineness ratio of 12⁽⁶⁾
 Key: 1- Finite difference computation; 2- Experimental results

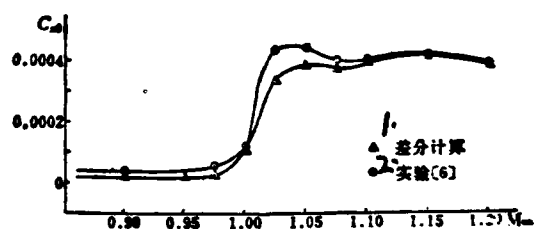


Figure 2(b) Zero-lift pressure drag coefficients of a parabolic-arc body of revolution having fineness ratio of 12⁽⁶⁾
 Key: 1- Finite difference computation; 2- Experimental results

The discrepancy between the results computed by finite difference method and those obtained experimentally is chiefly due to two factors. First, in the finite difference computation, the effect of the boundary layer has not been taken into consideration. Secondly, the experimental data are subject to errors due to their dependence on the extent the wind tunnel is choked^[8].

The values of M_∞ in the examples range from 0.8 to 1.4. There are from 11 to 13 M_∞ for each example. Computer time required on the Felix C-256 machine is around two hours while it is about a half hour on the Siemens 7760 machine.

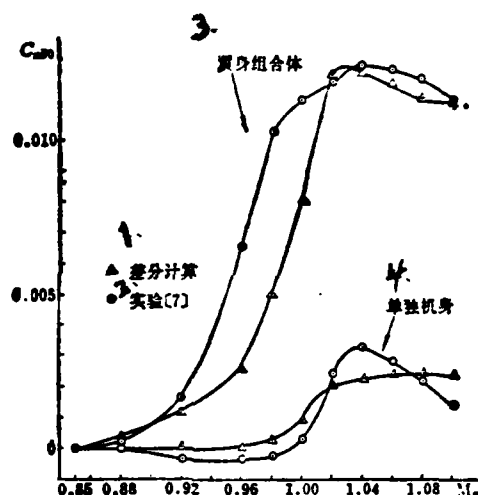


Figure 3. Zero-lift wave drag coefficients for a body of revolution equivalent to a delta-wing-body combination [7] and for the isolated body consisting of a cylinder and a missile type forebody.

Key: 1- Finite difference computation; 2- Experimental result; 3- Wing-body combination; 4- Isolated body.

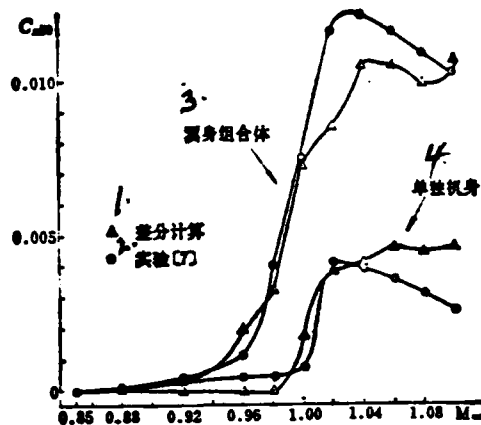


Figure 4(a). Zero-lift wave drag coefficients for a body of revolution equivalent to a swept-wing and curved-body combination [7] and for the isolated body.

Key: 1- Finite difference computation; 2- Experimental result;
3- Wing-body combination; 4- Isolated body.

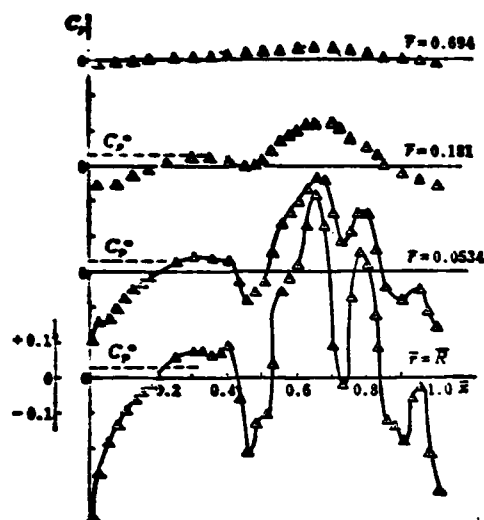


Figure 4(b). Computed pressure distribution of a body of revolution equivalent to a swept-wing and curved-body combination [7] at $M_{\infty} = 0.98$.

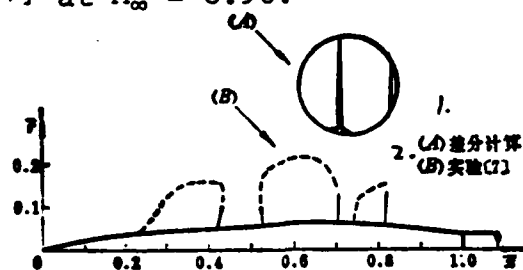


Figure 4(c). Shock-wave positions obtained from Figure 4(b).

Key: 1- Finite difference computation; 2- Experimental result



Figure 5(a). Cross-sectional area distribution of the aircraft

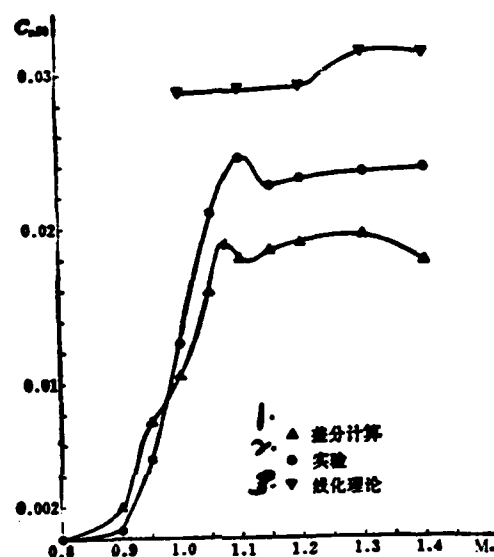


Figure 5(b). Zero-lift wave drag coefficients of the aircraft.

Key: 1- Finite difference computation; 2- Experimental result;
5- Linearized theory.

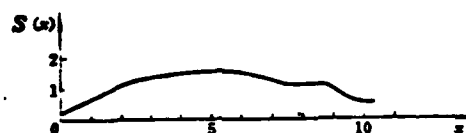


Figure 6(a). Cross-sectional area distribution of the aircraft I.

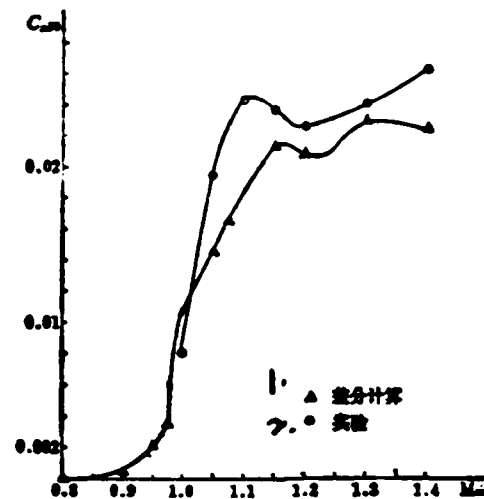


Figure 6(b) Zero-lift wave drag coefficients of the aircraft II.
Key: 1- Finite difference computation; 2- Experimental result

/8

IV. DISCUSSION OF METHODS

Comparison of computed results with experimental data shows that it is better to treat the apex of the bow and the end point of the tail as points on the inner side of the surface.

To study the effect of mesh spacing on the accuracy and convergence of the results of computation, we compared the results obtained by distributing 40, 80 and 160 mesh points, respectively, on the object along the axial line. We found that the choice of 40 mesh points along the axial line allows faster convergence, saves computer time and meets the requirement on accuracy of the job. Therefore, our choice of the mesh is as follows: The distance on the x-axis between $x=0$, and $x=L_D$ is divided into 40 equal spacings. To the front of $x=0$, 10 spacings are taken, with the first two each equal to $L_D/40$, and the remaining step lengths increasing in such a manner as to form a geometric progression with a common ratio of 2. To the back of $x=L_D$, 11 spacings are taken, with the same variation in step length as that for the points taken in front of $x=0$. Fifteen spacings are taken along the r-axis, with $\Delta r_2 = \Delta r_3 = 2\Delta r_1$ and the remaining step lengths forming a geometric progression with a common ratio of 2. Experience shows that Δr_1 can have any value lying within the range $\Delta r_1 \rightarrow 0$. We take it to be $L_D/80$. Hence, the total number of mesh points is 62×16 , and the farfield boundaries are $x=-12.8L_D$, $26.6L_D$ and $r=204.8L_D$.

We have also carried out trial computations for different far-field boundaries. The results show that the requirement on accuracy of the job is satisfactorily met by taking them at $10-20 L_D$ in front of and to the back of the object along the x-axis, and at $100 L_D$ along the r-direction. However, it may be well in the case of $M_\infty = 1$ to take the boundary points farther out along the r-direction. With this choice of the boundary points, the farfield boundary condition may be approximated by Equation (5). If the farfield boundaries are taken to be too close to the object, then there will be larger errors produced by approximating the farfield boundary condition with Equation (5).

We have compared the results obtained by using zero initial-field and those obtained by taking the initial field to be the final field computed from a neighboring M_∞ value that has been previously obtained from computation. The results show that the former converges faster. While the latter also converges, it requires many more iterations to attain the same degree of accuracy. Therefore, the initial field is taken to be zero in this work.

Both computational work and analysis of the local linearization theory (Section V) show that, under supercritical conditions, the use of the simple iterative method leads to instability in the computation. Except for the velocity determinant $1-M^2$ for which the simple iterative method has been used, we use the improved Seidel iteration throughout this work.

The results of the computations show that the optimal relaxation coefficient depends on M_∞ and the step length. For the same mesh spacing, the closer M_∞ is to 1, the smaller the value of the relaxation factor should be taken within the range given below. Otherwise, the computation may not converge. For the same M_∞ , the smaller the step length, the smaller the optimal relaxation coefficient. This is in agreement with the conclusion obtained from the stability analysis (Section V). In this paper, the relaxation coefficients for the 62×16 mesh are taken from the following ranges:

$$\begin{aligned} \text{For } M < 1, & \quad 0.9 \leq \omega \leq 1.7, \quad 0.9 \leq \omega \leq 1.0, \\ \text{for } M > 1, & \quad 0.8 \leq \omega \leq 0.9, \quad 0.8 \leq \omega \leq 0.9 \end{aligned}$$

Here, ω_b and ω_p denote, respectively, the relaxation factors for the locally subsonic points and locally supersonic points.

For $M_\infty < 1$, the convergence is usually monotonous. In general, after about 150 iterations, $\Delta\varphi \leq 10^{-4}$ ($\Delta\varphi = |\Delta\varphi_{n+1}^{(i)} / \Delta\varphi_{n+1}^{(i)}|$ denotes the maximal relative iterative error of the velocity potential field). For $M_\infty > 1$, the convergence goes through an oscillatory phase before it becomes monotonous. In general, $\Delta\varphi \leq 10^{-4}$ can be attained after 40 iterations. For $M_\infty \sim 1$, individual points may cause the velocity potential not to converge to the usual degree of accuracy. However, in general, after 200 to 300 iterations, the aerodynamic coefficients can be made to converge. Similar results are obtained when the mesh is shortened along the x-direction. This may be due to a decrease in the artificial viscosity in the finite difference equation at locally supersonic points. Said artificial viscosity is given by

$$(1 - M^2)\varphi_{xx}\Delta x$$

Both $M \rightarrow 1$ and $\Delta x \rightarrow 0$ cause the artificial viscosity to become smaller, making it difficult for the computation to converge. This problem requires further study.

V. STABILITY AND CONVERGENCE UNDER THE CONDITION OF LOCAL LINEARIZATION

When Equation (1) is solved with the iterative method, the non-linear terms in the equation have actually been locally linearized at every point.

Assume that the coefficient $1 - M^2$ of the ϕ_{xx} term in Equation (1) is a constant. Then, at the locally subsonic and locally supersonic points, Equation (1) can be transformed respectively into

$$\pm \varphi_{xx} + (r\varphi_r)_r = 0 \quad (11)$$

Let the step lengths Δx and Δr be constants. Then the finite difference equations for Equation (11) to be solved by line-over-relaxation along the radial direction become

$$\left. \begin{aligned} \frac{\varphi_{j+1,k}^{(n-1)} - 2\bar{\varphi}_{j,k}^{(n)} + \varphi_{j-1,k}^{(n)}}{\Delta x^2} \\ - \frac{\bar{\varphi}_{j,k}^{(n)} - 2\varphi_{j-1,k}^{(n)} + \varphi_{j-2,k}^{(n)}}{\Delta x^2} \end{aligned} \right\} + \frac{\bar{\varphi}_{j,k+1}^{(n)} - 2\bar{\varphi}_{j,k}^{(n)} + \bar{\varphi}_{j,k-1}^{(n)}}{\Delta r^2} + \frac{\bar{\varphi}_{j,k+1}^{(n)} - \bar{\varphi}_{j,k-1}^{(n)}}{r_k 2\Delta r} = 0 \quad (12a)$$

$$(12b)$$

Equations (12a) and (12b) are equivalent to the following differential equations, respectively:

$$\varphi_{xx} + \varphi_{rr} - \frac{\Delta t}{\Delta x} \varphi_{xr} + \frac{1}{r} \varphi_r - \frac{\Delta t}{\Delta x^2} \left(\frac{2}{\omega} - 1 \right) \varphi = 0 \quad (12a')$$

$$-\varphi_{xx} + \varphi_{rr} + \frac{1}{r} \varphi_r - \frac{\Delta t}{\Delta x^2} \left(\frac{1}{\omega} - 1 \right) \varphi = 0 \quad (12b')$$

Equations (12a') and (12b') are, respectively, hyperbolic and parabolic, and have inherent stability problems. The solutions of Equation (12a) and (12b) can be expressed in the form $\varphi(x, r, t) + \delta(x, r, t)$, where $\phi(x, r, t)$ is the exact solution and $\delta(x, r, t)$ is the error. $\delta(x, r, t)$ also satisfy Equations (12a) and (12b), and can be expressed as

$$\delta(x, r, t) = e^{i\alpha t / (\beta_1 x + \beta_2 r)} \quad (13)$$

In the above equation, $i = \sqrt{-1}$, β_1 and β_2 are any real numbers and α is a function of β_1 and β_2 . The condition of stability requires that the error not increase with time, i.e.,

$$|e^{i\alpha t}| \leq 1 \quad (14)$$

Making use of Equations (7), (12a) and (13), we obtain

$$|e^{i\theta_1 \Delta x}| = \frac{\left(\left(\frac{2}{\omega} - 1 \right) \left(\frac{1}{\Delta x^2} + \frac{2 \sin^2 \left(\frac{\beta_1 \Delta r}{2} \right)}{\Delta r^2} \right) - \frac{1 - e^{-i\theta_1 \Delta x}}{\Delta x^2} - \frac{2 \sin^2 \left(\frac{\beta_1 \Delta r}{2} \right)}{\Delta r^2} + i \frac{\left(1 - \frac{1}{\omega} \right) \sin \beta_1 \Delta r}{\Delta r r_k} \right)}{\left(\left(\frac{2}{\omega} - 1 \right) \left(\frac{1}{\Delta x^2} + \frac{2 \sin^2 \left(\frac{\beta_1 \Delta r}{2} \right)}{\Delta r^2} \right) + \frac{1 - e^{-i\theta_1 \Delta x}}{\Delta x^2} + \frac{2 \sin^2 \left(\frac{\beta_1 \Delta r}{2} \right)}{\Delta r^2} - i \frac{\sin \beta_1 \Delta r}{\omega \Delta r r_k} \right)} \quad (15)$$

The condition under which the above equation satisfies the inequality (14) is $0 < \omega \leq \omega_1 < 2$. Here, ω_1 decreases with decreasing step length.

Convergence refers to the convergence of the solutions for the artificial-time-dependent differential equations (12a') and (12b') to the solutions for Equation (11).

Let $\tau = t + \frac{1}{2} \frac{\Delta t}{\Delta x} x$. Equation (12a') can be written as

$$\varphi_{xx} + \varphi_{rr} - \frac{1}{4} \left(\frac{\Delta t}{\Delta x} \right)^2 \varphi_{\tau\tau} + \frac{1}{r} \varphi_r - \frac{\Delta t}{\Delta x^2} \left(\frac{2}{\omega} - 1 \right) \varphi = 0 \quad (16)$$

The solution for Equation (16) can be found by the method of separation of variables

$$\varphi(x, r, \tau) = G_m(x, r) + \sum_{m=1}^{\infty} (A_m e^{-\lambda_m^2 \tau} + B_m e^{-\lambda_m^2 \tau}) G_m(x, r) \quad (17)$$

Here $G_m(x, r)$ is the eigenfunction of the boundary value problem equation below.

$$G_{mm} + G_{rr} + G_r/r + \lambda_m^2 G = 0$$

λ_m^2 is the corresponding eigenvalue with $\lambda_1^2 < \lambda_2^2 < \dots < \lambda_{m-1}^2 < \lambda_m^2 < \dots$, $G_m(x, r)$ is the solution for Equation (11). A_m and B_m are constants.

$$\rho_{\infty} q_{\infty} = -\frac{2}{\Delta t} \left(\frac{2}{\omega} - 1 \right) \mp \sqrt{\frac{4}{\Delta t^2} \left(\frac{2}{\omega} - 1 \right)^2 - 4 \left(\frac{\Delta x}{\Delta t} \right)^2 \lambda_{\infty}^2}$$

Obviously, when $0 < \omega < 2$,

$$\lim_{\tau \rightarrow \infty} \varphi(x, r, \tau) = G_0(x, r)$$

All the results similarly derived are listed in Table 1. Computational study shows that these are the necessary conditions for stability and convergence.

TABLE 1. Stability and Convergence Conditions for r-line Over-relaxation Iterations

	1. 改进迭代		2. 简单迭代	
3. 条件	$M < 1$	$M > 1$	$M < 1$	$M > 1$
4. 稳定性	$0 < \omega < \omega_1$ ⑦	$0 < \omega_1 < \omega < 1$	$0 < \omega < \omega_1$ ⑦	6. 恒不稳定
5. 收敛性	$0 < \omega < 2$	$0 < \omega < 1$	$0 < \omega$	

⑦. ⑦ ω_1 随网格步长减小而减小。

Key: 1- Improved iteration; 2- Simple iteration; 3- Condition;
4- Stability; 5- Convergence; 6- Always unstable;
7- ω_1 decreases with decreasing mesh step length

VI. CONCLUSION

We have given in this paper a method for computing the zero-lift wave drag and pressure distribution on slender bodies of revolution at transonic speeds. The results of the computations agree fairly well with experimental results. In practice, it is only necessary to take 40 mesh points on the object along its body axis. When the bounda

condition for the farfield is taken to be zero, the boundaries of the farfield may be taken to be at 10-20 times the length of the object along the x-direction on either end of the object, and 100 times the object length along the r-direction. The finite difference equations are solved by line over-relaxation iterations along the r-direction. To ensure stability and convergence of the iterative computation, the relaxation coefficients for locally subsonic points are taken to be $0 < \omega < 2$. For small step lengths or when M_∞ is close to 1, the optimal value of ω is small. The relaxation coefficients for locally supersonic points are taken to be $\omega \leq 1$ and close to 1. When M_∞ approaches 1, the iterative computation does not converge to the usual degree of accuracy at individual points. In this case, the standards for convergence of the aerodynamic coefficients may be used.

The problem associated with difficulty in convergence at individual points of the velocity potential when $M_\infty \rightarrow 1$ requires further study.

REFERENCES

- (1) Murman, E. M. and Cole, J. D. Calculation of Plane Steady Transonic Flows. AIAA J. 9 (1971) 114-121.
- (2) Krupp, J. A. and Murman, E. M. Computation of Transonic Flows Past Lifting Airfoils and Slender Bodies. AIAA J. 10 (1972) 890-896.
- (3) Bailey, F. R. Numerical Calculation of Transonic Flow about Slender Bodies of Revolution. NASA TN D-6582 (1971).
- (4) Stahara, S. S. and Spreiter, J. R. Transonic Wind Tunnel Interference Assessment-Axisymmetric Flows. AIAA J. 18 (1980) 63-71.
- (5) Leo, S. I., Zheng, Y. W., Qian, H. and Wang, D. Q. Finite Difference Computation for Transonic Steady Potential Flows. Computer Methods in Applied Mechanics and Engineering 27(1981)129-138.
- (6) Taylor, R. A. and McDewitt, J. B. Pressure Distribution at Transonic Speeds for Parabolic-Arc Bodies of Revolution Having Fineness Ratios of 10, 12 and 14. NACA TN 4234 (1958).
- (7) Whitcomb, R. T. A Study of the Zero-Lift Drag-Rise Characteristics of Wing-Body Combinations Near the Speed of Sound. NACA RM L52H08 (1952).
- (8) Ury, J. W. and Wallace, J. W. Drag of a Supercritical Body of Revolution in Free Flight at Transonic Speeds and Comparison with Wind-Tunnel Data. NASA TN D-6580 (1971).

Characteristics of Metal Fatigue Propagation in the
Initial Stage and Its Influencing Factors

Beijing Aeronautical Material Institute Yan Minggao

ABSTRACT

In this paper, the mechanism and characteristics of fatigue crack propagation of metals and alloys near the threshold region were reviewed.

According to the results of microfractographic analysis of a series of specimens and structures, the predominant fracture morphology is a type of facet or river pattern in the near-threshold region. The correlation between the direction of the facet of different metals and alloys, and the crystal lattice structure could be described by the slip mode and dislocation.

In this paper, the relation between fatigue limits and threshold values of plate and notched specimens, as well as the fatigue crack propagation mechanism of a short crack, were described and commented. The crack propagation behavior of a short crack can in general be expressed as:

$$\Delta K_{II} = f(a) \Delta \sigma_{II} \sqrt{\pi a} \quad (A)$$

where $f(a)$ is a function of the crack length and specimen geometry.

In this paper, the effect of stress ratio, microstructure, and environment on the fatigue crack propagation behavior in the near-threshold range was reviewed. The concept of "oxide induced" and "roughness induced" crack closure effect was presented. It may be used to explain the effect of the aforementioned factors on the fatigue crack propagation behavior at the near-threshold range in structural materials.

I. INTRODUCTION

Since the incidents of fractured truck axles in England early in this century, the study of fatigue fracture has attracted a wide range of attention. Furthermore, a great deal of experimental research and theoretical analysis had been conducted.

Nevertheless, serious incidents still occurred from time to time; from the rupture of the ship "Freedom" in the forties to the disintegration of the airliner "Comet"; from the breaking up of a rocket shell to the collapse of the oil drilling rig on the North Sea in the eighties. This shows that the inception and propagation of fatigue cracks at places where stress is concentrated on a structural piece will be unavoidable. Therefore, the study of the initial propagation of fatigue cracks using notched and microcracked structural pieces has important theoretical and practical meaning in the prevention of future disasters.

It is generally believed that the propagation of fatigue crack can be divided into three stages. During the initial propagation period, it is propagating at an extremely low rate ($da/dN < 10^{-5}$ mm/week). The region is the discontinuous propagation zone. A type of crystallographic facet or river pattern fracture begins to emerge. When $da/dN > 10^{-5}$ mm/week, then it reaches a continuous propagation region. The fracture morphology is predominantly fatigue patterns. When $da/dN > 10^{-3}$ mm/week, it is in the "static type" propagation region. The fracture morphology is predominantly intergranular fracture and fiber tear. The entire da/dN - K curve can be approximately described as an "S" shaped curve, as shown in Figure 1.^[1,2]

In the recent twenty years, people have conducted many studies on the propagating behavior of fatigue cracks in the second stage and have obtained some profound understanding. The third stage of crack propagation, however, is not too important to the lifetime estimation of structural parts because of its rapid development. For this reason, the first stage of crack propagating behavior, which has a greater sensitivity to the structure and the environment, has attracted more and more attention. Especially with the development of fracture mechanics and application of new testing techniques, a large number of scientific papers have been published. Many mechanical models and

received in September, 1982

microscopic mechanisms were proposed. However, mutual contradictions often exist between these data and results. Even opposite conclusions were obtained. For this reason, a brief review of the studies in recent years on the microstructure of the fatigue crack in its initial stage, its mechanical behavior, and its influencing factors is needed. /14

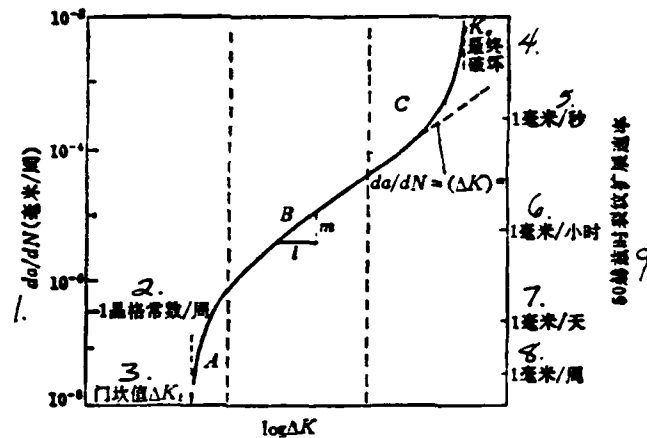


图1 $da/dN-\Delta K$ 曲线及其微观机制示意图^[1]

Fig.1 Schematic of da/dN curve and mechanisms of fracture^[1]

- | | | |
|-------------|------------------------|---------------------|
| 10. A段 | 16. B段 | 23. C段 |
| 11. 非连续型机制 | 17. 连续型机制 (条带增大) | 24. 静力型机制 (解理、晶间纤维) |
| 12. 影响大的因素 | 18. 影响小的因素 | 25. 影响大的因素 |
| 13. 1. 微观结构 | 19. 1. 微观结构 | 26. 1. 微观结构 |
| 14. 2. 平均应力 | 20. 2. 厚度 | 27. 2. 平均应力 |
| 15. 3. 环境 | 21. 影响大的因素 | 28. 3. 厚度 |
| | 22. 3. 环境、平均应力及频率的一些组合 | 29. 影响小的因素 |
| | | 30. 4. 环境 |

Figure 1. Schematic of da/dN curve and mechanisms of fracture^[1]

1. da/dN (mm/week)
2. lattice constant/week
3. threshold value ΔK_t
4. final destruction
5. 1mm/sec.
6. 1mm/hour
7. 1mm/day
8. 1mm/week
9. crack propagation rate at 50Hz
10. Segment A
11. non-continuous mechanism
12. heavy influencing factors
13. 1. microstructure
14. 2. average stress
15. 3. environment
16. Segment B
17. continuous mechanism (increasing band)

18. light influencing factors
19. 1. microstructure
20. 2. thickness
21. heavy influencing factors
22. 3. some combination of environment, average stress, and frequency
23. Segment C
24. static mechanism (cleavage, intergranular fiber)
25. heavy influencing factors
26. 1. microstructure
27. 2. average stress
28. 3. thickness
29. little influencing factor
30. 4. environment

II. MICROSCOPIC CHARACTERISTICS OF INITIAL CRACK PROPAGATION

Since Forsyth^[3] studied the fatigue propagation of aluminum alloys in the early sixties and divided it into the I and II propagating stages, a great deal of exploratory studies of the propagation behavior along the 45° crystallographic axis in the stage I of propagation have been carried out. Furthermore, some physical models were presented. The details are in Reference [2].

In the aspect of the microscopic morphology of fatigue crack in the metal propagation period, Hertzberg and Mills^[4] discovered that when the propagation rate was extremely low, the fracture showed a crystallographic facet or river pattern in their observation of the microfractography of Al, Cu, Ti and Ni alloys, and stainless steel. Since then, Beevers^[5] summarized the work done by previous workers. He listed the crystallographic directions of the facets produced in the initial propagation in over ten alloys. These facets are usually close to the densely packed crystallographic plane of the matrix, such as the {111} and {001} planes of a face centered cubic metal, the {110} and {001} planes of a body centered cubic metal, and {0001} plane of a tightly packed hexagonal metal. These facet fractures, which emerge under an extremely low propagation rate, had been believed to be due to the repeated slip in the local region at the tip of the crack. This causes the binding strength of atomic bonds between two neighboring slip surfaces to weaken. Therefore, the local slip surface created a cleavage fracture under a low tensile

stress.^[6] However, the fact that some of the facet directions of certain cubic metals appeared on the non-slip surface {001} was not explained.

However, when we considered the crystal structure, slip face energy (SFE), and modes of slip of metals and alloys, it was discovered that the orientation of these facets had a certain pattern^[7], as shown in Table 1.

1. 晶 格	2. 合 金	3. 层 错 能	4. 滑 移 类 型	5. 小平面位向
FCC	6. Al合金	11. 高	17. 波状	{001}
	7. Ni合金	12. 低	18. 平面	{111}
	8. 不锈钢	13. 低	19. 平面	{111}
BCC	Fe-3%Si	14. 高	20. 波状	{001}
	9. β 黄铜	15. 低	21. 平面	{011} $\pm 10^\circ$
HCP	10. Ti合金	16. 高	22. 波状	{0001} $\pm 5^\circ$

Table 1. Crystallographic orientations of facets on fracture surfaces

/15

1. lattice
2. alloy
3. SFE
4. mode of slip
5. orientation of facet
6. Al alloy
7. Ni alloy
8. stainless steel
9. β brass
10. Ti alloy
11. high
12. low
13. low
14. high
15. low
16. high
17. wavy
18. flat
19. flat
20. wavy
21. flat
22. wavy

From Table 1 one can see that it is favorable to show a cleavage fracture along the cubic plane for cubic metals with wavy slips and high SFE because it was easy for slips to occur. For example, certain cubic metals such as Fe-3%Si could be described by the fracture mechanism proposed by Cottrell^[8], i.e.,

$$-\frac{a}{2}(\bar{1}\bar{1}1) + \frac{a}{2}(11\bar{1}) \rightarrow a(001) \quad (A)$$

For other cubic metals (Ni-based alloys, stainless steel, and β brass, etc.), the aforementioned dislocation is difficult to occur due to the low SFE and planar slip. Consequently, cleavage only emerges along the slip surface^[7]. Recently, in the analysis of the mechanism of the initial propagation of fatigue crack by Lynch^[9], it was believed that the propagation of crack along the $\{001\}$ plane in the $\langle 110 \rangle$ direction is caused by the alternative slip of the tip of the crack in two $\{111\}$ planes, as shown in Figure 2.

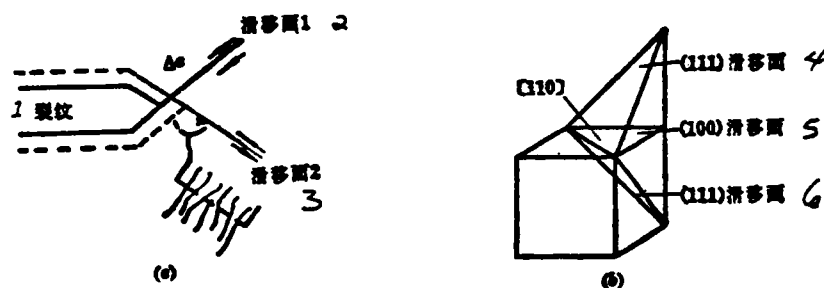


Figure 2. Schematic diagram of $\{100\}$ $\{110\}$ propagation by alternative slip in two $\{111\}$ planes at crack tip^[9]

1. crack
2. slip plane 1
3. slip plane 2
4. $\{111\}$ slip plane
5. $\{100\}$ slip plane
6. $\{111\}$ slip plane

In practical engineering materials, due to the influence of structure (the state and distribution of the second phase and impurities), environmental media, and stress, the microfractographic state during the initial stage of crack propagation is often various. Gerberich and Moody^[10], in their observation of the fracture morphologies of structural steel and titanium alloy, have pointed out that the microstructure of the fracture of these two materials in the initial propagation stage could be divided into the intragranular and intergranular type. Furthermore, it has nine patterns: (a) inclined cleavage; (b) degenerate cleavage; (c) crack between α/β phases; (d) α phase cleavage in α/β region; (e) intergranular crack in hard matrix; (f) intergranular crack in soft matrix; (g) elastic intergranular stripe; (h) grain boundary void created by point mass; and (i) linkage of intergranular crack, as shown in Figure 3. The first four types are intragranular forms and the latter five are intergranular forms.

Freudental^[11] believed that because there is always inhomogeneity and discontinuity in the local structure in a practical structural part and there are various distortions on the surface and in the inside, the microscopic mechanism of fatigue crack is primarily divided into the slip plane crack produced by the repeated slip of the soft metal and the shear crack of high strength alloy without slip. In the medium strength alloys, the /16 mechanism is a combination of both.

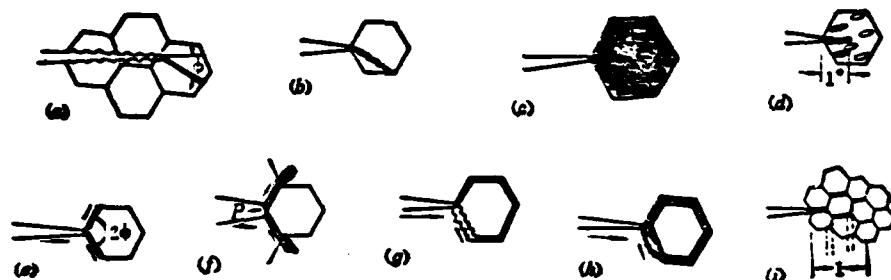


Figure 3. Types of microfractographs of fatigue crack propagation at initial stage^[10]

One can see that in practical engineering structural parts and specimens, the fracture structures are various. However, they also have a certain basic variation pattern. Ouyang Jie^[12] summed up eight types of fractures based on the orientation of cracks and fracture analysis of a large number of specimens and parts made of aluminum alloys, structural steel, and high temperature super alloys. Furthermore, he believed that these fractures could basically be described by the "alternative shear" mechanism and the "alternate tear-shear" mechanism. The author^[2] believed that, from a simple stress analysis, it belongs to the dual directional tensile plane stress type. In this case, because the tangential stresses on the slip plane cancel each other and the normal stress superimposes itself, it favors the occurrence of a facet type cleavage fracture.

III. MECHANICAL BEHAVIOR AND THRESHOLD VALUE IN INITIAL CRACK PROPAGATION STAGE

In recent years, in order to save energy, reduce material consumption, and improve product function, it is unavoidable to have notches and stress concentrating zones present in engineer-

ing structural parts. Especially certain components, such as rotor parts for an engine, gears, crankshafts, pressurized containers, etc., frequently sustain small amounts of low frequency heavy loads. In addition, the periodical inspection of these parts in long term operation is relatively difficult. For this reason, these parts are required to have an assurance of safe crack propagation (or no propagation). Consequently, a new important branch has been developed from "damage tolerance design" in product design, i.e., "safe crack design."^[13] Hence, the further study of mechanical behavior and threshold values of initial propagation of fatigue crack is seriously looked upon.

1. Fatigue Limit and Crack Propagation Threshold

Figure 4(a) is a schematic diagram of the stress-strain field on a notched specimen and the inception and propagation zone of fatigue crack. From the fatigue one can see that because of the presence of a relatively large plastic and elastic pressure stress field in front of the tip of the crack, the crack stops or propagates at an extremely low rate. Figure 4(b) is the schematic diagram of the relation between smooth and notched fatigue limits and the fatigue threshold stress.^[13]

Lukas^[14] pointed out that there were three fatigue limits at the present moment, i.e., crack propagation threshold (ΔK_{th}), fatigue stress limit (σ_a), and fatigue plastic strain limit (ϵ_{apc}). The latter two fatigue limits have the following relation, i.e.,

$$\sigma_a = K \epsilon_{apc}^n \quad (1)$$

where K and n are material constants. The fatigue threshold and fatigue stress limit also have a correlation. Assuming that $K_{a_{th}}$ is the basic threshold value, under the cycling of a symmetric stress, $K_{a_{th}} = \Delta K_{th}/2$. For a perforated crack, we can obtain that

$$K_{a_{th}} = 1.12 \sigma_a \sqrt{\pi a_e} \quad (2)$$

where a_e is the critical crack dimension. When the specimen has

a notch

$$K_{ts} = \sigma_{G_n} \sqrt{\pi a} F(a_n, K_t, \rho) \quad (3)$$

where σ_{G_n} is the notch fatigue limit, K_t is the notch stress concentrating coefficient, and ρ is the radius of the notch. The aforementioned formula can be written approximately as

$$\sigma_{G_n} = \frac{\sigma_s}{K_t} \left[1 + \frac{1.14}{\rho} \left(\frac{K_{ts}}{\sigma_s} \right)^2 \right]^{1/2} \quad (4)$$

with increasing strength, σ_G gradually increases and K_{atb} decreases. The second term in the parenthesis will also decrease. σ_{G_n} will be close to the value of σ_G/K_t . When ΔK_{th} is already known, the simplified formula can be applied in practical engineering.

Smith^[15] recently presented the correlation between the smooth and notched fatigue limits and the thresholds in a comprehensive analysis article regarding fatigue limits and threshold values. According to the usual fracture mechanics formula (LEFM), the threshold value (ΔK_{th}) is a function of the externally applied stress ($\Delta \sigma$) and the crack length (a). When a crack begins to propagate

$$\Delta K_{ts} = f \Delta \sigma \sqrt{\pi a} \quad (5)$$

where f is the calibration coefficient of the geometric dimension when a penetrating crack is formed on the surface.

$$K_I = 1.12 \Delta \sigma \sqrt{\pi a} \quad (6)$$

In order to make the crack not propagate, it is necessary that

$$\Delta K_{ts} > 1.12 \Delta \sigma \sqrt{\pi a} \quad (7)$$

From the aforementioned formula one can see that when the crack length is very small, it is necessary to apply a larger stress amplitude to make the crack propagate. In Figure 5, the threshold value ΔK_{th} of a long crack can be expressed by a straight line with a slope of $-1/2$, i.e.,

$$a_s = 0.25 \left[\frac{\Delta K_{ts}}{\Delta \sigma_s} \right]^2 \quad (8)$$

For soft steel ($\Delta K_{th} = 9.9 \times 10^6 \text{ NM}^{-3/2}$, $\Delta \sigma_0 = 240 \times 10^6 \text{ NM}^{-1/2}$), a_0 is approximately 0.2mm. For hardened steel ($\Delta K_{th} = 3.4 \times 10^6 \text{ NM}^{-3/2}$, $\Delta \sigma_0 = 670 \times 10^6 \text{ NM}^{-1/2}$), a_0 is only 0.005mm. This is why the surface scratches will greatly reduce the fatigue lifetime. This is because the presence of scratch may reduce or even eliminate the inception and initial propagation stages of cracks.

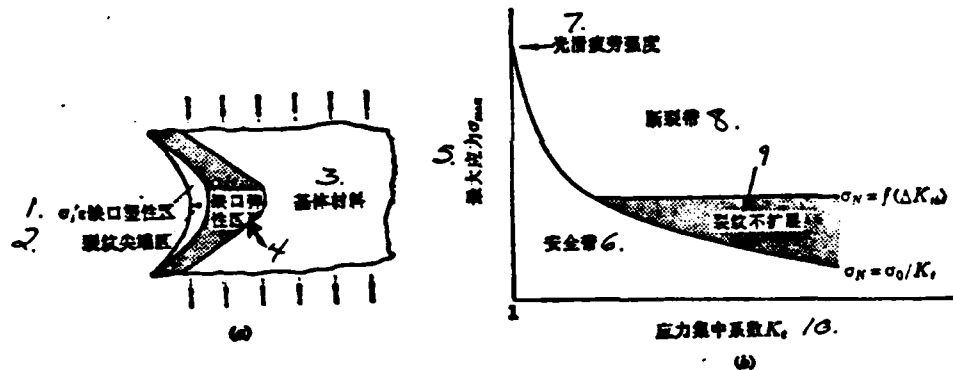


Figure 4. (a) Stress/strain field in a notched specimen and (b) relationship of fatigue limit of plain, notched specimens and threshold stress.^[13]

1. σ/ϵ notch plastic region
2. crack tip region
3. base material
4. notch elastic region
5. maximum stress σ_{max}
6. safe band
7. plain fatigue strength
8. fracture band
9. crack not propagating
10. stress concentrating coefficient K_t .

In the meantime, one can also see that when the crack length is less than a_0 , some of the formulas established in continuous mechanics (LEFM) are no longer applicable. In this case, the crack propagation pattern is different from the one observed with long cracks, as shown in Figure 5(b). This phenomenon was also proven by the experimental results recently published by Romaniv et al. [16] When the crack length exceeded its critical value (a_s^0), ΔK_{th} was not related to the crack length. They also [18] gave the correlating formula between the short crack threshold value (ΔK_{th}^{sh}) and the long crack threshold value (ΔK_{th})

$$\Delta K_{th}^{sh} = \Delta K_{th} \left(\frac{a'}{a_s^0} \right)^r \quad (9)$$

where r is a material constant.

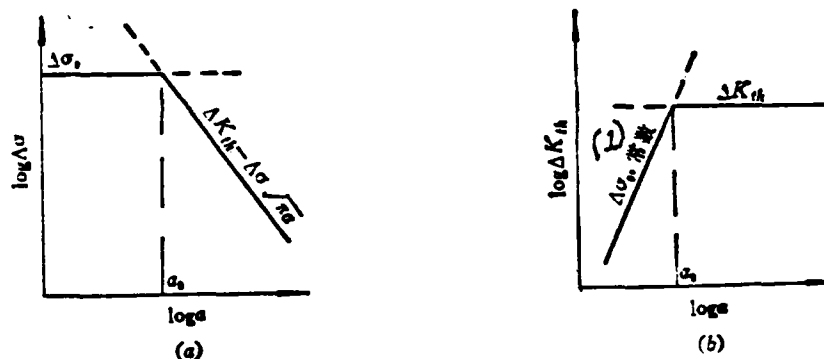


Figure 5. (a) Transition from fatigue limit of a plain specimen to K_{th} of a long crack and (b) its effect on the measurement of threshold value [15]

1. $\Delta \sigma_0$ constant

2. Propagation Behavior of Short Cracks

Kitagawa and co-author [17] have studied the threshold stress of structural steel rod specimens of various strength levels with microcracks on the surface, and obtained the following correlation

$$\Delta \sigma_{th} = \frac{\Delta K_{th}}{f(a)\sqrt{\pi a}} \quad (10)$$

where $f(a)$ is a function related to the crack size and specimen geometry.

El Haddad et al^[17,18] also further verified this phenomenon using a notched thin plate CSAG40-11 steel specimen. In order to make the method of LEFM fracture mechanics effective, they introduced a constant l_0 for correction, i.e.,

$$\Delta K = \Delta \sigma \sqrt{\pi(a + l_0)} F \quad (11)$$

where F is the coefficient related to the geometrical size of the specimen. For a small penetrating crack, F is approximately equal to 1. When a is approximately zero, $l_0 \gg a$, $\Delta \sigma = \sigma_L$, and $\Delta K = \Delta K_{th}$. We obtained a correlation similar to equation (8).

$$l_0 = \frac{1}{\pi} \left(\frac{\Delta K_{th}}{\Delta \sigma} \right)^2 \quad (12)$$

When considering a crack near the surface using 1.12 as the coefficient, equation (8) is basically in agreement with (12). By substituting equation (11) into the above formula, we can obtain the general formula for the threshold stress ($\Delta \sigma_{th}$) at any crack length.

$$\Delta \sigma_{th} = \frac{\Delta K_{th}}{\sqrt{\pi(a + l_0)}} \quad (13)$$

Figure 6 shows the curve correlating the fatigue threshold stress and the crack length of G40-11 steel.^[17] One can see that when $l_0 = 0.24\text{mm}$, the estimated value agrees with the experimental results well. With regard to the physical significance of l_0 , it is not clear at the present moment. It may be related to the stress-strain field at the tip of the crack.

Topper and El Haddad^[19] obtained a similar formula for the /19 propagation of a short crack through an analysis of the initial propagation of fatigue cracks on notched specimens.

$$\Delta \sigma_{th} = \frac{\Delta K_{th}}{K' \sqrt{\pi(l + l_0)}} \quad (14)$$

where K' is the elastic stress concentrating coefficient, and l is the crack length. The above formula can be written as

$$\Delta\sigma_{th} = \frac{F\Delta\sigma_e}{K'} \sqrt{\frac{l_0}{l+l_0}} \quad (15)$$

For the center or edge notch with a depth c

$$K' = \sqrt{\frac{l+c}{l}} \quad (16)$$

When l approaches zero, K' is close to $1.12 K_{to}$.

From equations (15) and (16) one can get that

$$\Delta\sigma_{th} = F\Delta\sigma_e \sqrt{\frac{l}{l+c}} \sqrt{\frac{l_0}{l+l_0}} \quad (17)$$

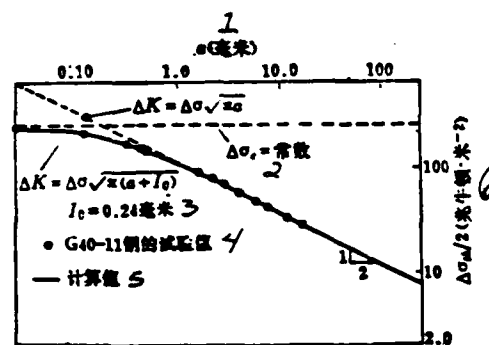


Figure 6. Fatigue threshold stress versus crack length for a G40-11 steel [17]

1. σ (mm)
2. $\Delta\sigma = \text{constant}$
3. $l_0 = 0.24 \text{ mm}$
4. experimental value of G40-11 steel
5. calculated value
6. $\Delta\sigma_{th}/2$ ($10^6 \text{ N}\cdot\text{m}^{-2}$)

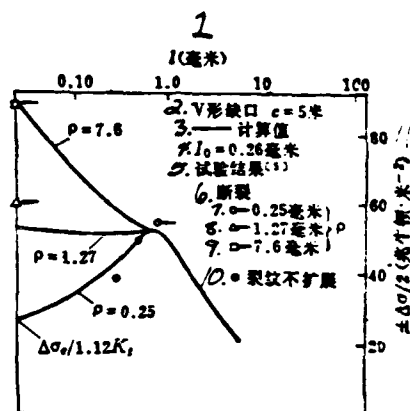


Figure 7. Comparison of calculated curves with the experimental data [18]

1. l (mm)
2. V-shaped notch $c=5\text{mm}$
3. calculated value
4. $l_0=0.26\text{mm}$
5. experimental results [5]
6. fracture
7. 0.25mm
8. 1.27mm
9. 7.6mm
10. crack not propagating
11. $\pm\Delta\sigma/2$ (10^6 N.M^{-2})

$$\Delta\sigma_r = \frac{F\Delta\sigma_0}{1 + \sqrt{c/l_0}} \quad (18)$$

Figure 7 shows the comparison of the experimental values with calculated values obtained using equations (15) and (18) for specimens with various notch diameters (ρ) (V shaped notch, depth $c=5\text{mm}$, $l_0=0.29\text{mm}$).

For a "sharp notch," the crack inception stress is

$$\Delta\sigma_r = \Delta\sigma_0/K_t \quad (19)$$

This stress increases as l extends until reaching its maximum value. /20

For a "dull notch", this stress decreases with increasing l (or equal to the initial stress), i.e.

$$K_i = 1 + 2\sqrt{c/\rho} \quad (20)$$

The boundary line of the two types of notch is $\rho_{cr} = 4l_0$. From equation 20 we can obtain

$$K_{ic} = 1 + 2\sqrt{c/\rho_{cr}} \quad (21)$$

Then

$$c_{cr} = (K_{ic} - 1)^2 l_0 \quad (22)$$

Figure 8 shows the initial short crack propagation behavior of notches of various geometrical shapes.^[18]

Hudak Jr.^[48] had given the following preliminary conclusions through an analysis of short crack propagation behavior:

(1) Using the general fracture mechanical analysis method (LEFM), the propagation behavior of a short crack is different from that of the long crack. The primary reason is that the assumption in the conventional continuous mechanics is already no longer applicable.

(2) A short crack might propagate below the crack size estimated and stress level applied for a long crack.

(3) The growth rate of a short crack is higher than that of the growth rate of a long crack predicted by the data $da/dN = \Delta K$.

(4) The actual propagation behavior of a short crack should take into account of a constant length l_0 on top of the actual crack size. At the present moment, the physical meaning of l_0 is not understood. However, it can be used to adequately measure the threshold value of a short crack and its propagation behavior.

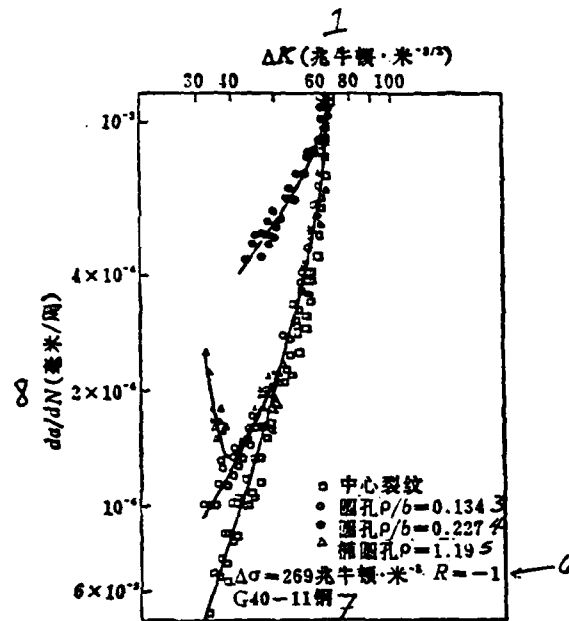


Figure 8. Propagation behaviors of short crack at notches with different geometry [18]

1. $\Delta K (10^6 \text{ N.M}^{-3/2})$
2. center crack
3. circular hole $\rho/b=0.134$
4. circular hole $\rho/b=0.227$
5. elliptical hole $\rho=1.19$
6. $\Delta\sigma=269 \times 10^6 \text{ N.M}^{-2}$, $R=-1$
7. G40-11 steel
8. $da/dN (\text{mm/week})$

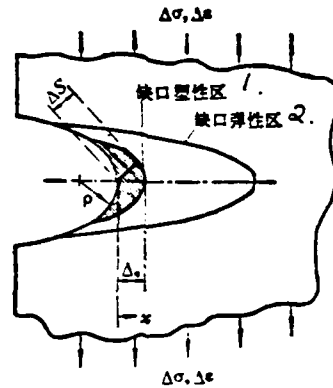


Figure 9. Elastic and plastic stress-strain field at the root of a notch [21]

1. notch plastic region
2. notch elastic region

Miller and his co-authors [20,21] had questioned the aforementioned analysis. They believed that the physical meaning of introducing the constant l_0 was not clear. The various propagation behaviors of some short cracks below $\Delta\sigma_e$ could not be predicted using equation (11). In addition, l_0 could not have been a constant because it was related to the level of applied stress. For this reason, they proposed a model using a local plastic shear model to describes the inception and initial propagation of a crack, as shown in Figure 9. In the figure, ΔS is the plastic tangential displacement of the notch. It is a function of stress level, cycle, yield strength, and notch size and shape.

When a crack enters the plastic region, the shear displacement $\{\phi_c\}$ of the crack tip can be considered to originate from the plastic tangential displacement $\{\phi_p\}$ caused by the notch plastic region. This tangential displacement decreases as the crack penetrates into the plastic region. In addition, the plastic distortion produced by the strangeness of the crack tip /21 (ϕ_e) must be added (which can be obtained according to the LEFM

analysis). Therefore

$$\phi_t = \phi_p + \phi_e \quad (23)$$

They believe that the critical value of ϕ_t for the inception and propagation of a crack could be

$$\phi_{tcr} = \frac{\Delta K_{th}}{\sqrt{2} E \Delta \sigma_{cy}} \quad (24)$$

where $\Delta \sigma_{cy}$ is the cyclic yield strength. When a crack begins to grow from a notch, the rate of decrease of ϕ_p might be faster than ϕ_e . Consequently, the situation that $\phi_t < \phi_{th}$ will appear, as shown in the $|\phi|_{e2}$ curve in Figure 10. Thus, a non-propagating crack is generated.

In summary, in regard to the propagation and mechanism of a short fatigue crack in the initial stage, it is still in the developmental stage. It is awaiting further experimental work and more profound theoretical analysis.

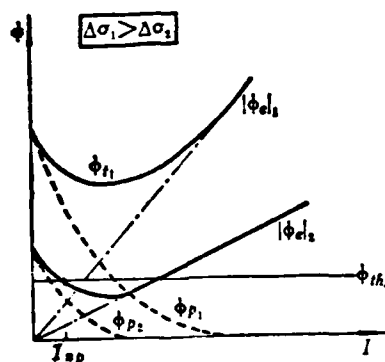


Figure 10. Schematic of fatigue crack propagation behavior at a notch under various stress levels[21]

IV. SOME FACTORS AFFECTING INITIAL PROPAGATION OF CRACKS

1. Effect of Stress Ratio

Among the factors affecting the initial crack propagation behavior and threshold value, it is generally believed that the stress ratio R is one of the important factors.^[22] The increase in R will cause the decrease of the initial propagation rate and threshold value.

With regard to the effect of the ratio R or the average stress on the ΔK_{th} value in a relatively low propagation rate range, it is usually expressed by the following formula.^[23]

$$\Delta K_{th} = \Delta K_{th0} (1 - R)^r \quad (25)$$

where r is a material constant. ΔK_{th0} is the threshold value when $R=0$. It is obvious that the above formula is only applicable to the range where R is positive. Kaisand and Mowbray^[24] had given a generalized formula which agrees with the experimental data well,

$$\Delta K_{th} = \Delta K_{th0} f(R) \quad (26)$$

when $R > 0$

$$f(R) = \left(\frac{1 - R}{1 + R} \right)^{1/3} \quad (A)$$

when $R < 0$

$$f(R) = \left(\frac{1 - R}{1 + \frac{R}{3}} \right)^{1/3} \quad (B)$$

That means when R is negative, they assumed that it was in a loaded cycle. Only the R values in the 1/3 compression portion are effective to the propagation of cracks.

There have been some different explanations regarding the /22 effect of the stress ratio R on the da/dN of the initial crack and the threshold value. Klesnil and Lukas^[25] believed that the load experience is an important factor for structural steel. They also pointed out that the effect of R on the threshold value is caused by the compressive stress in the plastic region on the tip of the crack. Schmidt and Paris^[26], however, adopted the crack closure effect to explain the effect of R on the threshold

value.

For a low stress value, $K_{min} < K_{CI}$

$$K_{max} = K_{CI} + \Delta K_0 = \text{constant} \quad (27)$$

$$\Delta K_{th} = K_{max} - K_{min} = K_{max} (1 - R) \quad (28)$$

For a high stress ratio, $K_{min} \geq K_{CI}$

$$\Delta K_{th} = \Delta K_0 = \text{constant} \quad (29)$$

$$K_{min} = \frac{\Delta K_{th}}{1 - R} = \frac{\Delta K_0}{1 - R} \quad (30)$$

The above relations have been verified in 2024-T3 aluminum alloy, A533 steel, and T-1 titanium alloy. Experimental results pointed out that the load frequency has a certain effect on the aluminum alloy crack closure stress strength factor K_{CI} and ΔK_{th} . At a low stress ratio, the effect of frequency on K_{max} is not too large. [27]

Radon [28] had discovered that the effect of R was related to the thickness of the specimen in his study of BS-4360 low alloy steel at near-threshold range. For a relatively thin specimen ($B = 12\text{mm}$), the effect was more apparent. In a 50mm thick specimen, however, the effect of R was not too large. This phenomenon might be related to the stress state of the specimen and the closure effect.

In addition, the prestrain also has different effects on the threshold values of carbon steel at various R ratios (see Figure 11). Blacktop et al [29] believed that at a low stress ratio the effect of cold work might be related to the size of the plastic zone of the crack tip. Simultaneously, they also pointed out that according to the following formula [30]

$$\Delta K_{th} = E_s \sqrt{2\pi \rho_{pl}} \quad (31)$$

the prestrain will cause the ϵ_f in the equation to decrease. Consequently, the threshold value will decrease.

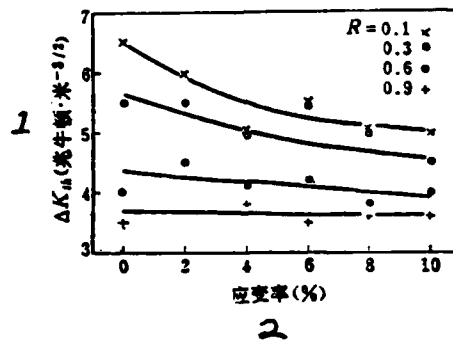


Figure 11. Effect of prestrain on ΔK_{th} at different stress ratios, R , in a plain carbon steel (0.1C-1.5Mn) [29]
 1. ΔK_{th} (10⁶ N.M^{-3/2})
 2. strain rate (%)

2. Effect of Microstructure

With regard to the effect of grain size on the initial crack propagation behavior and threshold value, a great deal of experimental data and many empirical formulas have been published to date. For example, Kitagawa et al [31] had discovered that ΔK_{th} and σ_y had the following relation in testing a low strength alloy steel

$$\Delta K_{th} = AE - B\sigma, \quad (32)$$

where A and B are experimental constants. Beevers [5] proposed the following empirical formula in his study of the effect of grain size (d) on the threshold value of a manganese steel

$$\Delta K_{th} = 3.8 + 1.4 \times 10^3 d^{1/2} \quad (33)$$

and

$$\sigma_s = 139 + 0.347 d^{-1/2} \quad (34)$$

Taira et al^[32] pointed out that ΔK_{th} increased with increasing grain size ($d^{1/2}$) in their study of the effect of grain size on the threshold value of a low carbon steel. Furthermore, a computation formula was given for the effective threshold (K_{effth}) and grain size $d^{1/2}$.

$$\Delta K_{effth} = 0.19 + 1.96 \times 10^{-2} \sqrt{d} \quad (35) / 23$$

where $\Delta K_{eff} = K_{max} - K_{Op}$. They discovered that the crack tip slip belt region ϵ_s increases with the grain size (d), i.e., $\epsilon_s = 0.51d$. The $da/dN - \Delta K$ curve of various grain sizes approaches a straight line if it is expressed by ΔK_{eff} , as shown in Figure 12.

Gerberich and Moody^[10] also pointed out that the slope of the $\Delta K_{th}/E - d^{1/2}$ curve of different materials showed a positive and a negative type through an analysis of the experimental data of structural steels and titanium alloys of different strength levels, as shown in Figure 13.

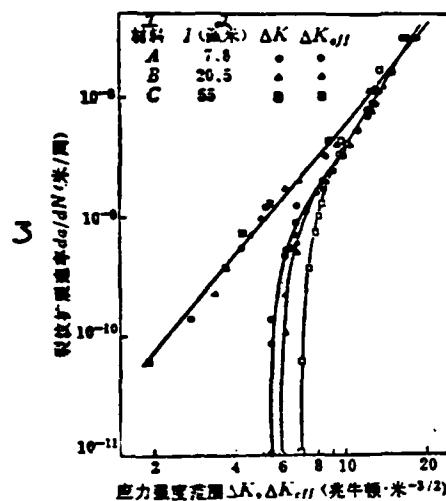


Figure 12. The da/dN - ΔK curve for low carbon steel with various grain size[32]

1. material
2. (micron)
3. crack propagation rate da/dN (m/week)
4. stress strength range $\Delta K, \Delta K_{eff}$ ($10^6 \text{ N.M}^{-3/2}$)

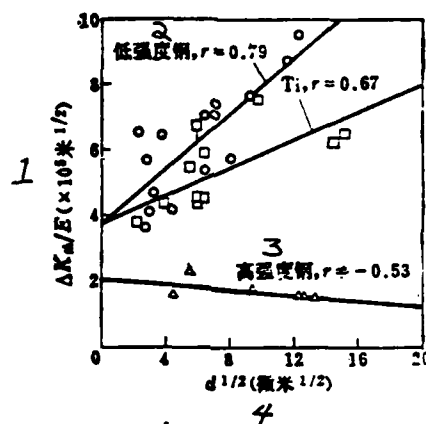


Figure 13. $\Delta K_{th}/E$ versus $d^{1/2}$ curves of various materials [10]

1. $\Delta K_{th}/E (\times 10^5 m^{1/2})$
2. low strength steel, $r = 0.79$
3. high strength steel, $r = -0.53$
4. $d^{1/2}$ (micron^{1/2})

From the results mentioned above, one finds out that it is not enough to only consider the grain size. It is also necessary to analyze the internal microstructure and morphology. Gu Hai-cheng and Knott^[33] gave the following correlation

$$\Delta K_{th} = (\pi \rho^*/2)^{1/2} \sigma_f(R) \quad (36)$$

They believed that the threshold value is not only related to the tensile strength (σ_u) of the material, but also correlated to the "spacing" parameter (ρ^*) of the structure (i.e., Neuber material constant). The increase in the tensile strength frequently brings about a decrease in the structural spacing parameter. Consequently, certain types of steel may show a peak value of ΔK_{th} at different temper temperatures.

As for the multi-phase metallographic aspect, Masounave et al^[34] studied the fatigue crack propagation behaviors of various ferrites (α) and pearlites (p) in carbon steel. They pointed out that the following relation between ΔK_{th} and the microstructure

$$\Delta K_{th} = f_{\alpha}^2 \phi_{\alpha} + (1 - f_{\alpha}^2) \phi_p \quad (37)$$

where f_{α} is the percentage of ferrite by volume. ϕ_{α} and ϕ_p represent the action function of ΔK_{th} with respect to α and p .

$$\phi_{\alpha} = \Delta K_0 + K_f d^{\frac{1}{2}} \quad (38)$$

$$\phi_p = \Delta K = \text{constant} \quad (39)$$

The author and co-workers^[35] discovered that the functional relation between ΔK_{th} and the microstructure can be approximately expressed by the following empirical formula in the determination of a threshold value of a high strength steel after different temperature treatments:

$$\Delta K_{th} = 1.95 f_M + 7.53 f_B + 14.1 f_A \quad (40)$$

where f_M , f_B , and f_A are the volumetric percentages of tempered martensite, bainite and residual austenite, respectively. From the above formula one can see that the contribution of different microstructures to ΔK_{th} is not the same, i.e., M:B:A is approximately equal to 1:4:7. This estimation is approximately equivalent to the contribution of the 10% residual austenite in 4340 steel to the plastic distortion energy studied by Schwalbe.^[36] In addition, through the determination of the lattice distortion, dislocation density, residual stress, and microscopic hardness of the surface layer structure also significantly affected the fatigue crack propagation and the threshold value.^[35,37]

Brown and Smith^[38] discovered that the corresponding relation between ΔK_{th} and \sqrt{GS} in α equi-axed structure alloys with residual β phase was not as apparent as that of a low strength steel in studying the effect of microstructure and crystal

orientation on the threshold of Ti-6Al-4V. However, the specimen T-L perpendicular to the (0001) surface and the specimen L-T parallel to the (0001) surface have different initial crack propagation behaviors. For the latter, when $\Delta K \approx 3.5 \times 10^6 \text{ Nm}^{-3/2}$, a crack propagation threshold value has still not been found.

Looking at the experimental results mentioned above, the effect of the microstructure on the initial crack propagation and the threshold value is very complicated. Some explanations have been given. In general, it is believed to be closely related to the reverse plastic zone size (r_y),

$$r_y = \frac{1}{6\pi} \left(\frac{\Delta K}{\sigma_y} \right)^2 \quad (41)$$

The relative dimension between r_y and the microstructure is an important factor affecting the initial crack propagation and threshold.

Irving and Beevers^[39] believed that the growth of a crack became structure sensitive from structure insensitive as the size of the plastic zone reached the microstructure dimension when they studied the effect of the microstructure of the Ti-6Al-4V titanium alloy on fatigue crack propagation. Kao and Byrne^[40] also pointed out that the cementite spacing in pearlite steel is the smallest microstructure unit. It has a primary induction effect on the fatigue crack propagation of steel. The effect of the original austenite grain size and its grain boundary on the crack propagation in the near threshold range belongs to a secondary type. Furthermore, the spacing determines the free mean distance of the crack leading edge propagation displacement. A decrease in the spacing limits the displacement of the leading edge of a crack. Consequently, its propagation rate is reduced. This effect is even more apparent at the near-threshold range.

3. Effect of Environmental Media

Among all the influencing factors, the effect of environmental media is a subject which attracts a lot of attention presently and is very complex. In the past, because of the lack

of experimental results in the initial crack propagation stage, some mechanisms in the middle and late stages of crack propagation (such as metal dissolution and hydrogen embrittlement) were frequently used to explain it. Recently, Ritchie^[1] summarized the following points according to the experimental results obtained in the aspect of the effect of environmental media on the behaviors in the initial crack propagation period and in the threshold range:

- (1) the effect primarily occurs in a low stress ratio condition
- (2) as compared with the results obtained in laboratory air, the dry inert atmosphere accelerates da/dN and it decelerates in water.
- (3) for a high strength steel, the propagation in dry hydrogen is lower than that in laboratory air.

Figure 14 shows the propagation behaviors of 2½ Cr-1Mo bannitic steel in moist air and dry hydrogen environment at various stress ratios and frequencies. One can see that the effect of hydrogen on crack propagation appeared in two regions, i.e., at a medium rate ($da/dN \sim 10^{-5}$ mm/week) and around the threshold value ($da/dN < 10^{-6}$ mm/week) (41).

The effect of the environment on the crack propagation of 300M high strength steel is slightly different, as shown in Figure 15. When the rate is higher than 10^{-6} mm/week, hydrogen causes an acceleration ($f=5\text{Hz}$). When it is lower than 10^{-6} mm/week, dry hydrogen reduces the initial crack propagation rate by 16%.^[43] Such a decrease is also shown in other high strength rotor steels.^[44] In the salt mist test of high strength steel, such a decreasing effect was also observed. The effect of dry hydrogen on the crack propagation behavior of structural steel is schematically shown in Figure 16.

The mechanism concerning the effect of the environmental media on the initial crack propagation could be approximately divided into two main groups, i.e., the hydrogen embrittlement model and the crack closure model. Although the former successfully described the behavior of a fatigue crack at a medium or

relatively high propagation rate, yet according to the experimental results described above there

/25

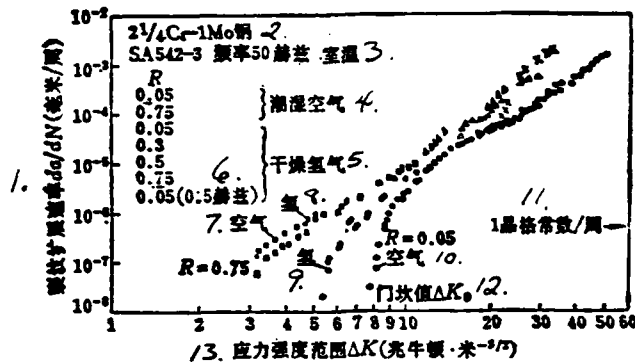


Figure 14. Fatigue crack propagation behavior in moist air and dry hydrogen for a bainitic SA542-3 steel^[41]

1. crack propagation rate da/dN (mm/cycle)
2. $2\frac{1}{4}$ Cr-1Mo steel
3. SA542-3 frequency 50Hz, room temperature
4. moist air
5. dry air
6. (0.5 Hertz)
7. air
8. hydrogen
9. hydrogen
10. air
11. crystal lattice constant/week
12. threshold value ΔK_0
13. stress strength range $\Delta K(10^6 \text{ N.M}^{-3/2})$

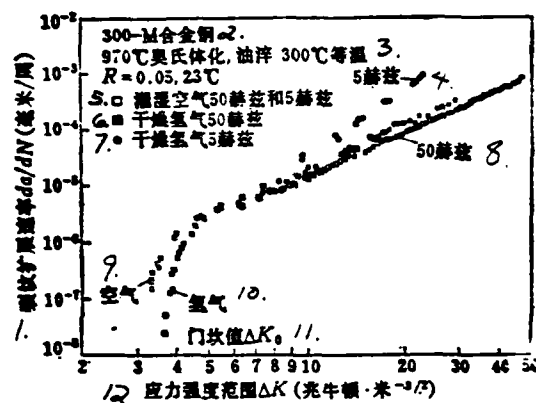


Figure 15. Fatigue crack propagation behavior in moist air and dry hydrogen for a high strength 300-M steel (300°C temper) [1]

1. crack propagation rate da/dN (mm/cycle)
2. 300-M alloy steel
3. 970°C Austenite, oil quenched, 300°C isothermal
4. 5 Hz
5. moist air, 50Hz, and 5Hz
6. dry hydrogen 50Hz
7. dry hydrogen 5Hz
8. 50Hz
9. air
10. hydrogen
11. threshold ΔK_0
12. stress strength range $\Delta K (10^6 \text{ N.M}^{-3/2})$

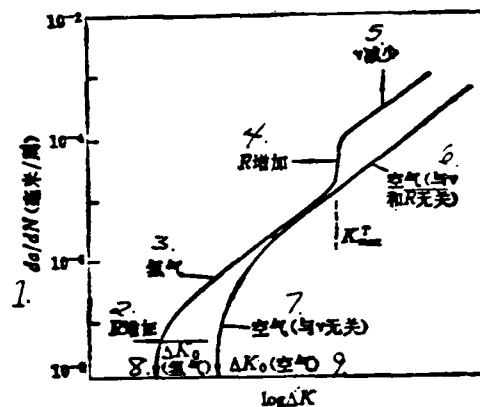


Figure 16. Schematic diagram of the effect of dry gaseous hydrogen on fatigue crack propagation in low strength steels [1]

1. da/dN (mm/cycle)
2. increasing R
3. hydrogen
4. increasing R
5. decreasing r
6. air (not related to r and R)
7. air (not related to r)
8. ΔK_0 (hydrogen)
9. ΔK_0 (air)

is obviously another mechanism present. For this reason, the emphasis is placed on the crack closure model. /26

In the recent two years, Ritchie and co-worker^[1,45] presented two models for the crack closure effect, i.e., the "oxide induced" and "roughness induced" closure models, based on the great deal of experimental results obtained for the effect of environmental media on alloy steels and high strength steels. The schematic diagrams for the two models are shown in Figure 17. The former is the foreclosure caused by the accumulation of oxides, while the latter is caused by the roughness of the fracture together with the second type shear displacement. Apparently, the closure caused by plastic distortion crushes the

oxide film and creates some fresh surface. Consequently, the oxide film is thickened. They found that the oxide film of 4½ Cr-2Mo steel near the threshold could reach 0.2mm^{-3} , which is approximately twenty times higher than the thickness in the medium and high propagation rate regions. The thickness of the corrosion product in dry hydrogen, however, is only $50\sim 150\text{\AA}$. At a high stress ratio, Type II displacement will cause "corrosion-oxidation" to significantly reduce the thickness of the oxide layer. Figure 18 shows the variation curves of the oxide layer thicknesses and da/dN of the two types of steel mentioned above versus the crack length as measured by an Auger Spectrometer.

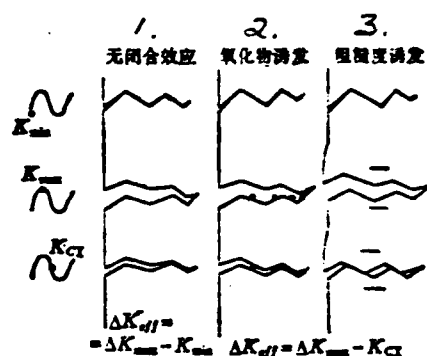


Figure 17. Schematic of the mechanism for near-threshold fatigue crack propagation^[1]

1. no closure effect
2. oxide induction
3. roughness induction

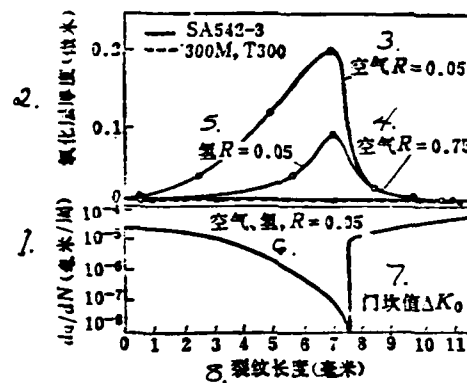


Figure 18. Auger measurements of crack flank oxide thickness in $2 \frac{1}{4}$ Cr-1Mo and 300-M steels as a function of crack length and da/dN [42]

1. da/dN (mm/week)
2. oxide layer thickness (micron)
3. air $R=0.05$
4. hydrogen $R=0.05$
5. air $R=0.75$
6. air, hydrogen, $R=0.05$
7. threshold ΔK_0
8. crack length (mm)

Suresh et al [45] also derived a calculation formula for the crack closure stress strength factor K_{cl}

$$K_{cl}|_{x=0} = \frac{dE}{4\sqrt{\pi l}(1-\nu^2)} \quad (42)$$

where d is the maximum thickness of the oxide layer, and $2l$ is the distance from the maximum thickness point to the tip of the crack. $E/(1-\nu^2)$ is the effective elastic modulus under a plane strain condition. The calculated values obtained using equation (42) are in approximate agreement with the experimental values.

Figure 19 shows the 1:1 corresponding relation between the maximum oxide layer thickness and the crack tip opening displacement (CTOD) plotted using some experimental data of 2½ Cr-1Mo steel in the atmosphere, hydrogen, helium, and water. A large microstructure or a high contaminant content may produce a rough or facet fracture surface to promote the occurrence of the "roughness induced" closure. This result agrees with the observation^[46] that a large "mismatch" existed in the fracture surface of a large α titanium structure in the crack propagation near the threshold as reported by early workers.

The above was a discussion on some major factors concerning the initial crack propagation behavior. In reality, other factors such as load history, frequency, amplitude, load type, and testing method, as well as the combined effect of various factors, must be seriously considered. Due to the limitation in page number, they cannot be individually listed. Some of the recently published overall review literature such as [1, 2, 47, 48] should be referred to. /27

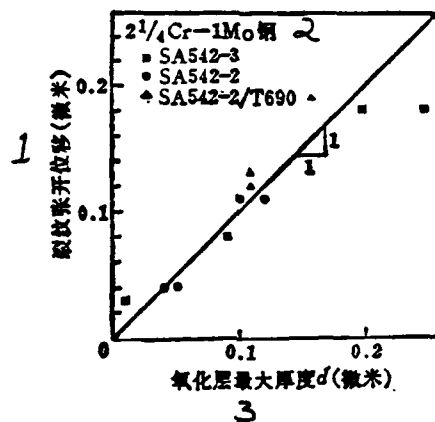


Figure 19. Showing the 1:1 correspondence of maximum oxide thickness with crack tip opening displacement (CTOD) for $2\frac{1}{4}$ Cr-1Mo steel in air, hydrogen, helium and water[1]

1. crack tip opening displacement (micron)
2. $2\frac{1}{4}$ Cr-1Mo steel
3. maximum oxide layer thickness d(micron)

V. CONCLUSIONS

In this paper, a brief review was carried out regarding the results of recent studies of metal fatigue crack propagation behaviors and fatigue threshold values. Some analysis and discussion were made on the microscopic characteristics, mechanical behavior, and its major affecting factors of the initial crack propagation process. Because crack propagation in the near threshold range is structure sensitive, also because of the significant effect of the environment (media, temperature), the load condition and the testing method, it is necessary to seriously distinguish and analyze the experimental results and data published. For example, the humidity in the atmosphere has a strong effect on certain materials (such as structural steel). In the determination of the initial crack propagation rate and the

threshold and its application in engineering, we must seriously consider some of the influencing factors and the combined effect. In the area of experimental plan design, it is necessary to sufficiently combine the operating conditions of the products such as the environment, temperature, stress ratio, etc. to find the characteristics and patterns under specific conditions. In the meantime, it is also necessary to combine the microstructure with the macrostructure, and to combine the materials, techniques, to the structure, in order to find the general pattern, to develop the application of fracture mechanics, and to explore ways to improve the fatigue characteristics of materials and structural parts. It can then be made to more effectively guide product design, scientific studies, and production to better serve the economic construction for the people.

During the organization process of this report, assistance was received from comrades Liu Caimu, Zhang Shijie, Ouyang Jie, and Yuan Gaoming, as well as the people in the information office. I want to express my gratitude here.

REFERENCES

- [1] Ritchie, R.O., A paper presented at Intern. Symp. on Fatigue Thresholds, Stockholm, (1981).
- [2] Yan Minggao, "Law of Metal Fatigue Crack Propagation and Its Micromechanism," HK 80075, CAE, (1980)
- [3] Forsyth, P.J.E., Proc. Roy. Soc., A242, (1975), 198.
- [4] Hertzberg, R.W. and Mills, W.J., ASTM STP 600, (1976), 220.
- [5] Beevers, C.J., Metals Science, Aug/Sept., (1977), 362.
- [6] Gell, M. and Leverant, G.R., Acta. Met., 16, (1968), 553.
- [7] Yan Minggao, and Wang, Zongguang, Proc. 1st China-USA Bi-lateral Metall. /28
- [8] Cottrell, A.H., Trans. AIME, 44, (1958), 192.
- [9] Lynch, S.P., ASTM STP 675, (1979), 174.
- [10] Gergerich, W.W. and Moody, N.R., ASTM STP 675, (1979), 292.
- [11] Freudental, A.M., Eng. Frac. Mech., 6, (1974), 775.
- [12] Ouyang Jie, Aeronautical Materials, (1978), No. 4.
- [13] Wanhill, R.J.H., Proc. Intern. Symp. on Fatigue Thresholds, Stockholm, (1981), Vol.1, No. 3.

- [14] Lukas, P., same as above, Vol. 1, No. 10.
- [15] Smith, R.A., same as above, Vol. 2, No. 29.
- [16] Romaniv, O.N. et al, same as above, Vol. 3, No. 45.
- [17] Kitagawa, H. and Takahashi, S., Proc. ICM-2, ASM, Cleveland, (1967), 627.
- [18] El Haddad, M.H. et al, J. Eng. Met. Tech., ASME, 101, (1979), 42, Intern. J. Frac., 16, (1980).
- [19] Topper, T.H. and El Haddad, M.H., Proc. Intern. Sump. on Fatigue Thresholds, Stockholm, (1981), Vol. 1, No. 7.
- [20] Hommouda, M.M. and Miller, J.J., ASTM STP 668, (1979), 703.
- [21] Hommouda, M.M., Smith, R.A. and Miller, K.J., Fat. Engng. Mater. Struct., 2, (1979), 139.
- [22] Bathies et al, same as above, 4, (1981), 1.
- [23] Klesnil, M. and Lukas, P., Mater. Sci. Engng., 9, (1972), 703.
- [24] Kaisand, L.R. and Mowbray, D.F., J. Testing and Evaluation, 7, (1979), 270.
- [25] Klesnil, M. and Lukas, P., Eng. Frac. Mech., 4, (1972), 77.
- [26] Schmidt, R.A. and Paris, P.C., ASTM STP 536, (1973), 79.
- [27] Nelson, D.V., Experimental Mech. 17/2. (1977), 41.
- [28] Radon, J.C., Proc. Intern. Symp. on Fatigue Thresholds, Stockholm, (1981), Vol. 1, No. 4.
- [29] Blocktop, J. et al, same as above, 4, (1981), 1.
- [30] Yu, Chonghua and Yan, Minggao, Fat. Engng. Mater. Struct., 3, (1980), 189.
- [31] Kitagawa, H., Nishitani, H. and Matsumets, J., Proc. ICF-3, V-4, (1977).
- [32] Taira, S. et al, ASTM STP 675, (1979), 135.
- [33] Gu, Haicheng and Knott, J.F., Proc. Intern. Symp. on Fatigue Threshold, Stockholm, (1981), Vol. 2, No. 30.
- [34] Masounave, J. and Bailon, Proc. ICM-2, Boston (1976), 513.
- [35] Yan Minggao, Gu Mingda, and Liu, Caimu, Proc. Inter. Symp. on Fatigue Thresholds, Stockholm, (1981) Vol. 2, No. 23.
- [36] Schwalbe, K.H., Engng. Frac. Mech., 9, (1977), 795.
- [37] Wang, Renzhi, Li, Xiangbin, Tan, Yonggui and Yan Minggao, Proc. 1st Intern. Conf. on Shot-peening, France, (1981).
- [38] Brown, C.W. and Smith, G.C. Proc. Intern. Symp. on Fatigue Thresholds, Stockholm, (1981), Vol. 1, No. 16.

- [39] Irving, P.E. and Beevers, C.J., Mater. Sci. Engng., 14, (1974) 229.
- [40] Kao, P.W. and Byrne, J.G., Proc. Intern. Symp. on Fatigue Thresholds, Stockholm, (1981), Vol. 2, No. 22.
- [41] Suresh, S., Zamiski, G.F. and Ritchie, R.O., Met. Trans., A12, (1981).
- [42] Toplosky, J. and Ritchie, K.O., Scripta Metallurgica, 15, (1981).
- [43] Stewart, A.T., Eng. Frac. Mech., 13, (1980), 463.
- [44] Liaw, P.K., Hudak, S.J. and Donald, J.K., Proc. 14th Nat. Symp. Frac. Mech., U.C.L.A., ASTM, (1981).
- [45] Suresh, S., Parks, D.M. and Ritchie, R.O., A Paper Presented at Intern. Symp. on Fatigue Thresholds, Stockholm, (1981).
- [46] Walker, N. and Beevers, C.J., Fatigue Engng, Mater. Struct., 1, (1979), 135.
- [47] Blom, A.F., Aeronautical Material (special edition), 2(1982), No. 1, 65.
- [48] Huadk Jr., S.J., Trans. ASME, J. Eng. Met. Tech., 103, (1981), 27.

Finite Element Models Based on a Generalized Hamilton's Principle
for Pfluger's Rod and Its Related Plate*

Chang Kung-hsing and Li Sung-nien

(Beijing Institute of Aeronautics and Astronautics)

ABSTRACT

A generalized Hamilton's principle for analysis of Pfluger's rod and its relative plate is provided in engineering form by a quite simple approach, so that the problem of a nonconservative system is transformed into that of a generalized conservative system. According to this variational principle, an attempt to undertake the discrete tests of finite elements has been made and the features of the finite element model are discussed in brief. A set of symmetric matrices for an element model are given in explicit form. After it is confirmed that instability of Pfluger's rod is caused by divergence, not by flutter, it is pointed out that the critical load can be determined by applying the conventional iterative technique for Rayleigh quotient. Some numerical examples have verified this model.

Finally, as an interesting extension, a finite strip model for analysis of simply supported rectangular plate subjected to follower forces has been derived by using the matrices mentioned above and tested preliminarily.

* Received in April, 1982

I. INTRODUCTION

As is well known, there may exist in non-conservative forces so-called follower forces of the non-conservative component. The work done by these forces under non-infinitesimal displacements is not determined by the initial and final states but depends on the path taken. Hence, the problem of stability for structures under the action of follower forces, such as the Pfluger's rod, cannot be solved by obtaining an approximate solution in the form of an expansion starting out from the usual Hamilton's principle. This has been an established point of discussion for a long time. Therefore, if one still wants to handle these non-conservative problems by means of a variational principle, one is left with two choices. One is to adopt a variational principle that simultaneously takes into account the adjoint system [1]. In this case, the scale of the problem to be solved is enlarged because of the introduction of the variables of the adjoint system. The other is to use an incomplete variational principle (or variational statement) in the expansion of an approximate solution [2]. Although the latter method is a more direct approach, its lack of symmetry makes numerical calculations more elaborate.

Is it possible to establish a general variational function from a generalized Hamiltonian principle without introducing the adjoint system and yet retaining symmetry? This possibility exists for problems with finitude. In Reference [3], a general discussion has been given of this method. However, its generality is only in form. In this paper, the general variational function has been cast into a practical engineering form by a rather simple approach for Pfluger's rod and a related problem. In essence, this is equivalent to what is given in Reference [3]. Based on this variational principle, we have undertaken a first attempt at finite element discretization tests, discussed their characteristics, and provided an element model in explicit form whose matrices are all symmetrical. Computed example demonstrates that this theory also shows effectiveness in the numerical aspect.

For a simply supported rectangular plate subjected to tangentially distributed follower forces, one can use the related matrices of the Pfluger rod element model to obtain the corresponding matrices of the finite strip model for the plate.

II. GENERALIZED HAMILTONIAN PRINCIPLE AND GENERALIZED LAW OF CONSERVATION OF ENERGY

It is easy to write down the differential equation of motion and boundary condition for Pfluger's rod as follows:

D.E.:

$$\ddot{w}(x, t) + \frac{\alpha}{\mu} w_{xxx}(x, t) + \frac{g}{\mu} (L - x) w_{xx}(x, t) = 0 \quad (1)$$

B.C.:

$$w(0, t) = w(L, t) = w_{xx}(0, t) = w_{xx}(L, t) = 0 \quad (2)$$

In the above equations, $w(x, t)$ denotes deflection, α is stiffness to bending, g is the follower force of the distribution in the direction opposite to the positive x -direction, μ is the mass per unit length of the rod, and L is the length of the rod; (\cdot) denotes partial derivative with respect to time, and $(\cdot)_x$ denotes partial derivative with respect to position x .

To answer the question of whether or not there exists general variational functions corresponding to Equations (1) and (2), we can use the simple method of examining the integral given below^[4].

$$\int_{t_1}^{t_2} \int_0^L \left\{ \ddot{w} + \frac{\alpha}{\mu} w_{xxx} + \frac{g}{\mu} (L - x) w_{xx} \right\} \delta w dx dt = 0 \quad (3)$$

If it is possible to take δ in Equation (3) out of the two integrals, then it means that the general variational function has been found. Otherwise, it does not exist. Partial integration of Equation (3) gives

$$\begin{aligned} & -\delta \int_{t_1}^{t_2} \int_0^L \frac{1}{2} \left\{ (\dot{w})^2 - \left[\frac{\alpha}{\mu} (w_{xx})^2 - \frac{g}{\mu} (L - x) (w_x)^2 \right] \right\} dx dt \\ & - \int_{t_1}^{t_2} \left\{ \int_0^L \frac{-g w_x}{\mu} \delta w dx \right\} dt + \int_0^L \dot{w} \delta w dx \Big|_{t_1}^{t_2} \\ & + \int_{t_1}^{t_2} \left\{ \left[\frac{\alpha}{\mu} w_{xxx} + \frac{g}{\mu} (L - x) w_{xx} \right] \delta w - \frac{\alpha}{\mu} w_{xx} \delta w_x \right\} \Big|_0^L dt = 0 \end{aligned} \quad (4)$$

In Equation (4), from the conditions on the time limits of Hamilton's principle, the third term vanishes. The fourth term also vanishes because of Equation (2) and the fact that $\delta\omega$ is an allowed function. Therefore, Equation (4) can be rewritten as

$$\delta H = - \int_{t_1}^{t_2} \int_0^L \frac{-g\omega_x}{\mu} \delta\omega dx dt \quad (5)$$

where

$$H = \int_{t_1}^{t_2} \int_0^L \frac{1}{2} \left\{ (\dot{\omega})^2 - \left[\frac{a}{\mu} (\omega_{xx})^2 - \frac{g}{\mu} (L-x) (\omega_x)^2 \right] \right\} dx dt$$

Obviously, H is the general Hamiltonian of the system when g is a director force rather than a follower force. For the Pfluger rod, as g is a follower force, $\delta H \approx 0$, and the right hand side of Equation (5) is the time-space integral of the virtual work done by the non-conservative component of force, $-g\omega_x$, acting through the virtual displacement $\delta\omega$. It can thus be seen that the general variational function cannot be obtained for the system from ordinary energy considerations. Only something in the form of a variational statement, as exemplified by Equation (5), can be derived. However, it can readily be seen from the fact that the right hand side of Equation (5) is hyperbolic in ω_x and $\delta\omega$ and not an ordinary second-order expression, that the expansion of the approximate solution will always lead to the appearance of asymmetrical matrices.

Derivation of Equation (5) shows us that if we can somehow take the term in Equation (1) containing ω_{xx} out of the process of partial integration, then it will be possible to obtain a general variational function. In fact, substituting $\delta\omega$ with $\delta\omega_{xx}$ in Equation (3), we obtain

$$\int_{t_1}^{t_2} \int_0^L \left\{ \ddot{\omega} + \frac{a}{\mu} \omega_{xxxx} + \frac{g}{\mu} (L-x) \omega_{xx} \right\} \delta\omega_{xx} dx dt = 0 \quad (6)$$

which becomes, after partial integration,

$$\begin{aligned} \int_{t_1}^{t_2} \int_0^L \left\{ -\dot{\omega} \delta \dot{\omega}_{xx} - \frac{a}{\mu} \omega_{xxx} \delta \omega_{xx} + \frac{g}{\mu} (L-x) \omega_{xx} \delta \omega_{xx} \right\} dx dt \\ + \int_0^L \dot{\omega} \delta \omega_{xx} dx \Big|_{t_1}^{t_2} + \int_{t_1}^{t_2} \left(\frac{a}{\mu} \omega_{xxx} \delta \omega_{xx} \right) \Big|_0^L dt = 0 \end{aligned}$$

$$\begin{aligned} & \delta \int_{t_1}^{t_2} \int_0^L \frac{1}{2} \left\{ (\dot{w}_x)^2 - \frac{\alpha}{\mu} (w_{xx})^2 + \frac{g}{\mu} (L-x)(w_{xx})^2 \right\} dx dt \\ & - \int_{t_1}^{t_2} \dot{w} \delta \dot{w}_x \Big|_0^L dt + \int_0^L \dot{w} \delta w_{xx} dx \Big|_{t_1}^{t_2} + \int_{t_1}^{t_2} \left(\frac{\alpha}{\mu} w_{xx} \delta w_{xx} \right) \Big|_0^L dt = 0 \end{aligned} \quad (7)$$

Following the same reasoning as above, we know that the last three terms of Equation (7) should vanish because of the conditions on the time limits and the boundary condition given in Equation (2). Furthermore, for the sake of convenience, we multiply both sides of Equation (7) by 2, and obtain the generalized Hamiltonian principle:

$$\delta H^* = 0 \quad (8)$$

The expression for the generalized Hamiltonian variational function is

$$H^* = \int_{t_1}^{t_2} \int_0^L \left\{ (\dot{w}_x)^2 - \frac{\alpha}{\mu} (w_{xx})^2 + \frac{g}{\mu} (L-x)(w_{xx})^2 \right\} dx dt \quad (9)$$

Thus we have established the variational principle corresponding to the given differential Equation (1) and its boundary condition (2). The approximate solution can be expanded on the basis of Equations (8) and (9); particularly, the finite element approximate solution. Compared with an expansion based on the variational statement (5), that based on the generalized Hamilton's principle makes the numerical computation easier because the symmetry property is retained in the latter.

By obtaining the generalized Hamiltonian variational function and the generalized Hamilton's principle we have in effect transformed the problem of the non-conservative system into that of a generalized conservative system. Here the "energy" cannot possess any physical meaning but is only a mathematical analog. In fact, Equation (3) is apparently an expression of the principle of virtual work. On the other hand, in Equation (6), the force is multiplied by a term that is not its corresponding virtual displacement, and the product is not virtual work in the physical sense. This type of mathematical virtual work or energy can be termed generalized virtual work or energy. Compare this with the canonical problem of

conservative systems. In the latter, the general Hamiltonian variational function is the time-integral of the Lagrangian operator which is the difference between the kinetic energy and the potential energy of the system, and the total energy of the system (sum of the kinetic and potential energy) is conserved (i.e., its rate of change with time is zero). Similarly, from the generalized Hamiltonian variational function, Equation (9), we can write (twice) the generalized total energy of the system as follows:

$$M = \int_0^L \left\{ (\dot{w}_x)^2 + \frac{\alpha}{\mu} (w_{xxx})^2 - \frac{g}{\mu} (L-x) (w_{xx})^2 \right\} dx \quad (10)$$

Differentiate Equation (10) with respect with time to obtain

$$\begin{aligned} \dot{M} = & -2 \int_0^L \left\{ \dot{w} + \frac{\alpha}{\mu} w_{xxx} + \frac{g}{\mu} (L-x) w_{xx} \right\} \dot{w}_{xx} dx \\ & + 2 \left(\dot{w} \dot{w}_x + \frac{\alpha}{\mu} w_{xxx} \dot{w}_{xx} \right) \Big|_0^L \end{aligned} \quad (11)$$

From Equations (1) and (2), $\dot{M}=0$, i.e., with respect to the generalized total energy M , the system is constant, steady and conservative. Therefore, we may say that the original problem of the non-conservative system has been transformed into that of a generalized conservative system.

Let

$$w(x, t) = e^{i\omega t} W(x) \quad (12)$$

Substitute this into Equations (8) and (9), and making use of the conditions on the time limits, we obtain the following boundary value variational expression:

$$\delta h = 0 \quad (13)$$

where

$$h = \int_0^L \left[\omega^2 (W_x)^2 - \frac{\alpha}{\mu} (W_{xxx})^2 + \frac{g}{\mu} (L-x) (W_{xx})^2 \right] dx \quad (14)$$

Equations (13) and (14) are the starting points for establishing the finite element model. Similarly, the boundary condition (2) is changed to

$$W(0)=W(L)=W_{xx}(0)=W_{xx}(L)=0 \quad (15)$$

The differential Equation (1) will take the form

$$-\omega^2 W + \frac{\alpha}{\mu} W_{xxxx} + \frac{g}{\mu} (L-x) W_{xx} = 0 \quad (16)$$

Based on the generalized Hamilton's principle, we may let $\omega=0$. and determine the critical load by applying the conventional iterative technique for Rayleigh quotient. In order to illustrate this, we will briefly discuss the form of instability of Pfluger's rod. Consider the following general function

$$F(\omega^2, g, W(x)) = \int_0^L \left(-\omega^2 W + \frac{\alpha}{\mu} W_{xxxx} + \frac{g}{\mu} (L-x) W_{xx} \right) W_{xx} dx = 0 \quad (17)$$

From

$$dF = \frac{\partial F}{\partial \omega^2} d\omega^2 + \frac{\partial F}{\partial g} dg + \frac{\partial F}{\partial W} dW = 0$$

where

$$\begin{aligned} \frac{\partial F}{\partial W} dW = \int_0^L \left\{ \left(-\omega^2 W + \frac{\alpha}{\mu} W_{xxxx} + \frac{g}{\mu} (L-x) W_{xx} \right) \delta W_{xx} \right. \\ \left. + W_{xx} \delta \left(-\omega^2 W + \frac{\alpha}{\mu} W_{xxxx} + \frac{g}{\mu} (L-x) W_{xx} \right) \right\} dx \end{aligned} \quad (18)$$

it can be checked by partial integration that the two terms on the right hand side of Equation (18) are equal. Furthermore, from Equation (16) we know that $\partial F / \partial W \cdot dW = 0$. Therefore, the slope of the eigenvalue curve $\omega^2 = \omega^2(g)$:

$$\frac{d\omega^2}{dg} = - \frac{\partial F / \partial g}{\partial F / \partial \omega^2} = - \frac{\int_0^L \frac{(L-x)}{\mu} (W_{xx})^2 dx}{\int_0^L -W W_{xx} dx}$$

From Equation (15), we know that the denominator of the above expression is

$$\begin{aligned} \text{Therefore,} \quad & \int_0^L (W_{,x})^2 dx \\ & \frac{d\omega^2}{dg} < 0 \end{aligned} \quad (19)$$

Equation (19) shows that the slope of the eigenvalue curve of Pfluger's rod is always negative. Therefore, instability will occur in the form of divergence rather than flutter. Hence, if one is only concerned with the determination of the critical load, one may let $\omega = 0$, and the problem becomes one of stability of static forces. It will not be hard to see that the problem of determining the critical load g_{crit} for the function $W(x)$ that satisfies the boundary condition (15) is equivalent to that of determining the minimum value of the following Rayleigh quotient.

$$G \equiv \frac{N(W)}{D(W)} = \frac{\int_0^L \frac{\alpha}{\mu} (W_{,x})^2 dx}{\int_0^L \frac{(L-x)}{\mu} (W_{,x})^2 dx} \quad (20)$$

Obviously, the numerator and denominator of the above expression are positive definite integrals. The value of G determined from the stationary-value condition on Equation (20) is nothing but Equation (13) for $\omega = 0$.

III. FINITE ELEMENT MODEL FOR PFLUGER ROD

Compared with the finite element discretization based on a variational statement, that based on the generalized Hamilton's variational principle formulated above has the following characteristics besides possessing symmetry. First, the finite element discretization model has to satisfy all boundary conditions and not just the geometric boundary conditions of the original problem. Secondly, the requirement on the order of continuity among the elements is increased. The highest order derivative in the general variational function is of the third order while those for the method using

variational statements and for the usual problem of conservative systems are only of the second order.

With respect to the second characteristic, it would seem that the so-called "over-conservative connected elements" would be useful in problems of stability of non-conservative systems. However, available over-conservative connected elements are not adequate for forming complete element models because up until now there is as yet no element used in structural analysis that has been derived from a general function containing third order derivatives. Moreover, the existence of distributed follower forces results in complicated generalized geometric stiffness matrix.

For the sake of convenience, we express Equation (14) in dimensionless quantities. Let

$$\begin{aligned} Q^2 &= \frac{\mu \omega^2 L^4}{\alpha} \\ q &= \frac{gL^3}{\alpha} \\ \zeta &= \frac{x}{L} \end{aligned} \quad (21)$$

Then, Equations (14) and (15) can be rewritten as

$$\bar{h} = \int_0^1 \{Q^2(W')^2 - (W'')^2 + q(1-\zeta)(W'')^2\} d\zeta \quad (22)$$

$$W(0) = W(1) = W''(0) = W''(1) = 0 \quad (23)$$

Let the rod be divided into n elements of equal length. The elements and nodes are numbered from 1 to n and from 1 to $(n+1)$, respectively, along the positive x -direction. Let β denote the local coordinate of each element, with values lying between 0 and 1. After carrying out the finite element discretization, the general function \bar{h} will be in the form of an algebraic expression. After completing the variational operations, we obtain the algebraic eigenvalue problem to be solved:

$$\{K_i - q(K_i - K_j)\}\{D\} = Q^2\{K_i\}\{D\} \quad (24)$$

where

$\{D\}$ — is the effective degree of freedom

$[K] = \sum_i [K_i]$ — is the generalized mass matrix

$[K_s] = n \sum_i (n - i + 1) [K_i]$ — is the generalized geometric stiffness matrix (corresponding to the conservative force)

$[K_n] = n \sum_i [K_i]$ — is the generalized geometric stiffness matrix (corresponding to the non-conservative force)

$[K_s] = n^2 \sum_i [K_i]$ — is the generalized stiffness matrix

$[K_i]$, $j = 1, 2, 3, 4$, — denotes the matrix related with the i th element.

/3

This matrix will have different forms of expression depending on the different design elements of the shape function. However, the form will not vary with the element number i . Therefore, one may omit the superscript i . The set of matrices listed below are the shape functions corresponding to fifth-order complete polynomials. The nodal variable of the i th element is

$$[D'] \equiv [(W, W_x, W_{xx})_i, (W, W_x, W_{xx})_{i+1}]$$

Even though if one is only concerned with the critical load, k_j is of no use, we list its values below for the sake of completeness and for later application in the problem of the rectangular plate.

$$\begin{aligned}
K_1' &= \frac{1}{1260} \begin{pmatrix} 1800 & & & & & \\ & 270 & 288 & & & \text{symmetrical} \\ & 15 & 21 & 2 & & \\ -1800 & -270 & -15 & 1800 & & \\ & 270 & -18 & -6 & -270 & 288 \\ -15 & 6 & 1 & 15 & -21 & 2 \end{pmatrix} \\
K_2' &= \frac{1}{210} \begin{pmatrix} 3600 & & & & & \\ 1800 & 1152 & & & & \\ 90 & 66 & 18 & & & \\ -3600 & -1800 & -90 & 3600 & & \\ 1800 & 648 & 24 & -1800 & 1152 & \\ -90 & -24 & 3 & 90 & -66 & 18 \end{pmatrix} \\
K_3' &= \frac{1}{140} \begin{pmatrix} 1200 & & & & & \\ 480 & 264 & & & & \\ 40 & 24 & 3 & & & \\ -1200 & -480 & -40 & 1200 & & \\ 720 & 216 & 16 & -720 & 504 & \\ -20 & 0 & 1 & 20 & -20 & 9 \end{pmatrix} \\
K_4' &= \frac{1}{4} \begin{pmatrix} 2880 & & & & & \\ 1440 & 768 & & & & \\ 240 & 144 & 36 & & & \\ -2880 & -1440 & -240 & 2880 & & \\ 1440 & 672 & 96 & -1440 & 768 & \\ -240 & -96 & -12 & 240 & -144 & 36 \end{pmatrix}
\end{aligned}$$

IV. FINITE STRIP MODEL FOR SIMPLY SUPPORTED RECTANGULAR PLATE

Let the boundaries of the simply supported rectangular plate be at $x=0, a$; and $y=0, b$. The plate is under the action of tangentially distributed follower forces along the negative x -direction. Its differential equation and boundary conditions are:

$$\text{D.E.:} \quad \ddot{w} + \frac{D}{\mu} \nabla^4 w + \frac{g}{\mu} (a-x) w_{xx} = 0 \quad (25)$$

$$\begin{aligned} \text{B.C.:} \quad & x=0, a; \quad w=0 \text{ 与 } w_{xx} + \nu w_{yy} = 0 \\ & y=0, b; \quad w=0 \text{ 与 } w_{xx} + \nu w_{yy} = 0 \end{aligned} \quad (26)$$

Obviously, there exists no general Hamiltonian variational function in the ordinary sense for this problem because the external force does not do actual work. Following the method used for Pfluger's rod, we multiply the right hand side of the differential Equation (25) by $\delta\omega_{xx}$ and perform integration over space and time. Noting that not only is the bending moment zero but also $\omega_{xx}=0$, and $\omega_{yy}=0$ on the perimeter of the simply supported plate, we can derive the following generalized Hamiltonian variational function and variational principle:

$$\delta H^* = 0$$

$$H^* = \int_{t_1}^{t_2} \int_{x=0}^a \int_{y=0}^b \left\{ (\dot{w})^2 - \frac{D}{\mu} [(w_{xx})^2 + 2(w_{xy})^2 + (w_{yy})^2] \right. \quad (27)$$

$$\left. + \frac{g}{\mu} (a-x)(w_x)^2 \right\} dx dy dt \quad (28)$$

Similarly, we can also demonstrate the conservative property of its generalized total energy, its instability being in the form of divergence, the existence of a generalized Rayleigh quotient, etc. These will be omitted here.

Let

$$w(x, y, t) = e^{i\omega t} W(x, y) \quad (29)$$

from Equation (27), Equation (28) can be rewritten as

$$\delta h = 0$$

$$h = \int_0^a \int_0^b \left\{ \omega^2 (W_x)^2 - \frac{D}{\mu} [(W_{xx})^2 + 2(W_{xy})^2 + (W_{yy})^2] \right. \quad (30)$$

$$\left. + \frac{g}{\mu} (a-x)(W_x)^2 \right\} dx dy \quad (31)$$

The boundary condition changes to the following:

On the perimeter,

$$W = W_x = W_y = 0 \quad (32)$$

Let $x = a\xi$, $y = b\eta$, λ be the ratio of the length of the plate to its width such that $b = \lambda a$, and

$$\begin{aligned}\Omega^2 &= \mu \omega^2 a^4 / D \\ q &= g a^2 / D\end{aligned}\quad (33)$$

Then Equations (31) and (32) are changed correspondingly into their dimensionless forms:

$$\begin{aligned}\bar{h} &= \int_0^1 \int_0^1 \left\{ \Omega^2 (W_{,\zeta})^2 + \left[(W_{,\xi\xi})^2 + \frac{2}{\lambda^2} (W_{,\xi\zeta})^2 + \frac{1}{\lambda^4} (W_{,\zeta\zeta})^2 \right] \right. \\ &\quad \left. + q(1-\zeta)(W_{,\xi\xi})^2 \right\} \lambda d\zeta d\xi\end{aligned}\quad (34)$$

On the perimeter, where $\zeta = 0.1$ and $\xi = 0.1$, we have

$$W = W_{,\xi} = W_{,\xi\xi} = 0 \quad (35)$$

The finite element model for the rectangular plate can be expanded on the basis of Equations (34) and (35). Here, we adopt the convenient finite strip model, and make use of the matrices that are already available for the element model of Pfluger's rod.

Let

$$W(x, y) = \sum_{m=1,3,5,\dots} F_m(\zeta) \sin m\pi\xi \quad (36)$$

Substitute Equation (36) into Equation (34), and complete integration with respect to ξ . Note the orthogonality of the trigonometric functions. It follows that for different values of m , there is no coupling among the corresponding $F_m(\zeta)$'s. We obtain

$$\begin{aligned}\bar{h} &= \frac{\lambda}{2} \sum_m \int_{\zeta=0}^1 \left\{ \Omega^2 (F'_m)^2 - \left[(F''_m)^2 + \frac{2}{\lambda^2} (F'_m)^2 (m\pi)^2 \right. \right. \\ &\quad \left. \left. + \frac{1}{\lambda^4} (m\pi)^4 (F'_m)^2 \right] + q(1-\zeta)(F''_m)^2 \right\} d\zeta\end{aligned}\quad (37)$$

For the discretization along the ξ -direction, we adopt a fifth order polynomial as in the case of Pfluger's rod, and divide the plate into n equal elements. Comparing Equations (37) and (22), we see that for any given odd value of m , the F_m in Equation (37) corresponds to the W in Equation (22), except that the derivative of F_m with respect to ζ is denoted by " $'$ ", and the expression corresponding to $(W_{,\zeta\zeta})^2$ is made up of three terms $\left[(F''_m)^2 + \frac{2}{\lambda^2} (F'_m)^2 (m\pi)^2 + \frac{1}{\lambda^4} (m\pi)^4 (F'_m)^2 \right]$. Hence, corresponding to each value of m , there are the following structural matrices:

$$[K_{1m}] \equiv [K_1] = \sum_i [K_i^1]$$

- is the generalized mass matrix

$$[K_{2m}] \equiv [K_2] = n \sum_i (n+1-i) [K_i^2]$$

- is the generalized geometric stiffness matrix (corresponding to the conservative force)

$$[K_{3m}] \equiv [K_3] = n \sum_i [K_i^3]$$

- is the generalized geometric stiffness matrix (corresponding to the non-conservative force)

$$\begin{aligned} [K_{4m}] &= [K_4] + 2 \left(\frac{m\pi}{\lambda} \right)^2 [K_2] + \left(\frac{m\pi}{\lambda} \right)^4 [K_1] \\ &= n^4 \sum_i [K_i^4] + 2 \left(\frac{m\pi}{\lambda} \right)^2 n \sum_i (n+1-i) [K_i^2] + \left(\frac{m\pi}{\lambda} \right)^4 \sum_i [K_i^1] \end{aligned} \quad (38)$$

In the above $K_1^1, K_2^1, K_3^1, K_4^1$ are the same as those for Pfluger's rod with the same notations.

Finally, we present some simple numerical examples. For Pfluger's rod, Reference [5], gives $q_{crit} = 18.96$. From our finitel element model, $q_{crit} = 19.188$ for $n=1$ and $q_{crit} = 18.97$ for $n=2$. For the simply supported plate, taking $\lambda=n=m=1$, we find, from Equation (38) $q_{crit} = 68.16$. The approximate solution given in Reference [2] is 69.1.

V. CONCLUSION

We have used simple approach to discuss Pfluger's rod in detail, particularly concerning the variational principle that is used to transform this non-conservative problem into one of a generalized conservative system. On the basis of this variational principle, we have carried out finite element discretization tests and presented the element matrices that are all symmetrical and convenient to use. We have also pointed out the procedure by which the finite strip

model for the related simply supported rectangular plate may be obtained using these matrices. It should be pointed out, however, that it may not be possible to transform a more general non-conservative problem in the same manner, and that this more general system may have some new characteristics that need to be dealt with. All these problems require further study.

REFERENCES

- [1] S.N. Prasad and G. Herrmann: "The usefulness of adjoint systems in solving nonconservative stability problems of elastic continua", Int. J. Solids Struct., 5, 727-735, 1969.
- [2] H. Leipholz: "Direct variational methods and eigenvalue problems in engineering", 1977.
- [3] H. Leipholz: "Variational principles for nonconservative problems, a foundation for a finite element approach" CMAME 17/18, 609-617, 1979.
- [4] K.H. Huebner: "The finite element method for engineers", 1975.
- [5] A. Pfluger: "Stability problems of elastostatics", 1950.

BUZZ IN AXISYMMETRIC SUPERSONIC INLET AND ITS CONTROL

Ho Chung-wei and Chang Shih-ying

(Nanching Aeronautical Institute)

ABSTRACT

An investigation on buzz in an axisymmetric external compression inlet and its control are presented. A zone of boundary layer bleed on the cone surface at throat has been designed (Fig.1). A block diagram of a dynamic pressure measuring system employed is shown in Fig.2. The static pressure fluctuation on the cone surface at throat has been picked up by Kulite transducer. The results of the experimental investigation can be summarized as follows,

1. At Mach number $M_\infty=1.97$ and angle of attack $\alpha=0^\circ$, there is only a little static pressure fluctuation in the stable supercritical regime or subcritical regime with a bow shock attached ahead the cowl lip. When the bow shock is away from the cowl lip, the feature of instability appears. And as buzz occurs in the inlet, the pressure fluctuates sharply (Fig.3). The characteristic frequency of pressure fluctuation is 43.75Hz (Fig.4). Its Δp_{rms} is about several times that of the supercritical regime (Fig.4).

2. At $M_\infty=1.97$, and $\alpha=12^\circ$, as buzz occurs in the inlet, the bow shock on the lee side of the cone vibrates sharply with a large amplitude (Fig.6), and the pressure fluctuation is ~~more~~ sharper than that on the windward side (Fig.7), and its main frequency is 18.75Hz (Fig.8). The Δp_{rms} is about double that on the windward side. The bow shock on the windward side vibrates with a small amplitude (Fig.6), and the main frequency is 20Hz.

3. By opening bleeder door with mass flow ratio $W_b/W_\infty=0.0061$, the inlet buzz disappears at once. The bow shock becomes stable (Fig.10), and the amplitude of the pressure fluctuation and their Δp_{rms} become smaller (Fig. 10 and Fig.11). The main frequency of pressure fluctuation, for example, on the lee side disappears (Fig.12).

NOTATIONS

M	
M_∞	Mach number of on-coming stream
M_s	Mach number of stream on surface of cone
$P_{T\infty}$	Total pressure of on-coming stream
W	Inlet mass flow of capture
A_c	Inlet area of capture
A_i	Area of inlet
ϕ	$=A_\infty/A_i$, flow parameter
x	Distance on the cone from the point of measurement to the apex
PA	Density of power spectrum
α	Angle of attack
P_s	Static pressure of stream on surface of cone
$\Delta p_{r,m,s}$	Root-mean-square value of fluctuating pressure
W_{bl}	Amount removed by boundary layer
A_∞	Free stream area
R_c	Radius of capture
x	Distance from point of measurement to cowl lip
ω	Frequency
Subscript "sup" denotes stable supercritical condition	

I. FOREWORD

Supersonic air intake buzz has always been a topic of great interest in other countries [1]-[4]. Research reports have been presented on the characteristics of inlet buzz, development of buzz, and inlet and throat flow characteristics under inlet buzz condition when the angle of attack is 0° . However, aircraft flight tests have shown that inlet buzz usually occurs under flight conditions where the angle of attack is relatively large. Therefore, the study of this problem is of practical significance.

II. EXPERIMENTAL MODEL

The model is a double-cone axisymmetric supersonic inlet constructed on the scale of 1:9.94 (Figure 1). The angles of the cones are, respectively, 35° and 50° . The angles of the inner and outer lips of the cowl are, respectively, 10° and 14° . The radius of capture R_c of the inlet is 47.4 mm. The geometric throat of the inlet is located at a position where $x/R_c = 0.232$. The conic body of the model is hollow. The boundary layer that has been removed from the surface of the cone is sucked into the hollow inside of the cone to flow past the branch rod and flow meter, and then returned to the low-pressure cabin of the wind tunnel. A series of static pressure holes have been designed on the upper and lower surfaces of the conic body. At the position where $x/R_c = 8.842$ is placed a rotating rake with 12 points for measuring total pressure. The position of the rotating rake during tests is monitored by means of a special indicator. The inlet mass flow is controlled through the tail-plug cone.

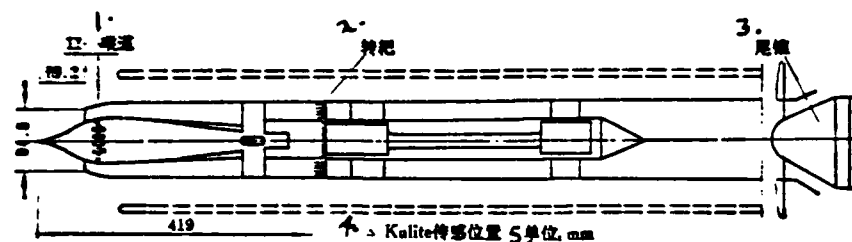


Figure 1. Axisymmetric supersonic inlet model.

Key: 1-Throat; 2- Rotating rake; 3- Tail cone; 4- Position of Kulite transducer; 5- Unit: mm

III. WIND TUNNEL AND MEASURING SYSTEM

The tests were carried out in the supersonic inlet wind tunnel of Nanching Aeronautical Institute. The dimensions of the nozzle are 160 mm x 160 mm, and its maximum angle of downward tilt is 15°. The Reynold number Re of the wind tunnel, that has as its characteristic dimension the inlet radius of capture, is $2 \times 10^6 - 5 \times 10^6$ (for $M_\infty = 1.6-2.63$).

The steady-state measuring system consists of SYD-1 transducer, XJ-100 detector and Model LS-5 digital recorder.

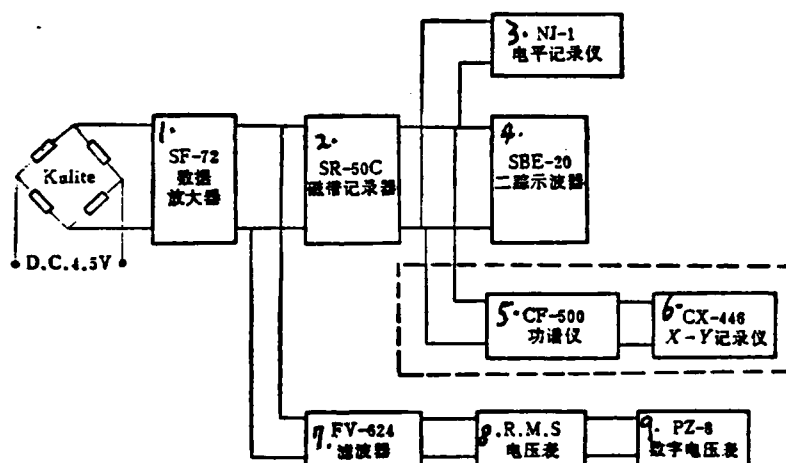


Figure 2. Block diagram of dynamic pressure measuring system.

Key: 1- SF-72 data amplifier; 2- SR-50C magnetic tape recorder; 3- NJ-1 recorder; 4- SBE-20 two-trace oscilloscope; 5- CF-500 power spectrum analyzer; 6- CX-446 x-6 recorder; 7- FV-624 filter; 8- R.M.S. voltmeter; 9- PZ-8 digital voltmeter.

The dynamic pressure measuring system is shown in Figure 2, NO.CQL-030-100 and NO.CQL-070-25 Kulite transducers are used to measure the fluctuating pressure at the geometric throat and on the surface of the cone. The electric signals put out by the transducers pass through the SF-72 amplifier, and are recorded by the SR-50 C magnetic tape recorder. At the same time, these signals are monitored by means of the SBE-20 oscilloscope. Or, the NJ-1 recorder is used to record the time history of the pressure. The signals also pass through the FV-624 filter and R.M.S. voltmeter, and the root-mean-square value of the fluctuating pressure is obtained. To obtain the principal characteristic frequency, use CF-500 to analyze the power spectrum. /41

IV. DESIGN OF BOUNDARY LAYER BLEED ZONE

According to References [2] and [4], upon separation of the boundary layer on the (slanted) cone surface, the inlet flow is hindered, and the unstable flow of the boundary layer gives rise to the inlet buzz. For $M_\infty = 1.97$ and $\alpha = 0^\circ$, we used the procedure given in Reference [6] to compute the development of the boundary layer along the surface of the cone. Our results show that the boundary layer develops very fast on the surface of the cone near the throat, increasing from 0.677 to over 1.088 mm. Furthermore, the Mach number of the surface of the cone near the throat obtained under similar conditions under supercritical conditions reaches above 1.40-1.77, and the boundary layer of the second compression surface becomes disordered [5],[6]. Hence when bow shock appears in front of the lip of the inlet, the intensity of the shock wave is sufficient to cause the boundary layer at that location on the cone surface to separate [7]. To control inlet buzz, we design the boundary layer bleed zone on the surface of the cone near the throat. Five rows of holes, bored vertically into the surface, are arranged alternately along the perimeter. The diameter of the holes is 1.5 times the thickness of the local boundary layer. The total area of the holes is 468 mm^2 , approximately equal to 1/10 of the area of the geometric throat.

V. EXPERIMENTAL RESULTS AND DISCUSSION

1. Characteristics of Static Pressure Fluctuation on the Cone

Surface for 0° Angle of Attack

For $M_\infty=1.97$, $\alpha=0^\circ$, the NO.CQL-030-100 Kulite transducer measures fluctuation of the static pressure on the cone surface at the geometric throat. The static pressure history for various typical mass flow ratios as well as the corresponding series of shock waves under steady supercritical and subcritical conditions are shown in Figure 3. It can be seen from Figure 3 that under steady supercritical and subcritical conditions, the pressure has a flat time history. When the bow shock is farther away from the lip of the inlet ($\phi=0.78$),

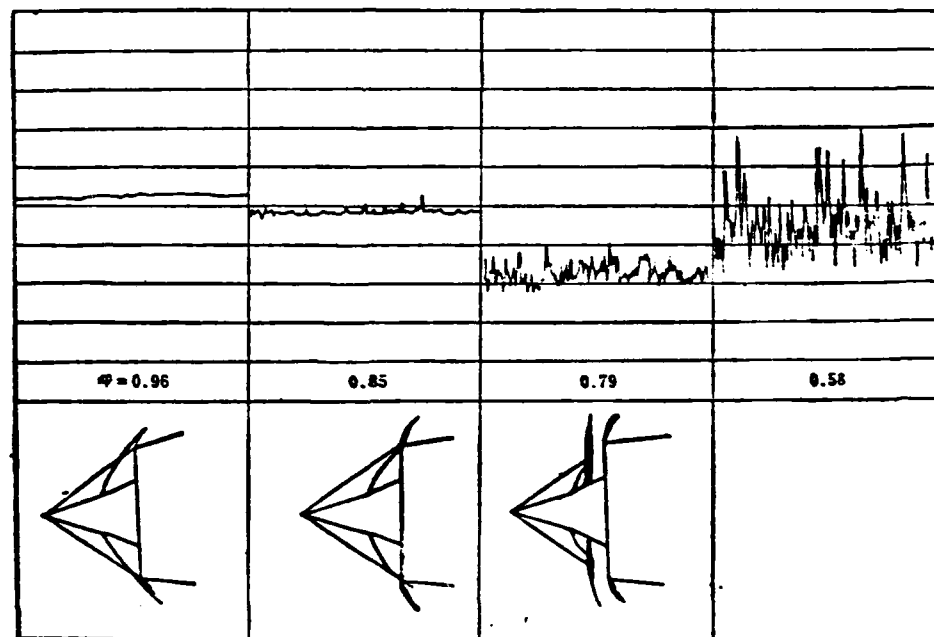


Figure 3. Static pressure history at specific mass flow ratios.

the static pressure undergoes marked fluctuation with time. When buzz occurs in the inlet, the fluctuation becomes very pronounced, with a large amplitude. There is a close correspondence between

the above-mentioned characteristics of static pressure fluctuation and the measured static pressure fluctuation $\Delta p_{r.m.s.}$ for the various mass flow ratios, as shown in Figure 4. ($\phi=0.78$). The value of $\Delta p_{r.m.s.}$ is several times that of the steady supercritical regime when buzz occurs in the inlet.

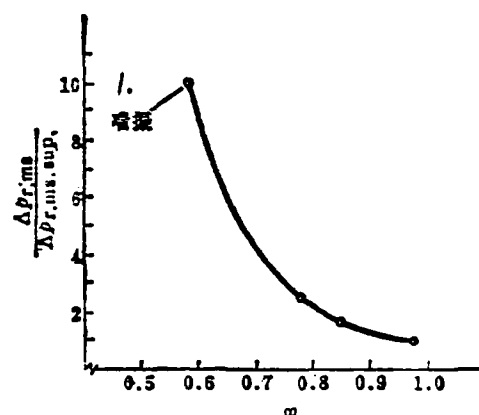
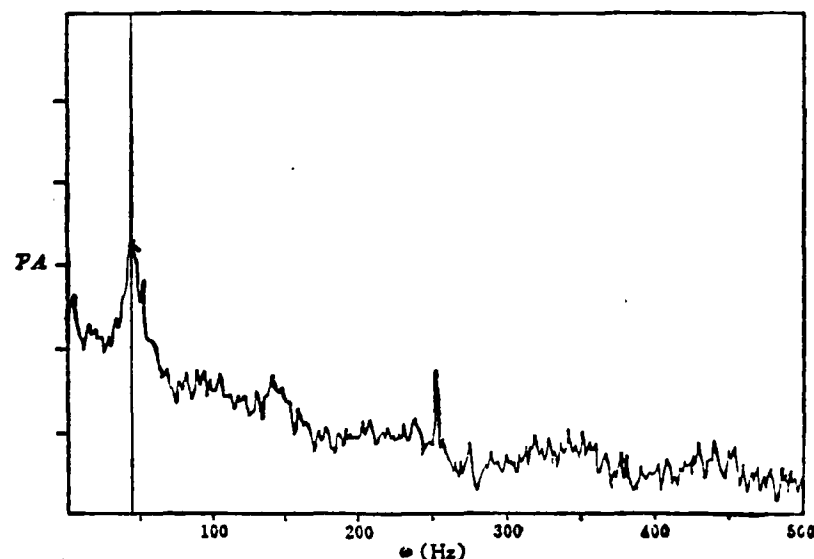


Figure 4. $\Delta p_{r.m.s.}$ of static pressure at specific mass flow ratio

A: 5 500
B: 5V 500Hz



HI-
LO-A 43.75Hz -32.34dB V

Figure 5. Power spectrum of static pressure on the cone surface in intake buzz conditions.

Power spectrum analysis using CF-500 Power Spectrum Analyzer yields for the time history of the pressure under intake buzz condition the power spectrum $PA-\omega$ for the fluctuating pressure under intake buzz condition. /4

It can be seen that the principal frequency of the static pressure fluctuation under intake buzz condition is 43.75 Hz (Figure 5).

2. The Dynamic Characteristics of Inlet Buzz for Larger Angles of Attack

- (1) Characteristics of bow shock fluctuation in front of the inlet lip

Tests on the dynamics of buzz have been performed under the conditions $m_\infty = 1.97$ and $\alpha = 12^\circ$. By slowly moving the tail cone, one can see that the inlet bow shock passes buzz characteristics different from those for 0° angle of attack. Under buzz condition, the bow shock on the lee side of the cone undergoes violent vibrations which are invisible to the naked eye, while the bow shock waves on the windward side are clearly visible (Figure 6). Figure 6 has been obtained by photographing at the speed of 1/50 seconds. Owing to the violent vibrations of the bow shock on the lee side of the cone, its image on the Schlieren photograph is blurred. The bow shock on the windward side, however, yields a very clear image.

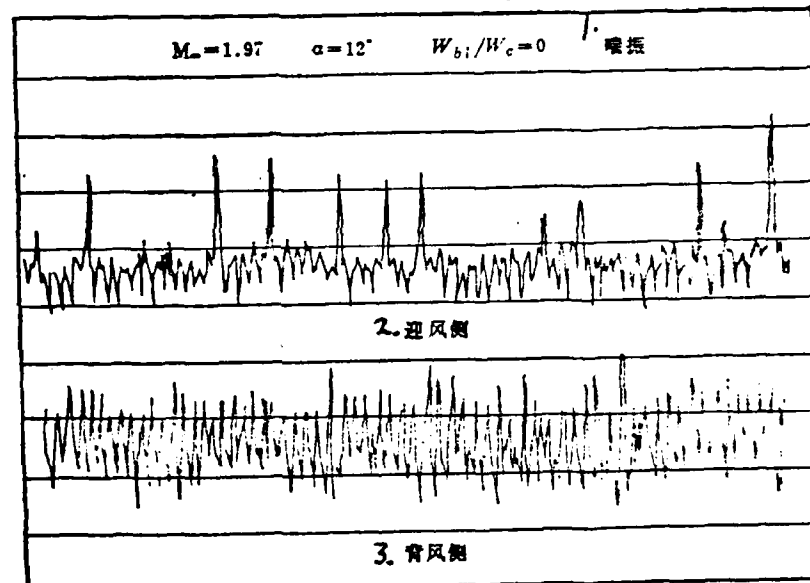
- (2) Characteristics of static pressure fluctuation on the surface of the cone under intake buzz condition.

Figure 7 shows the leeward and windward static pressure time history, measured by means of NO.CAL-075-25 transducer for the cone (at the throat), that corresponds to Figure 6. It is clear that, under intake buzz condition, the leeward static pressure fluctuation is much more severe than that on the windward side. Experimentally measured fluctuating pressure $\Delta p_{r,m,s}$ under the same conditions is twice as large on the lee side as on the windward side.



($M_\infty = 1.97$ $\alpha = 12^\circ$ $\varphi = 0.8847$ $W_{bi}/W_c = 0$)

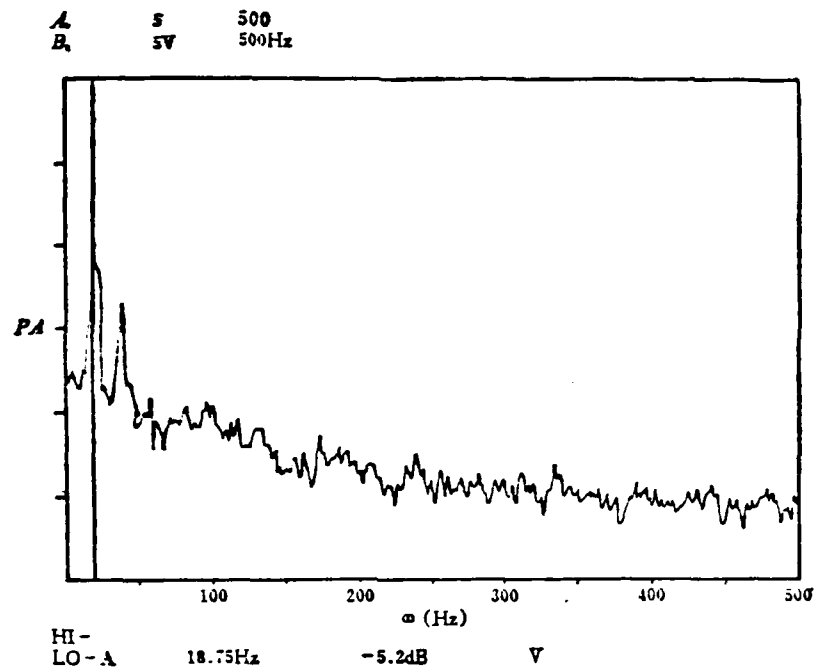
Figure 6. Schlieren photograph of shock wave in intake buzz condition.



($M_\infty = 1.97$ $\alpha = 12^\circ$ $\varphi = 0.8847$ $W_{bi}/W_c = 0$)

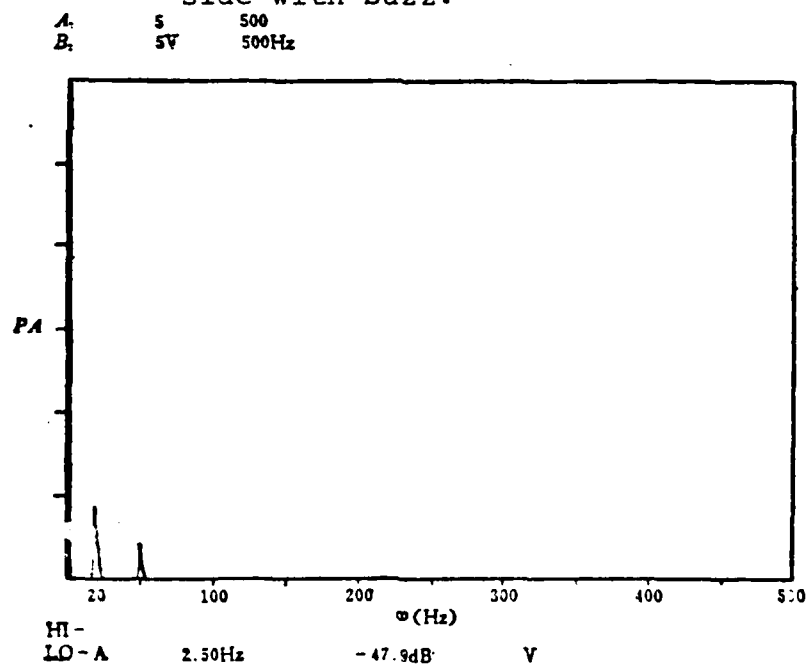
Figure 7. Comparison between pressure histories of the lee side and windward side on the cone surface in intake buzz conditions.

Key: 1- Buzz; 2- Windward side; 3- Lee side



$$(M_\infty = 1.97 \quad \alpha = 12^\circ \quad \frac{W_M}{W_c} = 0 \quad \varphi = 0.8847)$$

Figure 8. Power spectrum of static pressure on lee side with buzz.



$$(M_\infty = 1.97, \quad \alpha = 12^\circ \quad \frac{W_M}{W_c} = 0 \quad \varphi = 0.8847)$$

Figure 9. Power spectrum of static pressure on windward side with buzz.

- (3) Characteristic frequencies of static pressure fluctuation on the surface of the cone under intake buzz condition

Spectral analysis of the pressure history on the leeward and windward sides of the cone by means of the CF-500 power spectrum analyzer yields the power spectra Figures 8 and 9 under intake buzz condition. It can be seen from these that the principal characteristic frequency is 18.75 Hz on the lee side and 20 Hz on the windward side. The two values are very close to each other.

3. Improvement of the Dynamic Characteristics of the Inlet by Elimination of Intake Buzz Through Boundary Layer Bleed

- (1) Characteristics of inlet bow shock

Buzz suppression tests have been carried out under the condition that $M_\infty = 1.97$ and $\alpha = 12^\circ$. When buzz occurs in the inlet, the boundary layer bleeding holes are opened, and both the leeward and windward bow shocks become steady (Figure 10). The picture was taken at a speed of 1/50 second. The large-amplitude fluctuation of the bow shock on the lee side has disappeared.

- (2) Comparison of the static pressure fluctuation characteristics and the characteristic frequencies under intake condition with those after elimination of buzz.

After buzz is eliminated, there are significant changes in the static pressure time history on the lee and windward sides of the cone, and the amplitude of the fluctuation decreases dramatically (Figure 11). Experimental measurements show that the static pressure $\Delta p_{r,m,s}$ on the lee side after buzz is eliminated is only 1/3 that in the presence of buzz. The static pressure $\Delta p_{r,m,s}$ on the windward side after buzz is eliminated is only 1/2 of that in the presence of buzz. With the disappearance of buzz, the sharp fluctuation of the bow shock on the lee side abates, and a steady condition is attained. At this moment, the characteristic frequencies of the static pressure fluctuation shown in Figure 8 all disappear (Figure 12).



$M_\infty = 1.97 \quad \alpha = 12^\circ \quad \varphi = 0.9144 \quad W_{bl}/W_c = 0.0061$

Figure 10. Schlieren photograph of shock waves without buzz.

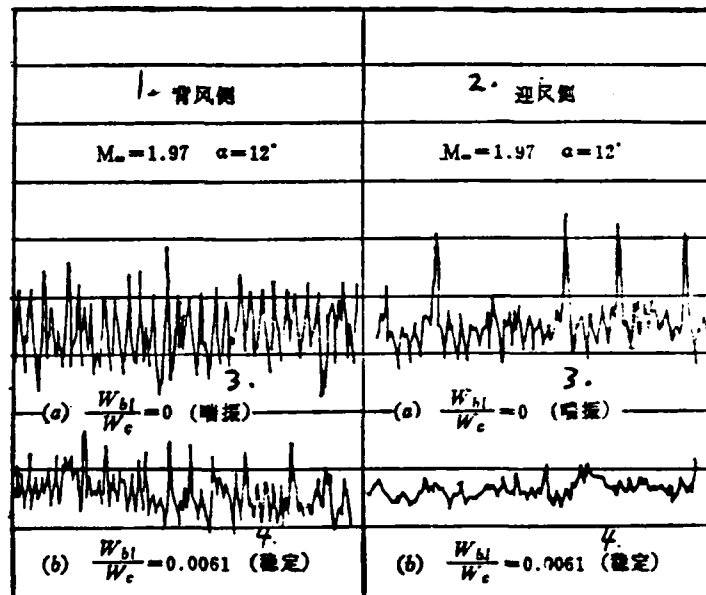


Figure 11. Comparison between the static pressure histories of the lee side and windward side with or without buzz.

Key: 1- Lee side; 2- Windward side; 3- Buzz; 4- Steady state

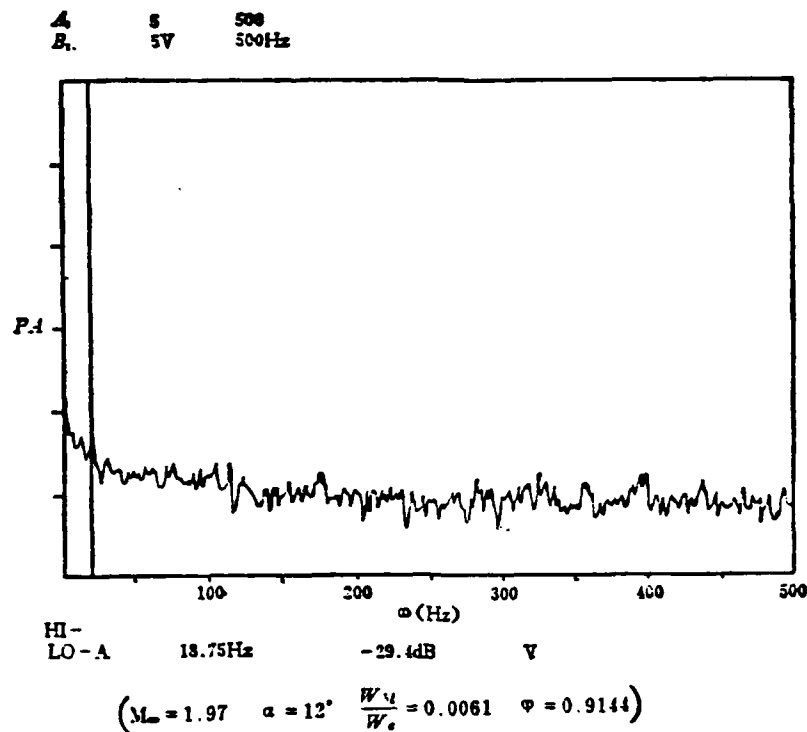


Figure 12. Power spectrum of static pressure on lee side without buzz.

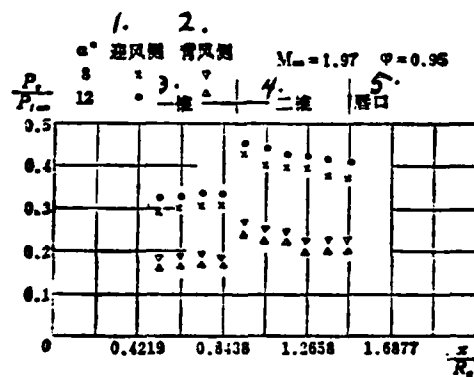


Figure 13. Comparison between the static pressure distributions on the lee side and the windward side.

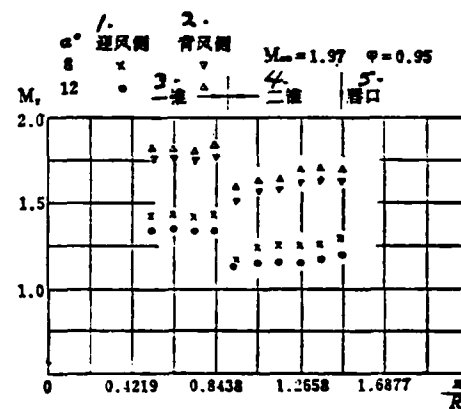


Figure 14. Comparison between the Mach number distributions on the lee side and the windward side.

Key: 1- Windward side; 2- Lee side; 3- First cone; 4- Second cone; 5- Lip

4. Discussion

The fact that the characteristics of inlet buzz for larger angles of attack are different from those for 0° angle of attack is closely related to the asymmetry of the shock waves on the surface of the cone at larger angles of attack. This asymmetry leads to a much higher static pressure on the windward side than on the lee side, as shown in Figure 13. The larger the angle of attack, the greater the difference in static pressure. This causes the boundary layer on the windward side to flow toward the lee side, resulting in an increase in thickness of the boundary layer on the lee side. On the other hand, the asymmetry in the shock waves on the cone surface also leads to a much higher Mach number on the second cone surface on the lee side than on the windward side. It can be seen from Figure 14 that under the condition that $M_\infty=1.97$ and $\alpha=8^\circ$ or 12° , the Mach number of the stream on the cone surface on the lee side in front of the cowl lip is greater than 1.6. When the bow shock waves appear in front of the cowl lip, their intensity is already high enough to cause the thickened boundary layer to separate, or even enough to cause separation of the main stream. On the windward side, however, the Mach number of the stream on the surface of the cone only goes up to about 1.25, and the bow shock may not be strong enough to cause separation of the boundary layer. This difference becomes more pronounced with increasing angle of attack. This explains why when buzz occurs in a symmetrical inlet at a large angle of attack the bow shock on the lee side goes into violent large-amplitude fluctuation. With a high pressure fluctuation $\Delta p_{r,m,s}$, while the bow shock on the lee side only undergoes small-amplitude fluctuation, with low pressure fluctuation $\Delta p_{r,m,s}$.

VI CONCLUSION

(1) Our study on the dynamic characteristics of the static pressure on the cone surface at the geometric throat of a double-cone axially symmetric supersonic inlet for $M_\infty=1.97$ and $\alpha=0^\circ$ reveals that when the inlet goes from the steady supercritical regime into the subcritical regime, and finally reaches buzz condition,

the static pressure time history gradually changes from a steady level trace into one with obvious static pressure fluctuation which becomes very violent, and with large amplitudes, under buzz condition. At this moment, the static pressure fluctuation $\Delta p_{r,m,s}$ may become several times that under supercritical or subcritical conditions. The principal characteristic frequency of the static pressure fluctuation is 43 Hz.

(2) For $M_\infty = 1.97$ and $\alpha = 12^\circ$, our results show that when buzz occurs in the inlet, the bow shock on the lee side of the cone goes into large-amplitude fluctuation first, with a principal characteristic frequency of pressure fluctuation of 18.75 Hz; $\Delta p_{r,m,s}$ of the static pressure fluctuation is about twice that on the windward side. The bow shock on the windward side only undergoes small-amplitude fluctuation, with a principal characteristic frequency of 20 Hz, close to that on the lee side. Once the boundary layer on the cone surface (at the throat) is removed by bleeding, intake buzz disappears, and there is marked decrease in the static pressure fluctuation, with the static pressure fluctuation $\Delta p_{r,m,s}$ on the lee side equal to 1/3, and that on the windward side equal to 1/2 of their corresponding values under buzz condition. Furthermore, as the buzz is eliminated, the violent large-amplitude fluctuation of the bow shock on the lee side disappears, and the principal characteristic frequencies of its static pressure fluctuation all disappear.

(3) Finally, we have made an analysis of the characteristics of buzz in an axisymmetric inlet at a relatively large angle of attack.

REFERENCES

- [1] Ferri, A. and Nucci, L. M. The Origin of Aerodynamic Instability of Supersonic Inlets at Subcritical Conditions NACA RM L50K30, 1951.
 - [2] Dailey, C. L. Supersonic Diffuser Instability Journal of the Aeronautical Sciences vol. 22, No. 11 1955.
 - [3] Nagashima, Obokata and Tsuyoshi Asuzuma Experiment of Supersonic Air Intake Buzz ISAS Report No. 481 May 1972.
 - [4] В. Г. Гурмлев, А. К. Ильяншин, Е. В. Плотников Течение на Входе и в Горле Воздухозаборника при Грольших Сверхзвуковых Скоростях Лотка и Числах М, Методы Расчетного «Ученые Записки ЦАГИ» ТОМ VI 1975 No. 1.
 - [5] 何中伟 薄附面层的测量技术研究 中国航空学会《航空学报》第3卷 1982 No. 2.
 - [6] 郭允龙 张世英 何中伟 带粘性的超音速轴对称进气道流场计算 《第一届全国计算流体力学会议》论文集, 第三分册, 1982.6.
 - [7] J. Seddon Boundary Layer Interaction Effectation in Intakes with Particular Reference to Those Designed for Dual Subsonic and Supersonic R. & M. No. 3565 1966.
-
- [5] Ho Chung-wei. A Study on the Measurement Techniques for Thin Boundary Layers, Acta Aeronautica et Astronautica Sinica, Vol. 3, 1982, No. 2, Chinese Society of Aeronautics and Astronautics
 - [6] Kuo Yun-lung, Chang Shih-ying and Ho Chung-wei. Computation of Viscous Flow Field in Supersonic Axisymmetric Inlet, Collection of Papers from the First National Conference on Computational Fluid Mechanics, 3rd Booklet, 1982.6.

A PREDICTION METHOD FOR CHARACTERISTICS OF COOLED TRANSONIC
TURBINES WITH LOW ASPECT RATIO AND HIGH LOAD*

Chuang Yü-nan, Chao Yü-ch'i, Shih Ching, Han Chien-yüen

(Nanhua Powerplant Research Institute)

ABSTRACT

At present, advanced aircraft turbines make a feature of low aspect ratio, transonic flow in cascade passage, high aerodynamic load and intensive cooling. In order to predict their characteristics the AMDC formula^(1,2) for cascade loss is corrected on the basis of the so-called KQ system [3] as in formula (3). In accordance with the experimental results of transonic cascades obtained in our country, the AMDC formula for supercritical wave drag is then modified into formulas (4) and (5) for transonic and high subsonic turbines respectively.

For the sake of eliminating the cascade choke conditions which do not exist in fact but often occur in calculation, a suitable relation for the flow angle at cascade exit is proposed.

The prediction method takes into account the various operating conditions, including subcritical, critical and supercritical expansions, limiting supercritical expansion and limiting load, and a computer program has been written.

The characteristics of a transonic and a high subsonic turbine models and the design performances of a cooled turbine with low aspect ratio have been predicted with this method, and compared with test results in good agreement. It is shown that the accuracy is about 99 percent.

* Received in November, 1982.

I. INTRODUCTION

Advanced aircraft turbines are designed with high total temperature of burning gas inlet and high load, and have as their characteristics low aspect ratio, high load transonic, usually unshrouded rotor blades and intensive cooling.

We have introduced the KQ system, recently announced abroad, in our analysis of the AMDC formula for cascade loss. On the basis of the experimental results obtained in our country for transonic plane cascades, we have modified the AMDC formula for supersonic wave drag, and have compiled a complete and practical set of empirical and semi-empirical formulas for loss in low-aspect ratio, high-load transonic cascades.

To solve the problem of the appearance of false choke conditions when the AMD [4] cascade exit flow angle formula is applied, we have, on the basis of careful studies using the empirical, semi-empirical and approximate theoretical formulas used abroad and at home, chosen the Apohob^[5] formula that is more suitable for high-load transonic cascade flow characteristics.

With increasing turbine inlet temperature, the relative amount of cold flow is increased, up to 5-6% for small turbines. The geometric throat of a high-load transonic turbine is usually in a critical or high subsonic state. Therefore, it is necessary to consider the mixing of cold flow in the cascade row by row. A formula for cooling flow mixing has been derived from the theory for one-dimensional compressible axial flow.

Finally, a DJS-6 source program for computing the characteristics has been written to take care of many operating conditions that may arise such as subcritical expansion, mass flow choke, supercritical

expansion, limiting supercritical expansion and limiting load.

II. SYSTEM OF FORMULAS FOR CASCADE LOSS IN TRANSONIC TURBINES WITH LOW ASPECT RATIO AND HIGH LOAD

Turbine cascade loss is usually divided into blade section loss, secondary flow loss, interstitial loss, wake loss and supercritical wave drag loss. Within the past 30 years, many empirical loss formulas have been published. The most famous among these are the Ainley/Mathieson/Dunham/Came (AMDC) system of loss formulas. /5

Table 1 gives typical results obtained from calculations using this system of formulas [6].

TABLE 1. Comparison of AMDC predicted efficiencies with test results for some typical turbines.

涡轮序号	1	2	3	4
2 展弦比 H/B	2.2	0.383	0.446	1.693
3 静叶				
4 动叶	2.387	1.696	1.902	2.937
5 流量系数 W_A/u	0.5342	0.441	0.414	0.639
6 载荷系数 $\Delta H/u^2$	0.3225	1.985	1.454	2.428
7 压比 π_T^*	1.441	2.695	2.616	3.089
8 AMDC 计算效率 η^*	0.893	0.824	0.847	0.831
9 实测效率 η_x^*	0.890	0.84	0.87	0.849
10 效率偏差 $\Delta\eta^*$	-0.307	-0.016	-0.023	-0.018
11 效率相对偏差 $\frac{\Delta\eta^*}{\eta_x^*}$	-0.73%	-1.94%	-2.71%	-2.17%

Key: 1- Turbine No.; 2- Aspect ratio H/B ; 3- Stator blade; 4- Rotor blade; 5- Mass flow coefficient W_A/u ; 6- Load coefficient $\Delta H/u^2$; 7- Pressure ratio π_T^* ; 8- AMDC predicted efficiency η^* ; 9- Measured efficiency η_x^* ; 10- Deviation in efficiency $\Delta\eta^*$; 11- Relative deviation of test efficiency $\frac{\Delta\eta^*}{\eta_x^*}$.

We conclude from the above that:

1. For ordinary turbines, there is good agreement between the AMDC predicted efficiencies and the measure efficiencies. This is the reason why this system of formulas was widely adopted abroad and at home

in the 70's. We have chosen this system as the basis for our system of loss formulas.

2. For high subsonic turbines with low aspect ratio and unshrouded rotor blades, such as turbines No. 2 and No. 3, the AMDC predicted efficiencies are lower than measured values by about 2%. Here, it is necessary to introduce the KQ system.

(1) For cascades with low aspect ratio, the AMDC predicted secondary flow loss is on the high side.

For ordinary turbines, secondary flow loss increases with decreasing aspect ratio. This relation is usually generalized as an inverse relation^[2]. Based on this, when the aspect ratio is at a low value of 0.383, the secondary flow loss is as high as 78.33%, higher than ordinary statistical values^[7]. This shows that the relation should be modified for cascades with low aspect ratio^{[3],[8]}.

TABLE 2. Loss analysis for turbine No. 2.

	1. 展弦比 H/B	2. 二次流损失 y_s	3. 叶型损失 y_p	4. 间隙损失 y_k	5. 总损失 y	y_s/y
6. 静叶	0.3832	0.0723	0.0201	0	0.0924	78.33%
7. 动叶	1.696	0.1235	0.0580	0.0900	0.2438	50.68%

Key: 1- Aspect ratio; 2- Secondary flow loss; 3- Blade section loss; 4- Interstitial loss; 5- Total loss; 6- Stator blade; 7- Rotor blade.

(2) AMDC predicted interstitial loss for unshrouded rotor blades needs to be modified.

Part of the flow does not participate in the deflection but leaks through the radial interstices between the shrouded rotor blades, resulting in a loss. This type of loss is also present in unshrouded rotor blades. Furthermore, for the unshrouded rotor blade, the steep pressure gradient between blade basin and the blade back produces deflected flow at the blade tip, forming a tip interstice vortex which meets the corner vortex there rotating in

the opposite direction. The combined flow moves downstream, not only affecting the low-speed flow in the boundary layer near the end wall, but also disturbing the deflection of the main stream in neighboring regions. (Refer to Figure 1.). The larger the relative radial interstices, the greater their effect on the cascade loss. For turbine No. 2 shown in Table 1, when the radial interstice is 0, the rotor blade total pressure has a recovery coefficient σ dropping to 0.844. The value computed from the AMDC formula for interstitial loss is 0.859. This needs to be corrected.

In addition, the AMDC formulas do not include the effect of the compressibility of the flow on the loss, nor the effect of the extent of choke at the tail edge on wake loss. Hence, it is necessary to introduce the KQ system to correct the AMDC loss formulas.

3. The efficiency predicted with the AMDC formulas for transonic turbines with high load are on the low side. The formula for computing the supercritical wave drag needs to be modified.

To increase the load of the turbine, the Mach number at the cascade exit of high transonic turbines is generally designed at around 1.2. Under the operating condition of supercritical expansion, a series of interacting waves are generated inside the slanted cut. When strong shock waves interfere with the boundary layer, the low-momentum fluid in the boundary layer passes through the shock waves and is slowed down. This generates a reverse pressure gradient which causes the boundary layer to separate, and the loss is increased. We call this the supercritical wave drag loss. Under this condition, the flow spectrum inside the slanted cut is extremely complex.

$$\text{In the AMDC system,} \quad y_p = y_p' f(s) \quad (1)$$

where y_p is blade section loss coefficient, y_p' is the basic blade section loss coefficient when the friction between the blade-surface and the end wall boundary layer is taken into consideration, and $f(s)$ is the increase in loss due to supercritical wave drag.

$$f(s) = 1 + 60(M_1 - 1)^4 \quad (2)$$

AO-A138 531

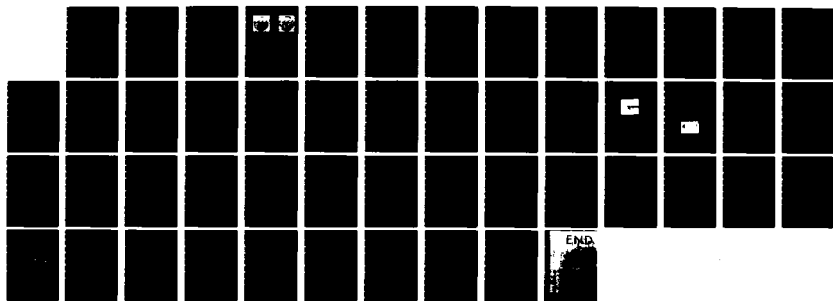
ACTA AERONAUTICA ET ASTRONAUTICA SINICA (SELECTED
ARTICLES)(U) FOREIGN TECHNOLOGY DIV WRIGHT-PATTERSON
AFB OH H Y LI ET AL. 30 JAN 84 FTD-ID(RS)T-1752-83

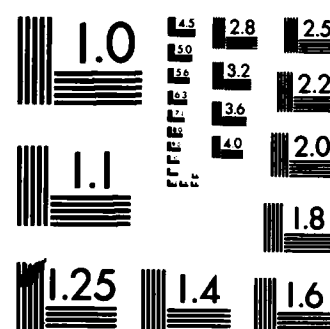
2/2

UNCLASSIFIED

F/G 1/3

NL





MICROCOPY RESOLUTION TEST CHART
NATIONAL BUREAU OF STANDARDS-1963-A

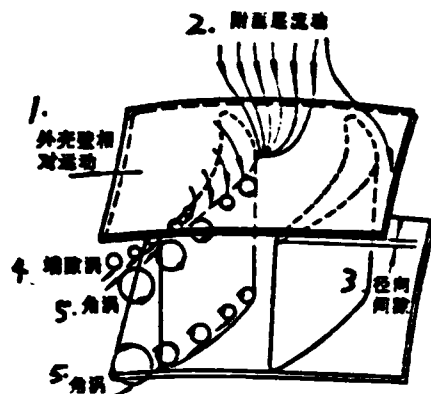


Figure 1. Flow field on free end for unshrouded rotor blade.

Key: 1- Relative motion of the wall; 2- Boundary layer flow; 3- Radial interstice; 4- Tip interstice vortex; 5- Corner vortex.

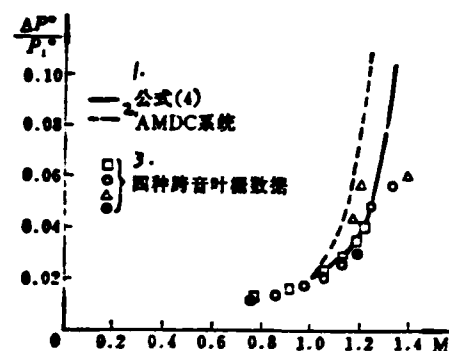


Figure 2. Comparison of transonic cascade test results with AMDC prediction [3].

Key: 1- Formula (4); 2- AMDC syst; 3- Data for four types of transonic cascade.

Figure 2 gives a comparison of transonic cascade test results with the AMDC predicted values [3]. Figure 7 gives a comparison of tests results with the AMDC predicted values for a high subsonic model turbine operating under supercritical expansion condition. This shows that, for high transonic turbines, the AMDC predicted efficiencies are on the low side, and the supercritical wave drag formula (2) needs to be corrected.

In recent years, we have accumulated in our country quite a bit of transonic cascade test results [9], [10]. The following generalizations can be made from this data:

(1) When the transonic cascade is working under the designed operating condition, although the exit Mach number is greater than 1, in general around 1.2, the loss is not very high, as shown in Figure 3. Only when it deviates from the designed operating

condition and continues to undergo supercritical expansion is the loss increased.

(2) The variation of loss with Mach number before the designed operating point may be computed from the KQ system.

This conclusion can be explained by comparing Figures 4 and 5. At the transonic design point $M_1 \approx 1.2$, not only do the shock waves inside the slanted cut tend towards the tail edge, but also their intensity is no higher than that of the shock waves for $M_2 = 1.0$. This is because, when the transonic cascade operates under its designed operating condition, the supersonic flow inside the slanted cut has flow characteristics that are compatible with the geometric /52 properties of the slanted cut. In this case, the blade back portion of the slanted cut is not a source of disturbance for the supersonic flow. Although the shock waves at the tail edge become stronger with increasing Mach number, at the design point, the tail shock FG incident on the slanted cut and its reflected wave GI are weakened by the action of the series of expansion waves CDE and their reflected waves in the slanted cut, (see Figure 6). Under the designed transonic operating condition, the shock waves in the slanted cut are thus not as strong as those under the critical condition. In this case, the loss due to interference of the boundary layer by the shock waves is not as that under the critical condition.

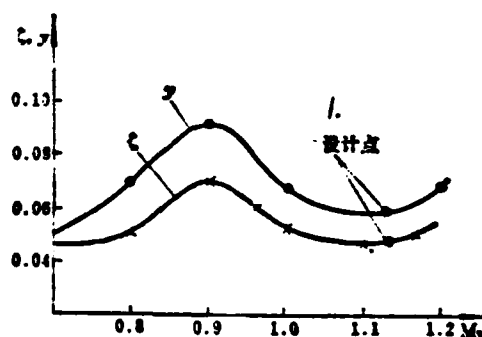


Figure 3. Variation of transonic cascade loss with exit Mach number [9].

Key: 1- Design point

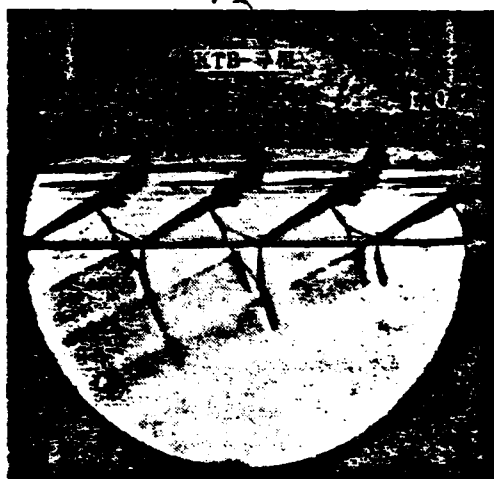


Figure 4. Schlieren photograph of $M_2 = 1.0$ spectrum for a transonic cascade.

Key: 1- KTB-stator blade root.



Figure 5. Schlieren photograph of $M_2 = 1.2$ spectrum for a transonic cascade.

Key: 1- KTB-stator blade root.

Figure 6. Flow pattern in a transonic cascade at $M_2=1.2$.

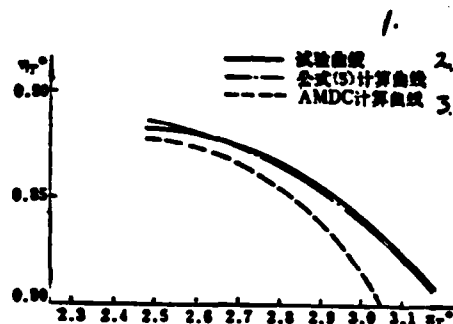
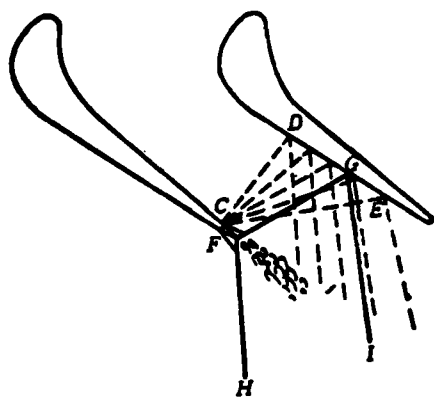


Figure 7. Comparison of prediction with test results for a high subsonic model turbine in supercritical expansion condition.

Key: 1- Experimental curve;
2- Curve obtained from computation using Equation (5);
3- Curve obtained from computation using the AMDC formula.

When the basic blade section loss coefficient is computed from the formula corrected on the basis of the KQ system

$$\gamma' = 0.914 \left(\frac{2}{3} \gamma_{\text{pAMDC}} K_p + \gamma_{\text{shock}} \right) \quad (3)$$

where γ_{pAMDC} is the basic blade section loss coefficient of the AMDC system, K_p is the correction factor to account for the compressibility of the flow, and γ_{shock} is the loss coefficient of the front-edge shock waves, then, on the basis of the AMDC loss formulas, Equation (2) is modified to read

$$f(s) = 1 + 60 (M_2 - M_{\text{design}})^2 \quad (4)$$

In the above, M_{design} is the design Mach number of the transonic cascade.

The validity of this formula has been borne out by tests performed on our high-load transonic model turbine (see Figure 11).

For subsonic and high subsonic turbines, the slanted cut undergoes supercritical expansion, deviating from the design operating condition, and the loss due to supercritical wave drag should be taken into consideration. However, the critical Mach number at the exit of an actual turbine is not 1. We modify Equation (2) on the basis of Equation (3) to read

$$f(s) = 1 + 60 (M_1 - M_{\text{cr}})^2 \quad (5)$$

where M_{cr} is the exit critical Mach number.

The validity of the above equation is borne out by tests on total performance of our high subsonic model turbine (Figure 7). See Table 3 for the exit critical Mach number.

TABLE 3. Exit critical Mach number for a high subsonic model turbine.

1. 叶 型	2. 参 数	3. 总压恢复系数	4. 全压损失系数	5. 尾缘转折角	6. 尾缘楔角	7. 出口构造角	8. 最后临界马赫数
		σ	γ	δ	ω	β_{2c}	M_{cr}
9. 静 叶		0.9855	0.0885	16.38°	11°	20.36°	0.9313
10. 动 叶		0.9123	0.2147	11°	16°	31.3°	0.9618

Key: 1- Cascade; 2- Parameter; 3- Total pressure recovery coefficient; 4- Total pressure loss coefficient; 5- Tail-edge deflection angle; 6- Tail-edge wedge angle; 7- Exit structure angle; 8- Exit critical Mach number; 9- Stator blade; 10- Rotor blade

III. EXIT FLOW ANGLE FORMULA

All the formulas for the exit flow angle have the form $\arcsin\left(K\frac{\theta}{t}\right)$, whether they are approximate theoretical, empirical or semi-empirical formulas. All of them are based on $\beta_{2c} = \arcsin\left(\frac{\theta}{t}\right)$ [4], [5], [11]. K is the deflection factor determined by

- (1) exit Mach number,
- (2) the slanted-cut geometrical characteristics determined by the geometric exit angle, tail-edge deflection angle and tail-edge wedge angle, and
- (3) loss in the cascade channel.

We performed some computations on the turbine characteristics [6] using the Ainley/Mathieson/Dunham formulas [4]

$$\beta_{2c} = \arcsin \frac{A_{2c}}{F_2} \quad M_2 = 1 \quad \beta_{1c} = \arcsin \frac{A_{1c}}{F_1}$$

$$M_2 < 0.5 \quad \beta_{2c} = 1.147 \arcsin \frac{\theta}{t} - 11.1 + 4 \frac{t}{c}$$

$$0.5 < M_2 < 1.0 \quad \beta_2 = \beta_{2c} - 4(\beta_{2c} - \beta_{1c})(1 - 6M_2 + 9M_2^2 - 4M_2^3)$$

The false choke condition shown in Table 4 and Figure 8 was generated in the calculations. This is because the deflection factor used in the AMD formulas was induced from subsonic cascades and is not completely suitable for high subsonic near-critical operating conditions.

Taking into consideration the high transonic cascade flow characteristics, we choose to use the approximate theoretical formula, the Apohob formula [5], that was derived from the basic equations starting out from the concept of passage and taking loss into account:

$$\beta_{1cr} = \arcsin\left(\frac{A_{cr}}{F_1}\right) \quad \beta_2 = \arcsin\left(K \frac{A_{cr}}{F_1}\right)$$

$$K = \cos \alpha \frac{Y\left(\frac{\lambda_2 \cos \beta_2}{\cos \beta_1}\right) \pi \left(\frac{\lambda_2 \cos \beta_2}{\lambda_1 \cos \beta_1}\right)}{Y(\lambda_2) \pi \left(\frac{\lambda_2}{\lambda_1}\right)} \quad (6)$$

TABLE 4. Generation of false choke condition with AMD cascade exit flow angle formula

工 况	1	2	3
3. 临界	0.3641	0.3450	0.9508
4. 假堵塞	0.7758	0.4625	0.7782

Key: 1- Operating condition; 2- Turbine No.; 3- Critical;
4- False choke.

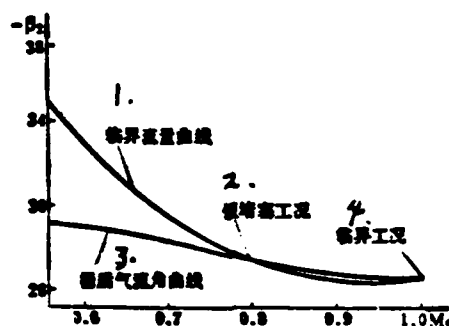


Figure 8. Generation of false choke condition with AMD cascade exit flow angle formula.

Key: 1- Critical mass flow curve; 2- False choke condition;
3- Exit flow angle curve; 4- Critical operating condition

IV. COOLING FLOW AND MAIN FUEL FLOW MIXING FORMULAS

When carrying out calculations for cooling flow mixing in the cascade of a high-load transonic cooled turbine row by row using the one-dimensional compressible axisymmetric flow theory, we first calculate the velocity triangle and aerodynamic parameters for the exit main fuel flow. Then cooling flow mixing is carried out in the axial interstices. Finally, the entrance parameters for the next row are calculated.

The assumptions made in the derivation of the cooling flow mixing formulas are:

(1) Both the cooling flow and the main burning fuel flow are axisymmetric.

/55

(2) The cooling flow and the main fuel flow are mixed evenly in the axial interstices.

(3) Within the axial interstices, the loss due to viscous friction within the flow and between the flow and the end wall may be neglected.

(4) The flows are steady constant flows.

The cooling flow mixing formulas derived from the one-dimensional compressible axisymmetric flow theory are as follows.

$$\frac{\Delta T^*}{T^*} = \frac{\Delta G(c_p T_i^* - c_p T^*)}{(G + \Delta G)c_p T^*} \quad (7)$$

$$\frac{\Delta W_1}{W_1} = \frac{\sin^2 \beta_1}{(1 - M_1^2 \sin^2 \beta_1)} \left\{ \left(1 + \frac{k-1}{2} M_1^2 \right) \frac{\Delta T^*}{T^*} - \frac{1}{\tan^2 \beta_1} \frac{\Delta R_a}{R_a} - \frac{\Delta F_1}{F_1} + \left[1 + \left(k M_1^2 \cos^2 \beta_1 - \frac{1}{\tan^2 \beta_1} \right) (1 - \gamma_a) + k M_1^2 \sin^2 \beta_1 (1 - \gamma_a) \right] \frac{\Delta G}{G} \right\} \quad (8)$$

$$\frac{\Delta t}{t} = -(k-1) M_1^2 \frac{\Delta W_1}{W_1} + \left(1 + \frac{k-1}{2} M_1^2 \right) \frac{\Delta T^*}{T^*} \quad (9)$$

$$\frac{\Delta M_1^2}{M_1^2} = 2 \frac{\Delta W_1}{W_1} - \frac{\Delta t}{t} \quad (10)$$

$$\frac{\Delta W_1}{W_1} = \frac{1}{\sin^2 \beta_1} \frac{\Delta W_2}{W_2} + \frac{1}{\tan^2 \beta_1} \frac{\Delta R_2}{R_2} + \frac{(1 - \gamma_1)}{\tan^2 \beta_1} \frac{\Delta G}{G} \quad (11)$$

$$\Delta \beta_1 = \left(\frac{\Delta W_1}{W_1} - \frac{\Delta W_2}{W_2} \right) \tan \beta_1 \quad (12)$$

$$\frac{\Delta p}{p} = -k M_2^2 \left\{ \frac{\Delta W_2}{W_2} + [\cos^2 \beta_1 (1 - \gamma_1) + \sin^2 \beta_1 (1 - \gamma_2)] \frac{\Delta G}{G} \right\} \quad (13)$$

$$\frac{\Delta p^*}{p^*} = \frac{\Delta p}{p} + \frac{\frac{k M_2^2}{2}}{1 + \frac{k-1}{2} M_2^2} \frac{\Delta M_2^2}{M_2^2} \quad (14)$$

Table 5 gives an example of computation using the above formulas. The predicted values deviate from the measured values by 0.488%, justifying the use of this simplified theory.

TABLE 5. Prediction of cooling flow mixing for the turbine No. 2.

	2.	3.	4.	5.	6.	7.	8.	9.	10.	11.	12.
1. 参数	冷却剂 流量	总温 变化	总压 变化	静压 变化	速度 变化	轴向速度 相对变化	马赫数 相对变化	气流角 变化	静温 变化	冷却剂 掺混	试验效率
	$\Delta G/G$	$\Delta T^0/T^0$	$\Delta P^0/P^0$	$\Delta p/p$	$\Delta W_1/W_1$	$\Delta W_2/W_2$	$\Delta M_2/M_2$	$\Delta \beta_1$	$\Delta T^0/T^0$	13.7%	14.7%
15. 值	1.9%	-1.17%	-0.438%	0.35%	-1.71%	-5.53%	-1.35%	-0.0038	-0.78%	0.8359	0.84

Key: 1- Parameters; 2- Relative mass flow of cooling flow; 3- Relative change in total temperature; 4- Relative change in total pressure; 5- Relative change in static pressure; 6- Relative change in velocity; 7- Relative change in axial velocity; 8- Relative change in Mach number; 9- Change in flow angle; 10- Relative change in static temperature; 11- Calculated efficiency for cooling flow mixing; 12- Measured efficiency for cooling flow mixing; 13- η^* calculated; 14- η^* measured; 15- Numerical values.

V. COMPARISON OF PREDICTED CHARACTERISTICS WITH MEASURED RESULTS

Table 6 and Figures 9-11 give a comparison between the calculated and measured characteristics of a high subsonic model turbine and a high-load transonic model turbine made in this country. The error is 1%.

Table 5 gives a comparison between the calculated and measured efficiency for a cooled high subsonic turbine with low aspect ratio at its design operating point. The error is 0.448%. /56

TABLE 6. Characteristics of design condition for transonic and high subsonic model turbines

1.	2.	3.	4.	5.	6.	7.	8.
参数	膨胀比 π_r	折合功 \bar{L}	滞止效率 η_s	静叶栅出口马赫数 M_{e1}	动叶栅出口相对马赫数 M_{w2}	气流转折角 $180^\circ - (\beta_1 - \beta_2)$	动叶收敛度 $(\beta_1 - \beta_2)$
9. 高亚音速模型涡轮	2.39	20.3	0.887	1.012	0.92	106.53	7.57
10. 高负荷跨音速模型涡轮	3.51	26.3	0.858	1.109	1.047	119.34	7.39

Key: 1- Parameters; 2- Expansion ratio; 3- Equivalent work; 4- Stagnant efficiency; 5- Stator cascade exit Mach number; 6- Rotor cascade exit relative Mach number; 7- Flow deflection angle; 8- Rotor blade convergence; 9- High subsonic model turbine; 10- High-load transonic model turbine.

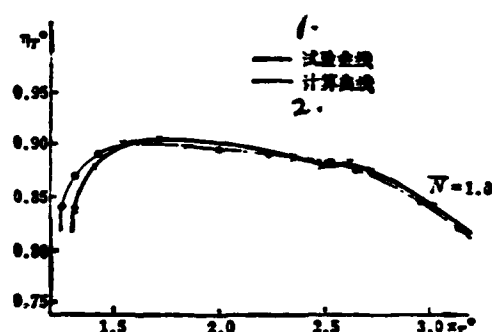


Figure 9. Comparison of predicted efficiencies with test results for a high subsonic model turbine.

Key: 1- Experimental curve;
2- Calculated curve

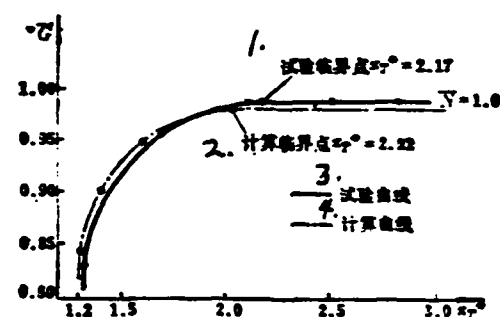


Figure 10. Comparisons of predicted equivalent flow rate with test results for a high subsonic model turbine.

Key: 1- Experimental critical point;
2- Calculated critical point;
3- Experimental curve;
4- Calculated curve

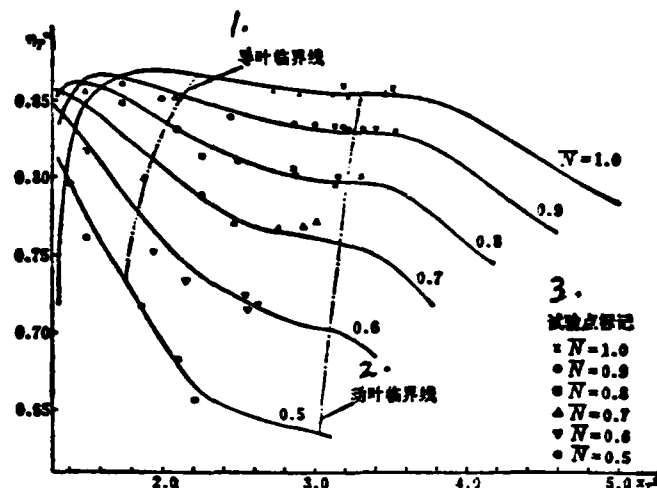


Figure 11. Comparison of prediction efficiency characteristics with test results for a high-load subsonic model turbine.

Key: 1- Critical line for stator blade; 2- Critical line for rotor blade; 3- Notation for test points

VI. CONCLUSION

/57

1. We have shown through tests on the total characteristics that the modifications we made on the AMDC supercritical wave drag formula are justified. The modified formula is applicable to high subsonic or transonic turbines.

2. Better fit is obtained between experimental results and the characteristics calculated from the new set of cascade loss formula and exit flow angle formulas. This shows that this method of computation is applicable to transonic turbines with low aspect ratio and high load as well as to ordinary turbines.

3. It has been shown through an actual computed example that it is appropriate to use the cooling flow mixing formula derived from the simplified one-dimensional compressible axisymmetric flow theory. However, it is to be studied how one can convert the complicated compound cooling flow in the cascade channel into the equivalent exit axisymmetric flow.

Notations

A_{cr}	Area of geometric throat
B	Chord length
β	Flow angle
β_x	Angle between the average momentum vector at the throat and the bow line
c_p	Specific heat
F	Turbine passage area
G	Mass flow
H	Blade height
K	Deflection factor
k	Specific heat ratio
e	Radius of curvature of blade tail edge
M	Mach number
ϕ	Throat width
ΔT^*	Change in total temperature caused by cooling flow mixing
Δp^*	Change in total pressure caused by cooling flow mixing
Δp	Change in static pressure caused by cooling flow mixing
ΔW_2	Change in velocity due to cooling flow mixing
\bar{N}	Ratio of rotational speed to design rotational speed
p	Static pressure
p^*	Total pressure
R_m	Mean radius of axial interstice
T^*	Total temperature
t	Static temperature, cascade spacing
W	Velocity of fuel gas flow
x	Angle between normal to the cross section of the throat and the mean momentum vector
ψ	Velocity coefficient
γ_θ	Ratio of the velocity component of the cooling flow along the perimeter to that of the burning fuel flow
γ_x	Ratio of the velocity component of the cooling flow along the axial direction to that of the burning fuel flow

Notations (Continued)

ΔG Mass flow of the cooling flow
 ΔW_A Axial velocity change due to cooling flow mixing
 ΔM_2 Change in Mach number due to cooling flow mixing
 $\Delta \beta_2$ Change in exit flow angle due to cooling flow mixing
 y Total pressure loss coefficient
 ζ Energy loss coefficient
 \bar{G} Ratio of mass flow to design mass flow

Subscripts:

A Axial
1 Cascade entrance
2 Cascade exit
L Cooling air
ef Effective
1-n From the cascade entrance to throat

REFERENCES

- (1) Ainley, D. G., and Mathieson, G. C. R., "A Method of Performance Estimation for Axial Flow Turbines," British ARC, R&M 2974, 1951.
 - (2) Dunham, J., and Came, P. M., "Improvements to the Ainley/Mathieson Method of Turbine Performance Prediction," ASME Journal of Engineering for Power, July 1970, pp252-256.
 - (3) Kacker, S. C., and Quapan, U., "A Mean Line Prediction Method for Axial Flow Turbine Efficiency," ASME 81-GT-38.
 - (4) Dunham, J., "A Parametric Method of Turbine Blade Profile Design," ASME 74-GT-119.
 - (5) Б. М. Аронов, М. И. Жуковский, В. А. Журавлев, "ПРОФИЛИРОВАНИЕ ЛОПАТОК АВИАЦИОННЫХ ГАЗОВЫХ ТУРБИН," Москва «МАШИНОСТРОЕНИЕ» 1973.
 - (6) 涡轮特性计算方法及DJS-6源程序 清华大学机械研究所赵玉琦。
 - (7) W. Hosny, and W. Tabakoff "Analysis of Loss and secondary Flows in Turbine Cascade," AD-736853.
 - (8) Rogo, C., "Experimental Aspect Ratio and Tip Clearance Investigation on Small Turbines," SAE Paper 680448, Mid Year Meeting Detroit, Mich., May 20-24, 1968.
 - (9) SJ5-3(I) 叶型超音速风试验报告, 北京重型电机厂清河实验室。
 - (10) KT-8动尖 (II) 叶型超音速风试验报告, 北京重型电机厂清河实验室。
-
- [6] A Method of Computation for Turbine Characteristics and DJS-6 Source Program, Chao Yu-ch'i, Nanhua Powerplant Research Institute
 - [9] SJ5-3(II) A Report on Transonic Wind Test on Cascades, Ch'ingho Laboratory, Peiching Heavy Electrical Machine Plant
 - [10] KT-8 Rotor blade tip (III) A Report on Transonic Wind Test on Cascades, Ch'ingho Laboratory, Peiching Heavy Electrical Machine Plant

Effect of Resin Matrix Toughness on Mechanical
Properties of Composite Materials

/60

Northwestern Polytechnical University

Ma Ruiran, Zhou Xizhen, Wang Yan, and Zhang Wu

ABSTRACT

Using the diglycidyl ether of biphenol A--butadiene-acrylonitrile rubber with random carboxyl groups--2-ethyl-4-methylimidazol epoxy resin system as a representative, the effect of the resin matrix toughness on the unidirectional mechanical properties of the glass fiber composite material was investigated. The experimental results showed that with increasing resin matrix toughness, the fracture resistant characteristics of the composite material obtained increased correspondingly. However, the amplitude of increase is smaller than the increment of the toughness of the resin matrix itself. The short beam shear strength of the composite material, in addition to the tensile modulus, and the transverse mechanical properties also improve with increasing resin matrix toughness. The effect on the flexural characteristics and longitudinal mechanical properties, however, was not significant.

INTRODUCTION

In recent years, the use of rubber to toughen epoxy resin has already attracted the attention of many people.^[1~3] However, the rubber used was mostly a butadiene rubber with a carboxyl group at the end. There are few experimental results with other types of rubber reported. Due to the fact that butadiene rubber with a random carboxyl group has already been produced in batches in our country, we chose this rubber as a toughening agent. Its toughening effect on epoxy resin and the effect of the toughened epoxy resin matrix material on the properties of the fiber reinforced composite material were studied. The toughening effect of butadiene rubber with a random carboxyl group on epoxy resin had already been reported by us.^[4,5] The results of the study showed that after being modified by butadiene rubber with a random carboxyl group and biphenol A, the fracture surface energy of the biphenol A epoxy resin was increased by 1~4 times. The

impact strength was increased by 2~10 times. The toughness modulus (the area under the tensile stress-strain curve) was increased by 0.5~11.5 times.

In this paper, the effect of the toughness of the epoxy resin matrix on the mechanical properties of a unidirectional glass fiber composite material was reported. Furthermore, the method of testing the fracture toughness K_Q of a composite material was briefly introduced.

II. TESTING OF FRACTURE TOUGHNESS K_Q

K_Q is the opening type critical stress strength factor of the composite material. We used a double edge notched tensile fracture method in our determination. The dimensions of the test specimen are shown in Figure 1.

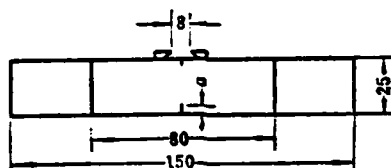


Figure 1. Double edge notched tension specimen

The stress strength factor K is calculated according to the following formula^[6]:

$$K = Y\sigma\sqrt{a} \quad (1)$$

where σ - the stress acting on the two ends of the specimen

a - the effective crack length. The initial crack length adopted in this experiment was $a_0 = 3.5\text{mm}$.

received in September, 1982

Y - the correction coefficient for the geometric shape of the specimen, which is corrected according to the /61

following formula:

$$Y = 1.98 + 0.36 \frac{2a}{w} - 2.12 \left(\frac{2a}{w} \right)^2 + 3.42 \left(\frac{2a}{w} \right)^3 \quad (A)$$

w is the width of the specimen.

The effective crack length is obtained using the compliance calibration curve method. Figure 2 is the dimensionless compliance calibration curve obtained using eight pieces of specimens with different $\frac{2a_0}{w}$ values at two thicknesses of 1 and 2mm. From Figure 2 one can see that the dimensionless compliance curves obtained with specimens fabricated using 1mm and 2mm thick plate materials could coincide each other very well.

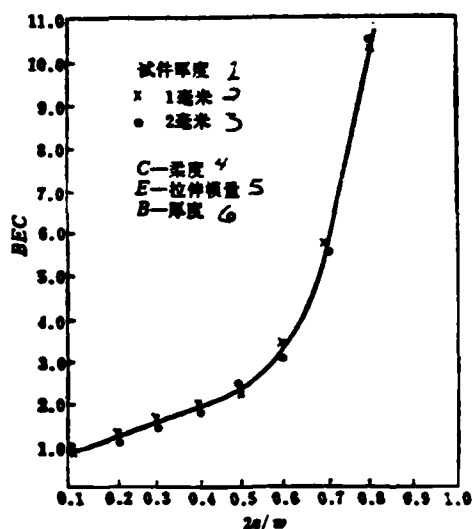


Figure 2. Compliance calibration curve

1. specimen thickness
2. x 1mm
3. o 2mm
4. C-compliance
5. E-tensile modulus
6. B-thickness

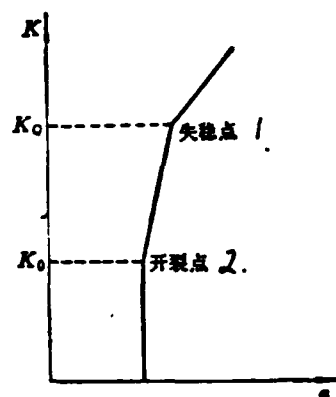


Figure 3. Schematic representation of determining K_Q

1. instability point
2. crack point

According to the curve in Figure 2, the $P-\delta$ curve of each formal specimen, and equation (1), it is possible to obtain the value of K corresponding to the effective crack length in the crack propagation process. From these, the $K-a$ curve is prepared (Figure 3). In this paper, the first turning point on the curve is the crack inception point. The second turning point is the crack instability point. The value K corresponding to the instability point is the fracture toughness K_Q .

III. RESULTS AND DISCUSSION

A unidirectional fiber plate is the basic composition unit of a fiber composite material. For this reason, in order to understand the effect of the toughness of the resin matrix (using impact strength, toughness modulus, and fracture surface energy as the evaluating indicators) on the mechanical properties of a glass fiber composite material, three types of resin-hardener systems were selected as the objects to be studied in this work. The corresponding unidirectional glass fiber composite materials were prepared. The fracture resistant properties and conventional

mechanical characteristics of these three composite materials were analyzed and compared.

The compositions and formulations of these three resin-hardener systems are shown in Table 1. The major thermal-mechanical properties of cast resins are listed in Table 2.

The matrix material A was the unmodified 618 epoxy resin/2-ethyl-4-methylimidazol system. B and C were modified by a random carboxyl butadiene rubber, and a random carboxyl butadiene rubber and diphenol A, respectively. By comparing the data in Table 2, it is possible to see that the fracture surface energy, impact strength, and toughness modulus of the matrix materials A, B, and C were improving gradually. This shows that the ability of these three materials to resist crack propagation and the capability of resisting fracture under a fast and slow load will increase according to the sequence mentioned above. The thermal distortion of these three is more or less the same. Therefore, it can be considered that the matrix materials B and C have a relatively higher toughness. The toughness of C, however, is higher than that of B. The experimental results of the fracture resistance /62 characteristics and conventional mechanical properties of unidirectional glass fiber composite materials corresponding to the three matrix materials are described in the following:

1. 原 材 料	2. 重 量 比	3. 树脂基体		
		A	B	C
618环氧树脂 (双酚A型, 环氧值: 0.48~0.54当量/100克)		100	100	100
无规羧基丁腈橡胶 (工业品)		—	5	5
双酚A (化学试剂级)		—	—	24
2-乙基-4-甲基咪唑 (化学试剂级)		3	3	3

Table 1. Formulation of resin-hardener systems

1. raw material
2. weight ratio
3. resin matrix
4. 618 epoxy resin (biphenol A type, epoxy value: 0.48~0.54 equivalent/100 gram)

5. butadiene rubber with a random carboxyl group (industrial grade)
6. diphenol A (chemical reagent grade)
7. 2-ethyl-4-methylimidazol

/ 测试项目	2. 环氧浇注体		
	A	B	C
3 断裂表面能, $\times 10^5$ 尔格/厘米 ²	0.30	0.67	1.6
4 冲击强度, 公斤·厘米/厘米 ²	3.84	10.2	41.6
5 冲击强度, 公斤·厘米/厘米 ²	3.56	5.29	44.3
6 拉伸强度, 公斤/厘米 ²	455	532	724
7 拉伸弹性模量, $\times 10^4$ 公斤/厘米 ²	3.18	3.14	2.98
8 断裂伸长率, %	1.4	2.0	8.6
9 弯曲强度, 公斤/厘米 ²	942	906	1150
10 弯曲弹性模量, $\times 10^4$ 公斤/厘米 ²	2.94	3.00	2.68
11 热变形温度, $^{\circ}\text{C}$ (弯曲应力: 18.5 公斤/厘米 ²)	96	96	91

Table 2. Properties of cast epoxy resins

1. testing item
2. cast epoxy resin
3. fracture surface energy, $\times 10^5$ erg/cm²
4. impact strength, kg.cm/cm²
5. toughness modulus kg.cm/cm³
6. tensile strength, kg/cm²
7. tensile elastic modulus, $\times 10^4$ kg/cm²
8. fracture elongation rate, %
9. flexural strength, kg/cm²
10. flexural elastic modulus, $\times 10^4$ kg/cm²
11. thermal distortion temperature, $^{\circ}\text{C}$
12. flexural stress: 18.5 kg/cm²

1. Fracture Resistant Characteristics of Unidirectional Glass Fiber Composite Materials

(1) Fracture Surface Energy

The testing results of the fracture surface energy of a crack propagating along the fiber axis are shown in Table 3.

/ 环氧树脂基体	2. 复合材 料	
	3. 含胶量, %	4. 断裂表面能, $\times 10^5$ 尔格/厘米 ²
A	26.43	8.21
B	25.32	13.7
C	27.83	30.4

Table 3. Fracture surface of unidirectional E-glass fiber composites

1. epoxy resin matrix
2. composite material
3. glue content, %
4. fracture surface energy, $\times 10^5$ erg/cm²

A comparison of the data in Table 3 shows that with increasing matrix toughness the fracture surface energies of composite materials B and C increased by 69% and 270% as compared to that of A, respectively. This is because the fibers could not be aligned straight in a composite material. When the tip of a crack passes through the resin matrix, the two surfaces near the crack zone of a crack are still connected by the unbroken fibers or by broken fibers which have not been pulled out. Hence, the fracture surface energy measured by a cleavage test is primarily consumed in the splitting of the matrix, the detachment of the fiber-matrix interface, and the fracture of the fibers. Therefore, increasing the toughness of the matrix and the strength of the fiber-matrix interface will help the fracture surface energy of a composite material to increase.

A comparison of the short beam shear strength of the three composite materials A, B, and C (see Table 6) shows that the bonding force of the fiber-matrix interface is improved after /63

the epoxy resin is toughened by rubber and diphenol A. Therefore, according to the difference in the matrix toughness and interface strength among these three composite materials, it is possible to predict that the improvements in the fracture surface energy are the results of improved matrix toughness and interface strength.

A further comparison of the fracture energy of the composite material and the matrix shows that with increasing matrix toughness, the amplitude of increase in the fracture surface energy of a composite material is smaller than the increment in the matrix itself. This may be attributed to the thin film state of the resin matrix in a composite material since the toughness of a thin film resin is significantly lower than that of a block of resin. [7]

(2) Impact Strength

The impact characteristics of the three composite materials are tabulated in Table 4.

1 环氧树脂基体	2 复 合 材 料				
	3 含量, %	4 横向冲击强度, 公斤·厘米/厘米 ²		5 纵向冲击强度, 公斤·厘米/厘米 ²	
		6 平均值	7 离散系数	8 平均值	9 离散系数
A	25.44	9.21	10.7	603	3.64
B	28.79	12.6	13.4	762	6.10
C	28.08	15.6	13.6	739	4.85

Table 4. Impact strength of unidirectional E-glass fiber composites

1. epoxy resin matrix
2. composite material
3. glue content, %
4. transverse impact strength, kg.cm/cm²
5. longitudinal impact strength, kg.cm/cm²
6. mean value
7. scatter coefficient

8. mean value
9. scatter coefficient

A comparison of the data in Table 4 shows that the composite materials have a relatively higher transverse impact strength (the length direction of the transverse specimen is perpendicular to the axial direction of the fiber) after they are toughened. Composite materials B and C are raised by 39% and 69% as compared with that of A, respectively. The increments of the longitudinal strength of a composite material (the direction of the length of a longitudinal specimen is parallel to the fiber axis) are relatively smaller. B and C improved by 16% and 23%, respectively, as compared to A.

As shown in Figure 4, the fracture mode of a composite material transverse impact specimen is primarily the detachment of the interface and the cracking of the matrix. Therefore, the transverse impact strength is mainly determined by the tensile properties and interface strength of the matrix material. Because the toughness modulus of the matrices B and C is higher than that of A, and the decrease in the tensile elastic modulus is very slight, and the interface strength of composite materials B and C are higher than that of A, therefore, the transverse impact strength of composite materials B and C is higher than that of A.

The fracture process of a composite material longitudinal impact specimen is relatively complex. Because the total energy absorbed when the specimen is broken (not including the energy consumed as the specimen flies away) includes the energy consumed in the "initial fracture" U_i , and the fracture work consumed in the "crack propagation" process U_p , therefore, it is necessary to comparatively analyze the U_i and U_p of the three composite materials in order to understand the contribution of the matrix characteristics to the impact resistant properties of composite materials.

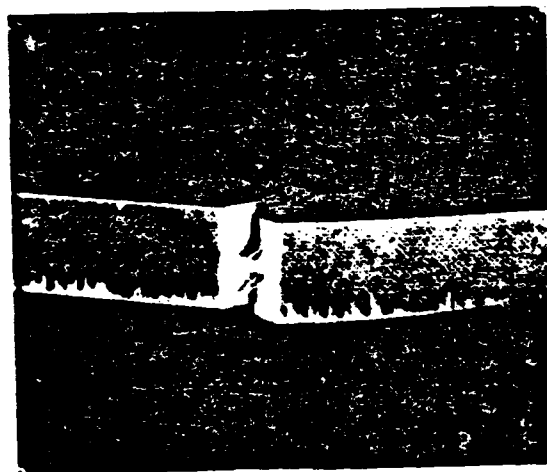


Figure 4. Failed transverse impact specimen

Because the interface strength of the three composite materials increases with increasing matrix toughness, therefore, the capabilities in matrix transfer and load balancing also increase with increasing toughness. Furthermore, the tensile strength and fracture elongation ratio of the toughened matrices B and C are higher than those of matrix A. Consequently, a relatively larger stress is needed for the destruction of the microscopic dimension in the matrix or between the fibers to take place. Therefore, the toughening of the matrix increases the "initial fracture" work U_i of the composite material. /64

An observation of failed longitudinal impact specimens made of composite materials A, B, and C discovered that the mode of fracture of these three materials is mainly due to fiber fracture. Only a small amount of interface detachment existed (see Figure 5). This is because all the epoxy-glass fiber composite materials have the sufficient interface strength. Hence, it is not possible to create a great deal of interface detachment in the

"fracture propagation" process. Fiber fracture is always the major mode of the fracture of the specimen as a whole. Therefore, the U_p of this type of composite material must increase with increasing interface strength.^[8]

According to the above analysis, the presence of a difference among the longitudinal impact strength of composite materials A, B, and C may be primarily due to the difference in the toughness of the matrix materials and in the interface strength. However, because there are more factors influencing the failure of a longitudinal impact specimen, the effect of the matrix toughness on the longitudinal impact strength will be interfered with by other factors.

The above analysis and the results of impact strength testing showed that the improvement of the epoxy resin matrix toughness could raise the resistance against fracture of a composite material in a high speed impact state.



Figure 5. Failed longitudinal impact specimen

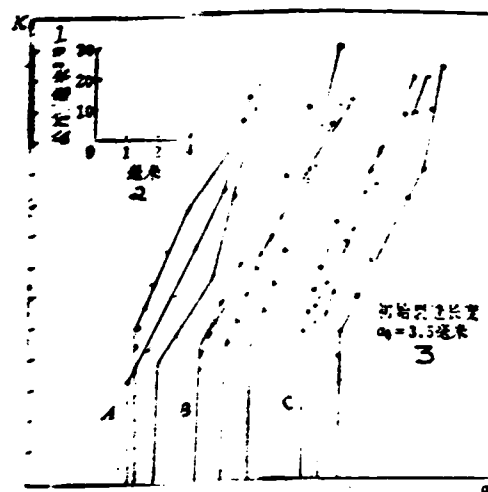


Figure 6. K - a curves of unidirectional E-glass fiber composites

1. $\text{kg} \cdot \text{mm}^{3/2}$
2. mm
3. initial crack length $a_0 = 3.5 \text{ mm}$

(3) Fracture Toughness

Similar to metallic materials, the stress strength factor K can be used as a fracture mechanical parameter for composite materials. However, different from metallic materials, it is very difficult to arbitrarily choose a thickness for a composite material specimen. Furthermore, using a thick specimen, it is very difficult to ensure that a crack will propagate on the same plane. It is not easy to obtain the plane strain fracture toughness corresponding to a metallic material. Therefore, in this paper the stress strength factor at the crack instability point of a specific thickness specimen was used as the fracture toughness K_Q . The instability point was determined by the K - a curve for crack propagation. The K - a curves for the three unidirectional glass fiber composite materials A, B, and C are shown in

Figure 6.

Analysis of Figure 6: the vertical lines in each curve corresponds to the first stage of crack propagation. In this stage, the crack tip displacement increases with increasing load. However, the crack has not yet begun to propagate. The crack length is a fixed value. Immediately afterwards, it enters the second stage, a sub-crack region begins to appear at the tip of the crack. With an increasing stress strength factor, the crack strength increases slightly. The third stage of crack propagation is the gradual stable propagating process of the crack. In this stage, the increment of crack length and the increment of the stress strength factor showed a linear relation. The first turning point on the $K-\alpha$ curve begins to appear. When the stress strength factor increases to a certain value, the slope of the straight line section changes. The second turning point appears. This is the critical point at which the crack changes from stable propagation to unstable propagation. The straight line sections beyond the turning point points upward or downward. It is determined by the stress transferred by the fibers from the crack tip to the hardened band.

/65

The test results of the fracture toughness of the three composite materials are shown in Table 5. In the paper, K_0 , and K_Q are the stress strength factors corresponding to the crack opening point and the instability point, respectively.

From the data shown in Table 5 one can see that the value of K_0 of a composite material increases with increasing matrix toughness. This is because with increasing matrix material toughness the damaged region at the tip of the crack created by the propagation of the sub-critical crack becomes larger. Consequently, more energy can be absorbed and the concentration of stress is reduced. Therefore, a larger stress is required to create a crack. The data in Figure 5 also shows that with increasing matrix toughness,

/ 环氧树脂基体	复合材料	
	$3 K_0$, 公斤/毫米 ^{3/2}	K_Q , 公斤/毫米 ^{3/2}
A	38.0	82.7
B	43.3	94.5
C	48.8	102.5

Table 5. Fracture toughness of unidirectional S-glass fiber composites

1. epoxy resin matrix
2. composite material
3. K_0 , Kg/mm^{3/2}
4. K_Q , Kg/mm^{3/2}

1 测试项目	2. 测试结果	3. 复合材 料	A	B	C
3. 横向拉伸强度, 公斤/厘米 ²	13. 平均值		124	301	384
	14. 离散系数		8.24	10.11	8.86
4. 横向拉伸弹性模量, $\times 10^5$ 公斤/厘米 ²	15. 平均值		1.43	1.10	1.04
	16. 离散系数		—	14.1	14.5
5. 纵向拉伸强度, 公斤/厘米 ²	17. 平均值		7344	7526	8780
	18. 离散系数		4.25	4.88	2.29
6. 纵向拉伸弹性模量, $\times 10^5$ 公斤/厘米 ²	19. 平均值		4.44	4.88	4.89
	20. 离散系数		0.73	0.90	0.79
7. 静弯曲强度, 公斤/厘米 ²	21. 平均值		9300	10500	9860
	22. 离散系数		2.90	4.05	1.80
8. 弯曲弹性模量, $\times 10^5$ 公斤/厘米 ²	23. 平均值		3.36	3.45	3.43
	24. 离散系数		2.87	4.86	1.64
9. 纵向压缩强度, 公斤/厘米 ²	25. 平均值		608	1203	1442
	26. 离散系数		5.94	3.48	6.69
10. 纵向压缩弹性模量, 公斤/厘米 ²	27. 平均值		5634	5881	5323
	28. 离散系数		5.52	4.30	6.78
11. 短梁剪切强度, 公斤/厘米 ²	29. 平均值		636	846	943
	30. 离散系数		6.42	1.37	4.02
12. 含胶量, %			26.43	25.32	27.83

Table 6. Mechanical properties of unidirectional E-glass fiber composites

1. test item
2. test results
3. transverse tensile strength, kg/cm^2
4. transverse tensile elastic modulus, $\times 10^5 \text{kg/cm}^2$
5. longitudinal tensile strength, kg/cm^2
6. longitudinal tensile elastic modulus, $\times 10^5 \text{kg/cm}^2$
7. static flexural strength, kg/cm^2
8. flexural elastic modulus, $\times 10^5 \text{kg/cm}^2$
9. transverse compression strength, kg/cm^2
10. longitudinal compression strength, kg/cm^2
11. short beam shear strength, kg/cm^2

12. glue content, %
13. average
14. scatter coefficient
15. average
16. scatter coefficient
17. average
18. scatter coefficient
19. average
20. scatter coefficient
21. average
22. scatter coefficient
23. average
24. scatter coefficient
25. average
26. scatter coefficient
27. average
28. scatter coefficient
29. average
30. scatter coefficient
31. composite material

the value of K_Q of the composite material also increases correspondingly. Composite materials C and B are 8% and 24% higher than A, respectively. However, comparing with the amplitude of increase in the toughness of the matrix material C, it decreases. This may be due to the fact that the matrix material in a fiber composite material is under the action of forces from three directions. The tough matrix does not yield easily, and consequently it fails by embrittlement. /66

2. Conventional Mechanical Properties of Unidirectional Glass Fiber Composite Materials

The major mechanical properties of composite materials A, B, and C are shown in Table 6. The variation of each property with increased toughness is shown in Figure 7.

Figure 7 shows that after the matrix is toughened the transverse tensile strength, transverse compression strength, and short beam shear strength of composite materials B and C increase. The transverse tensile modulus decreases. The changes of other properties are not obvious.



Figure 7. Effect of matrix toughness on the mechanical properties of unidirectional E-glass fiber composites.

- I. Transverse tensile strength
- II. Transverse compressive strength
- III. Short beam shear strength
- IV. Transverse tensile modulus
- V. Longitudinal tensile strength
- VI. Longitudinal tensile modulus
- VII. Flexural strength
- VIII. Flexural modulus
- IX. Longitudinal compressive strength
- 1. relative value

Because the reinforcing material of the three composite materials is the same type of glass fiber, therefore, the difference in the mechanical properties of a composite material is mainly a reflection of the different mechanical properties of

the three matrix material and the different fiber-matrix interface strength.

The data shown in Table 2 indicated that the major difference in the convention mechanical properties of the matrix materials A, B, and C is shown in terms of tensile strength, fracture elongation rate, and tensile elastic modulus. The first two properties increase with increasing matrix toughness. The latter decreases slightly. From the short beam shear strength of a composite material one knows that the interface strength of composite materials B and C is higher than A. Furthermore, C is higher than B.

Because of the aforementioned difference present in the tensile properties of the matrix materials A, B, and C and interface strength of a composite material, therefore, the conventional mechanical properties of the three composite materials also vary correspondingly. Also because the toughness of the matrix is directly related to the tensile properties and the interface strength of the composite material, therefore, the mechanical properties of the composite material must be affected by the matrix toughness. However, the extent of effect on various mechanical properties is not the same.

IV. CONCLUSIONS

As the matrix toughenss increases, the fracture resistant properties (impact strength, fracture surface energy, fracture toughness) of an epoxy resin-unidirectional glass fiber composite material also increase correspondingly. The short beam shear strength, transverse tensile strength, and transverse compressive strength of a composite material also increase with rising matrix toughness. But, the transverse tensile modulus decreases. The effect of matrix toughness on the flexural properties and longitudinal mechanical properties is not apparent.

REFERENCES

- [1] Drake, R.S. and Siebert, A.R., "Elastomer Modified Epoxy Resins for structural Applications", SAMPE Q, vol. 6, No. 4 (1975), 11.

/67

- [2] Soldatos, A.C. and Burhans, A.S., "Cycloaliphatic Epoxy Resins with Improved Strength and Impact Coupled with High Heat Distortion Temperature," 25th Annual Technical Conference RP/Composites Div., SPI., 3c (1970).
- [3] Rowe, E.H., Siebert, A.R., Drake, R.S., "Toughening Thermosets with Liquid Butadiene/Acrylonitrile Polymers," Modern Plastics, vol. 47, No. 8 (1970), 110.
- [4] Ma Ruiran et al, "Toughening of Composite Materials Using Epoxy Resin (I)," Aeronautical Material Special Issue, Vol.1 No. 2 (1981), 15.
- [5] Ma Ruiran, and Ma Manzhen, "Toughening of Composite Materials Using Epoxy Resin (II)," Northwestern Polytechnical University Technical Information, CL8183 (1981).
- [6] Mandell, J.F. et al., "Engineering Aspects of Fracture Toughness: Fiber Reinforced Laminates," 29th Annual Technical Conference RP/Composites Div., SPI., 17D (1974).
- [7] Scott, J.M., Phillips, D.C., "Carbon Fiber Composites with Rubber Toughened Matrices," J. Materials Sci., vol. 10, No.4 (1975), 551.
- [8] Peter Yeung, Lawrence, J.B., "The Effect of Glass-Resin Interface Strength on the Impact Strength of Fiber Reinforced Plastics," 32nd. Annual Technical Conference RP/Composites Div., SPI., 9B (1977).

MONITORING CURE PROCESS OF COMPOSITES WITH
DYNAMIC DIELECTRIC ANALYSIS TECHNIQUE*

Tu Shicun, Li Xingzhou, Shen Rongying,
Man Shupeng

(Beijing Aeronautical Material Institute)

ABSTRACT

A dynamic analysis monitoring technique is presented for autoclave cure process of composites constructed of T300/8DDT carbon-fiber epoxy resin pre-preg. On the basis of the monitoring technique and with a domestic monitor model JK2107, the appropriate time of pressure application can be chosen and then the "optimum band of pressure application" can be determined successfully by a small number of experiments.

During cure process of thermosetting resin system, a dielectric loss tangent vs time curve can be obtained with the monitor and the "optimum band of pressure application" can be found from the curve. Thus it is possible to choose the proper time of pressure application by the loss tangent, and composite plates with a low void content are made by monitoring the time chosen.

This paper proposes a new way to move the "optimum band of pressure application" to the peak of loss tangent curve or behind it by increasing frequency given by monitor JK2107 and to use the peak of the curve as a reference signal. Therefore, the time of pressure application can be controlled exactly and the quality of composite plates is guaranteed steadily in this way.

* Received October 1982

Monitoring Cure Process of Composites with Dynamic
Dielectric Analysis Technique

/69

Tu Shicun, Li Xingzhou, Shen Rongying, and Man Shupeng
(Beijing Aeronautical Material Institute)

INTRODUCTION

A composite material using a high modulus carbon fiber as the reinforcing body has a much higher specific strength, specific modulus, and fatigue resistance as compared to those of steel, aluminum, and titanium alloys. As far as reducing the structural weight of an airplane is concerned, this is a type of aircraft structural material with a bright future in development. According to the prediction of experts^[1], the composite material used in the high performance fighter structure will rise to around fifty percent by the end of this century from a few percent at the present time. However, the manufacturing of parts by composite materials frequently causes the properties of the materials to fluctuate because there is an absence of a rigorous quality control method. The scatter coefficient of the material strength is increased. Thus, it is necessary to increase the safety coefficient. The superiority of composite materials cannot be fully materialized.

Void is a frequently observed defect in fiber reinforced composite material. In the meantime, it is also one of the major reasons causing the properties of a material to scatter. This defect causes the inside of the composite material to become porous. According to theoretical derivation, as well as large amount of experimental data, the presence of voids was proven. It causes the mechanical properties of the composite material to decline. In the seventies, the technical workers in and out of our country were extremely concerned with the effect of voids on fracture, fatigue, shear strength, and hygroscopicity. A great deal of work was carried out on non-destructive techniques to detect voids. A lot of articles have been published^[2-4]. As far as the dynamic mechanical properties are concerned, a void is a stress concentrating point. Under

the action of a repeated load, it is a fatigue source. As far as static mechanical properties are concerned, voids cause the inside of the material to become porous. They also cause the mechanical properties to decline. According to a report^[3], in an epoxy resin based carbon fiber composite material, when the porosity is under 4%, the laminar shear strength of the composite material will decrease by 4% to 7% as the porosity increases by 1%. With respect to other resins, certain key properties also decrease to the same extent. Some of them even decrease by larger amounts. Therefore, experts have suggested^[5] that: as major structural components of an aircraft, it is required that pores should not be present in composite material fabricated parts, or they should be rigorously controlled to under 1%. As far as secondary structural parts are concerned, the porosity should not exceed 2%. From the above, one can clearly see the significance of obtaining low porosity composite material fabricated parts.

In this paper, a non-destructive detection technique which is capable of obtaining low porosity composite materials - the dynamic dielectric monitoring technique^[6~10], is introduced. This technique can be used to monitor the solidification process of carbon fiber composite materials.

EXPERIMENTAL

1. Brief Description of the Method.

The so-called dynamic dielectric analysis technique is a measuring technique which is capable of automatically and continuously monitoring the variation of dielectric properties of resin systems during solidification under programmed temperature control.

Received in October, 1982

The dielectric analysis technique uses the motion of polar /70 groups present in a thermosetting resin to express the state of the resin system at a particular instance in the solidification process. When an alternating and varying voltage is applied to

the specimen, due to the interaction between the dipole moment and the electric field, the dipole moment will rotate along the direction where the electric field is generated. Because these polar groups are attached to other molecules, therefore, their movement is limited. Hence, the extent to which dipole moment can rotate freely is related to the extent to which these polar groups can move freely in the polymer. During a polymerization reaction, the result is always to increase the constraints applied to the migration of dipole moments. Therefore, the dielectric response characteristics of a resin system with respect to an applied external alternating and varying electric field will vary as the reaction process proceeds. The alignment of a dipole moment and the lagging effect when it rotates can be expressed by the dielectric coefficient and the dielectric loss factor, respectively. Furthermore, both of them are functions of frequency and temperature. The dielectric monitoring technique uses the variation patterns of these two physical quantities to monitor and control the relevant technological parameters. The curves of dielectric characteristics (capacitance C and the tangent of the dielectric loss angle $\tan \delta$) and viscosity (η) in a typical epoxy resin solidification process are as shown in Figure 1. From Figure 1 one can find the portions corresponding to the three stages in the solidification process. In the solidification process, the temperature (T) and the polymerization reaction affect the direction of the dipole moment at various degrees alternatively. During the initial stage of solidification, the resin begins to soften with increasing temperature. It is gradually changed into a molten state. The activity of the polar group increases with decreasing viscosity. The electrical capacitance also continues to increase. Due to the evaporation of low molecular weight compounds, the energy loss continues to rise. A flow peak is shown in the loss curve. As the viscosity of the resin further decreases, it will reach its minimum.

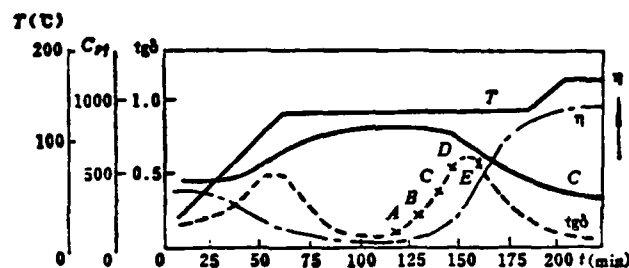


Figure 1. Change in viscosity and dielectric characteristic during curing of typical epoxide resin.

This corresponds to the first stage in the solidification process. Then, the polymerization reaction begins. It causes the viscosity to increase. Moreover, it hinders the alignment of a dipole moment along an electric field. Consequently, it causes $\text{tg}\delta$ to once again increase. The electrical capacitance also decreases. Due to the furthering of solidification, the cross-linking reaction causes the viscosity to increase rapidly. At this moment, $\text{tg}\delta$ decreases from its peak and gradually levels off. This means that the solidification has basically been completed. Therefore, we can monitor and control the solidification process on a real time basis based on the flow variation characteristics of the resin by using the dielectric analysis technique.

2. Experimental Apparatus

In this experiment, a domestic Model JK 2107 automatic dielectric monitoring device, which is capable of automatically reading and continuously recording T , C , and $\text{tg}\delta$ was used. The measuring range of this device included: 0.1~10 KHz in frequency, 0~1000 pF, 0~ ∞ for $\text{tg}\delta$, and 0~350°C in temperature. The block diagram of this dielectric monitoring device is shown in Figure 2.

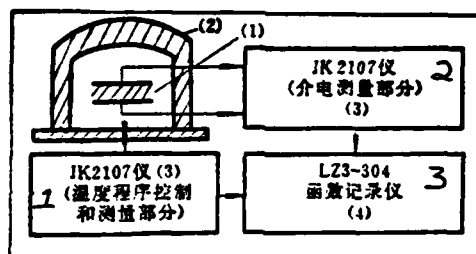


Figure 2. Monitoring curve of dielectric method.

1. The Model JK 2107 Device (3) (the temperature program control and measuring part)
2. The Model JK 2107 Device (the dielectric measuring part)
3. The Model LZ3-304 Function Recording Device

In the figure, the detector (1) is a parallel plate capacitor using a carbon fiber pre-preg material as the medium. The entire detector is placed in a heated pressurized container (2). When the testing frequency is selected, using a certain temperature program, the Model JK 2107 dielectric instrument (3) is used to measure and output the information regarding to $\text{tg}\delta$, C, and T in the solidification process of the resin system. These data points are used as time functions of a three channel scanning recorder. The LZ3-304 function recorder (4) is used to plot the correlation curves between $\text{tg}\delta$, C, and T with time t. /71

3. Selection of Optimized Technological Conditions and the Monitoring and Control Method.

For the usual composite material manufactured parts, the frequently used solidification process obeys a standard set of temperature, time and pressure. We call this standard as the static technological quality control method. Under the situation that various factors are rigorously controlled, it is possible to obtain very good results. In reality, in the middle

of a complicated matter, once there is an interference from internal factor the properties of the fabricated parts will decrease due to improper solidification. They may even have to be scrapped. This is the major disadvantage of the static technological quality control method. Therefore, the development of a non-destructive monitoring and control technique for the resin system to regulate the technological process on a real time basis becomes very important.

The dynamic dielectric analysis technique was used to monitor the solidification process of a resin system. Furthermore, the dielectric characteristic curves related to the resin solidification properties were used as the reference curves in the selection of optimum technological parameters. Then, the curves were used as a basis to regulate the technological process on a real time basis. It is then possible to obtain the optimum properties attainable by the material. The quality of the material is stable and reliable.

In order to obtain the optimum technological parameters, this experiment was carried out using the following method. Under the condition that the temperature program was given by DSC, the pressure application time was the key problem. For this reason, we carried out the solidification test in a heated pressurized container. The specimen used a pre-preg formed by 8DT7 epoxy resin and T300 carbon fiber. The specimens were 14 layer 0° laminated 10 x 15cm samples. The pressure was 7Kg/cm². An instantaneous pressure application method was used. On the tgδ curve in Figure 1, 5 pressure application points at different times, A, B, C, D, and E, were chosen. The solidified composite material was tested in order to determine the short beam shear strength (SBSS), bending resistance strength (σ_f), and porosity (V%). Experimental results are plotted in Figure 3.

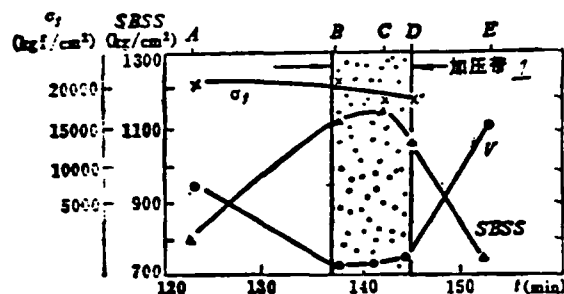


Figure 3. Effect of different pressure application time on properties.

1. pressure application band

According to these experimental results, we can obtain the following conclusions:

(1) The pressure application time cannot be too early, nor too late. If the pressure is applied too early (point A in Figure 4), the resin is lost excessively. In the meantime, due to the fact that low molecular weight compounds are not volatilized sufficiently, the porosity is increased. In a local area, the internal voids are connected together to lead to local delamination. If the pressure is applied too late (point E in Figure 4) beyond the cure point, the resin is already cured. Externally applied pressure can no longer press the resin and the fiber to a solid and compact entity. Thus, local resin accumulations will be formed and ompact entity. Thus, local resin accumulations will be formed inside the material. Furthermore, larger voids will also appear.

(2) When the pressure is applied too early or too late, it will lead to increasing porosity in the composite material. The strength decreases. Therefore, in order to obtain a low porosity composite material, it is necessary to fully remove low molecular weight volatile compounds. Furthermore, pressure must be applied at a suitable time (point C in Figure 3) before

it starts to cure so that the optimum properties of the materials can be attained.

(3) From Figure 3 one can see that a pressure application belt can be found in a region around point C in which the strength variation is not too much. Its width can be determined by the allowed fluctuation range of the material.

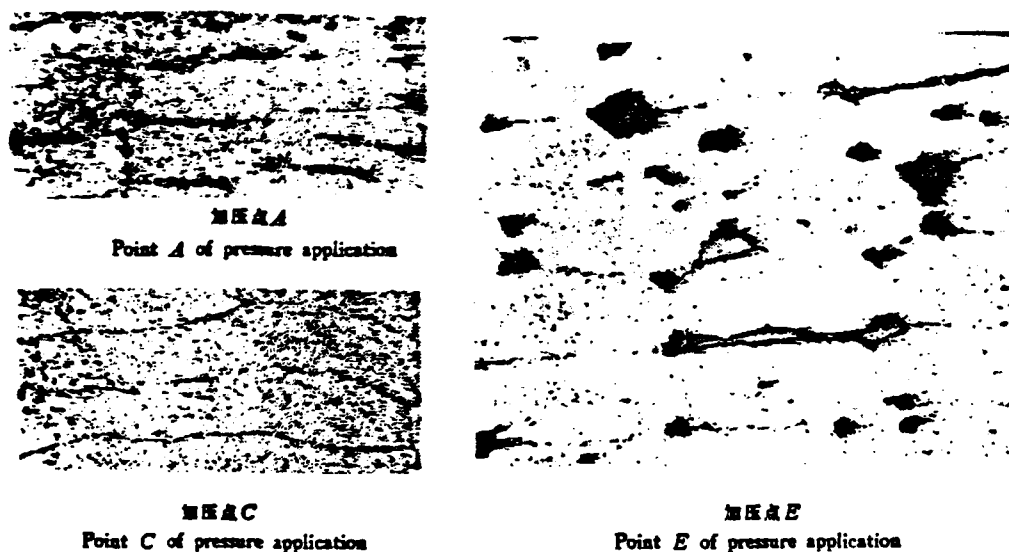


Figure 4. Photo micrograph of different time of pressure application.

/72

(4) The tangent of the dielectric loss angle $\text{tg}\delta$ in the region corresponding to the pressure application zone is our information to monitor and control the application of pressure. The usual value of $\text{tg}\delta$ is affected by many factors. To simply use $\text{tg}\delta$ to monitor and control the pressure application time cannot reach good results. However, the peak value of $\text{tg}\delta$ represents a special turning point.

The authors presented a method to increase the testing frequency so that this turning point is displaced to within or in

front of the monitoring and control region (See Figure 5). It is used as the monitoring and control signal. Thus, the accuracy of monitoring and control can be increased.

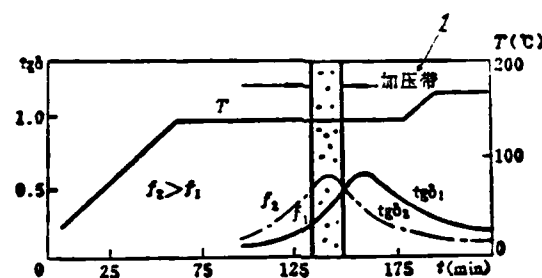


Figure 5. Monitoring curve of dielectric method.

1. pressure application band

CONCLUSIONS

We used the Model JK 2107 instrument to monitor and control the pressure application of a carbon fiber composite material during the solidification process with a press in a heated and pressurized container. The test has already proven that: this monitoring and control technique, when used in the quality control in the solidification process, can obtain a composite material plates with less than 1% porosity.

REFERENCES

- [1] Song Tian Zi and Hu Daibanglong, "Carbon Fiber Composite Materials Used in Aircrafts," Journal of the Society of Aeronautics and Astronautics in Japan, Vol. 30. No. 338, 1982, p. 18.
- [2] E.F. Olster, "Effect of Voids on Graphite Fiber Reinforced Composites," AD-746 560.

/73

- [3] N.C.W. Judd and W.W. Wright, "Voids and Their Effects On The Mechanical Properties of Composites--An Appraisal," SAMPE Journal Vol. 14, No. 1, January/February, 1978, p.10.
- [4] D.E.W. Stone and B. Clarke, "Ultrasonic attenuation as a Measure of Voids Content in Carbon fibre Reinforced Plastics," NDT Research and Practice, Vol. 8, No. 3, June, 1975, p. 137.
- [5] D.J. Hagemmaier and R.H. Fassbender, "Nondestructive of Advanced Composites," Mat. Eval. Vol. 37, No. 7, June 1979, p. 43.
- [6] B.G. Martin, "Monitoring The Composite Cure Cycle by Dielectric Analysis," Mat. Eval. Vol. 34, No. 49, 1976.
- [7] S.A. Yalof, "Dielectric Monitoring of Cure," Rubber Age, Vol. 6, No. 29, June, 1976, p. 29.
- [8] L.D. Dragatakis and Z.N. Sanjana, "Dielectric Analysis in the Control of Vacuum-Pressure Impregnation and Cure of Coil-Insulation Tap," 35th ANTECH SPE., April, 1977.
- [9] J. Yokota, "In-Process Controlled Curing of Resin Matrix Composites," SAMPE Journal, Vol 14, No. 4, July/August, 1978, p. 11.
- [10] G. Wm. Lawless, "Dielectrometry as A Cure Monitoring Technique For Composites/Resin Processing," ICCM₃ Volume 2, 1980.

✕ The Society, together with the Astronautics Society of China and China Aerodynamics Research Society, held the "Technical Discussion Meeting on Viscous Flow and Surface Layer" on October 31st through November 6th in 1982 in the city of Fuzhou. Sixty four representatives attended the meeting. The meeting received 35 technical papers, and 22 were read in the meeting.

✕ The Society held nine technical exchange meetings between November and December 1982. They included:

1. On November 2-8, the "Technical Meeting on Environmental Control and Protection in Aircraft Cockpits" was held in Kunming. 92 representatives attended the meeting. 65 technical papers were received. 50 of them were read in the meeting.

2. On November 5-11, the "Forging Technique Exchange Meeting" was held in Jiujiang. 59 representatives attended the meeting. 42 technical papers were received. 28 of them were read in the meeting.

3. On November 14-20, the "Technical Exchange Meeting on the Auxiliary Engine and Precision Machining Special Fields" was held in Wuxi, Jiangsu. 122 delegates attended the meeting. It received 85 technical papers and 57 of them were read in the meeting.

4. On November 15-21, the "Technical Discussion Meeting on the Strength of Aeronautical Gears" was held in Zhuzhou, Hunan. 73 delegates attended the meeting. 45 technical papers were received and 34 of them were read in the meeting.

5. On November 18-22, the "Rocket Engine Special Field Technical Exchange Meeting" was held in Changsha. 47 delegates attended the meeting. 40 technical papers were received, and 25 were read.

6. On November 22-28, the "Aircraft Incident Inspection and Analysis Technical Discussion Meeting" was held in Beijing. 73 delegates attended the meeting. 35 technical papers were received, and 25 of them were read in the meeting.

7. On December 4-10, the "Aeronautical Auxiliary Engine Computer Aided Design and Manufacture Meeting" was held in Fuzhou. 79 representatives attended the meeting. 41 technical

papers were received, and 36 of them were read in the meeting.

8. On December 6-10, the "Technical Exchange Meeting on Data Collection, Processing, and Control Systems Centered Around Computers" was held in Chengdu. 79 delegates attended the meeting. 50 technical papers were received, and 46 of them were read in the meeting.

9. On December 16-23, the "High Temperature Fatigue and High Temperature Strain Testing Technique Meeting" was held in Chengdu. 102 delegates attended the meeting. 60 technical papers were received, and 48 of them were read in the meeting

The Society of Aeronautics in China Held an Academic Activity Symposium in Beijing.

/76

The Society of Aeronautics in China held an academic activity symposium on January 18, 1983 at the People's Conference Hall in Beijing. There were ninety one people, including the secretary general and vice secretary general of the Society of Aeronautics in China in Beijing together with the chairmen of various special field committees, academic secretaries, and responsible comrades of related organizations. The secretary general of the Society of Aeronautics in China, comrade Wang Junkui, presided the meeting. Comrade Zhao Zhengyan, the vice secretary general of the Society of Aeronautics in China, gave a working report on the "summary of academic activities in 1982" and the "key points of academic activities in 1983." Comrade Liu Tianfu, who is the vice secretary of the Party Committee of the Chinese Science Association, arrived at the meeting and gave an important speech.

Under the leadership of the Party organizations of the Chinese Science Association, Aeronautical Industry Ministry, and the Society, and with the support of the vast scientific and technical personnel, the related units nationwide, and the aeronautic societies in various provinces and cities, through the joint effort of various special committees and special academic groups, the academic activities of the Society in 1982 were successfully completed according to the 1982 academic activity plan. Twenty eight academic meetings were

held in 1982. A short term class was held. As compared to last year, the number of activities increased by 26%. The total number of technical papers received was 1699, and 1259 of them were read in various meetings. 2499 people participated in the academic activities. Through these academic activities, the results of recent academic research and working experience were summarized and exchanged. The trends of development of related special fields in and out of our country were analyzed and explored. Technical advisory suggestions were provided to the relevant department. The various academic organizations were established and further strengthened. The future academic activity plan was discussed. Through these academic activities, the planning of domestic academic activities and the organizational management work were further strengthened. The rules and regulations needed were established and perfected. The "temporary regulation regarding organizing domestic academic meetings" and the "brief rules governing special committees." The work of various special committees and the development of academic activities were promoted.

The 1983 academic activity plan has already been formulated. A total of 35 academic meetings, 5 training classes, and 2 academic working meetings will be arranged. The total number is 42. In the activities in this year, the emphasis will be placed on the selection and recommendation of outstanding papers. Conditions will be created so that training classes for scientific and technical personnel can be operated well. The special features of academic activities will be combined in order to open up various technical consulting activities. The extension and exchange of academic activity results must be seriously carried out.

Vice Secretaries of the Society, comrades Dong Xiao, Hang Mingyang, and Zhang Peijian, as well as Special Committee Chairmen such as comrades Zhuang Fengang, and Lin Shier, spoke at the meeting. They provided valuable suggestions regarding the direction of future development of the academic activities of the Society and the development of the aeronautic industry in

our country. During the meeting, the experts and professors in the elder generation of the aeronautic community in our country and the young and middle age technical workers gathered together in the same room in harmony. In the afternoon, the various special committee academic secretaries in Beijing continued to meet specifically with respect to some actual problems in academic work. Everyone was enthusiastically in agreement with the academic working conference held by the Society in August this year. The academic work experience was summarized and exchanged. Problems such as how to further improve the quality of academic meeting was explored.

Obituary

In Deep Memory of Comrade Wang Terong,
Chief Editor of ((Journal of Aeronautics))

/77

Chief Editor of ((Journal of Aeronautics)), Comrade Wang Terong died on December 2, 1982 due to sickness. He was seventy four. His departure was an important loss to the research and education in aeronautics in our country. It is also an important loss to this publication.

Comrade Wang Terong graduated from Shanghai Jiaotong University in 1932. He went to England to study in 1935. He returned to our country in 1938. Until 1951, he was professor and chairman at Southwest Consolidated University and Qing Hua University. In 1952, he participated in the planning work of Beijing Institute of Aeronautics and Astronautics. For over thirty years, he had made great contributions to the construction and growth of Beijing Institute of Aeronautics and Astronautics. In 1964, during the founding process of the Society of Aeronautics in China, he was one of the active supporters. Since 1965, from the beginning of ((Journal of Aeronautics)), he was the chief editor. He worked very hard in the manuscript reviewing, editing, and publishing of each volume of the ((Journal)). Even when he was critically ill, he still remembered the work at the ((Journal)).

For over half a century, comrade Wang Terong dedicated all his energy to the aeronautic industry in his own country.

During the period ruled by the reactionary Nationalists, he remained straight while facing the dark ruling power. He did not try to get close to the center of power. He was dissatisfied with the corrupt authority. Furthermore, he was actively helping progressive students with sympathy. In 1949, Comrade Wang Terong was touring the United States. As soon as he heard the good news that the new China was founded, he immediately started to return to our country to devote to the construction of our homeland. He was actively close to the party organization and insisted on the accurate position. He was persistent and maintained the realistic attitude. He supported the leadership of the Party and the socialistic route. During the three year difficulty period, he not only did not withdraw, on the contrary, obtained more progress politically with enthusiasm. In December 1961, he joined the Chinese Communist Party with honor. During the ten year period of chaos, no matter whether it was political oppression or torture in life, the Comrade Wang Terong's decision to struggle for the Party and the people was not shaken. After Premier Chou proposed the magnificent objective of the Four Modernizations, he gave lectures to research organizations actively. He provided a lot of rationalized opinions to overcome technical obstacles. He solved some major difficulties in research and production. Until he was critically ill, he still made his best effort to illuminate the scientific exploration route with his life.

Throughout his life, Comrade Wang Terong devoted his honorable life to the aeronautical industry in our country. It was a life seeking for progress. It was a life of hard struggle and hard work. He had raised many outstanding students. He was an elder leader and an elder teacher with reputation in the aeronautical community. However, he never sought for honor and position for himself. He was a famous professor and an expert. He was a council member of the Chinese Mechanics Society, a council member of the Society of Aeronautics in China, a specially invited committee member of the Scientific Technical Committee of the Aeronautical Industry Ministry, and a member of

the Political Association of Beijing. However, he never claimed credit and became arrogant. He was humble and easy to approach. He had written and reviewed a great deal of papers. However, he never let each detail go and repeatedly pondered on the key words. Comrade Wang Terong was indeed an outstanding teacher of the people. He was indeed a good member of the Chinese Communist Party.

Comrade Wang Terong left us. This made us sincerely sorrowful. However, we must transform sorrow into strength. We must learn from him the excellent quality of his loyalty to the Party and to education. We must learn the rigorous and serious attitude in studying from him. Under the guidance of the spirit of the 12th Congress of the Party, we must succeed the career started by Comrade Wang Terong. We must continue to work hard to run ((Journal of Aeronautics)) well in order to struggle hard for the beautiful tomorrow of the aeronautical and astronautical career of our country.

Editing Committee of ((Journal of Aeronautics))

December /1982

REFERENCES

- (1) 後田 豊・戸愛邦明, "航空機用炭繊維複合材料について", 日本航空宇宙学会誌, Vol. 30, No. 338, 1982, P18.
- (2) E. F. Olster, "Effect of Voids on Graphite Fiber Reinforced Composites" AD-746 560.
- (3) N. C. W. Judd and W. W. Wright, "Voids and Their Effects On The Mechanical Properties of Composites—An Appraisal", SAMPE Journal Vol. 14, No. 1, January/February, 1978, P10.
- (4) D. E. W. Stone and B. Clarke, "Ultrasonic attenuation as a Measure of Voids Content in Carbon fibre Reinforced Plastics", NDT Research and Practice, Vol. 8, No. 3, June, 1975, P137.
- (5) D. J. Hagmaier and R. H. Fassbender, "Nondestructive of Advanced Composites", Mat. Eval. Vol. 37, No. 7, June 1979, P43.
- (6) B. G. Martin, "Monitoring The Composite Cure Cycle by Dielectric Analysis", Mat. Eval. Vol. 34, No. 49, 1976.
- (7) S. A. Yalof, "Dielectric Monitoring of Cure", Rubber Age, Vol. 6, No. 29, June, 1976, P29.
- (8) L. D. Dragatakis and Z. N. Sanjana, "Dielectric Analysis in the Control of Vacuum-Pressure Impregnation and Cure of Coil-Insulation Tap", 35th ANTECH SPE, April, 1977.
- (9) J. Yokota, "In-Process Controlled Curing of Resin Matrix Composites", SAMPE Journal, Vol. 14, No. 4, July /August, 1978, P11.
- (10) G. Wm. Lawless, "Dielectrometry as A Cure Monitoring Technique For Composites/Resin Processing", ICCM3 volume 2, 1980.

END

FILMED

384

DTIC